AD-774 844

EVALUATION OF THE CONAP (CONTROLLED ATMOSPHERIC PROTECTED SYSTEM) CONCEPT FOR ADVANCED ABM NOSE TIPS

Archie Ossin, et al

Martin Marietta Aerospace

Prepared for:

Army Materials and Mechanics Research Center

January 1974

NTIS	
DDC	
JUSTIFICATION	
BY	
DISTRIBUTION/AVAILABILITY	
Dist.	
A	

The view and conclusions contained in this document are those of the authors and should not be interpreted as necessarily representing the official policies, either expressed or implied, of the Defense Advanced Research Projects Agency of the U. S. Government.

Mention of any trade names or manufacturers in this report shall not be construed as advertising nor as an official indorsement or approval of such products or companies by the United States Government.

UNCLASSIFIED

SECURITY CLASSIFICATION OF THIS PAGE (When Data Entered)

AD 774844

REPORT DOCUMENTATION PAGE		READ INSTRUCTIONS BEFORE COMPLETING FORM
1. REPORT NUMBER AMMRC CTR 74-1	2. GOVT ACCESSION NO. –	3. RECIPIENT'S CATALOG NUMBER
4. TITLE (and Subtitle) Evaluation of the CONAP Concept for Advanced ABM Nose Tips		5. TYPE OF REPORT & PERIOD COVERED Final Report
		6. PERFORMING ORG. REPORT NUMBER OR 12,840
7. AUTHOR(s) Archie Ossin Don M. Cawthon		8. CONTRACT OR GRANT NUMBER(s) DAAG46-73-C-0053
9. PERFORMING ORGANIZATION NAME AND ADDRESS Martin Marietta Aerospace Orlando Division Orlando, Florida 32805		10. PROGRAM ELEMENT, PROJECT, TASK AREA & WORK UNIT NUMBERS D/A Project:1W162113A661 AMCMS Code: 612113.11.07000 Agency Accession: –
11. CONTROLLING OFFICE NAME AND ADDRESS Army Materials and Mechanics Research Center Watertown, Massachusetts 02172		12. REPORT DATE January 1974
		13. NUMBER OF PAGES 158
14. MONITORING AGENCY NAME & ADDRESS(if different from Controlling Office)		15. SECURITY CLASS. (of this report) Unclassified
		15a. DECLASSIFICATION/DOWNGRADING SCHEDULE –

16. DISTRIBUTION STATEMENT (of this Report)

Approved for public release; distribution unlimited.

17. DISTRIBUTION STATEMENT (of the abstract entered in Block 20, if different from Report)

18. SUPPLEMENTARY NOTES

19. KEY WORDS (Continue on reverse side if necessary and identify by block number)

Anti-missile missiles	Transporation
Nose cones	Gas permeability
Cooling Systems	Porous metals

20. ABSTRACT (Continue on reverse side if necessary and identify by block number)

This document reports the results of a twelve month research study of a transporation-cooling system concept having application to the nose tip and control surface leading edges of an advanced ABM. This concept uses a reactive gas coolant and a hot wall matrix. Testing has been conducted to determine the permeability and inertial resistance coefficients of candidate refractory porous and discrete hole matricies. Testing was also

DD FORM 1 JAN 73 1473 EDITION OF 1 NOV 65 IS OBSOLETE

UNCLASSIFIED

SECURITY CLASSIFICATION OF THIS PAGE (When Data Entered)

20. Abstract (Continued)

conducted to determine the amount of heat transfered from the hot matrix to the coolant gas. The results show that system weight savings would be realized from use of the CONAP concept when compared to a water system. The data taken have been correlated with curve fits and used to conduct preliminary concept design analyses.

AD

AMMRC CTR 74-1

EVALUATION OF THE CONAP CONCEPT FOR ADVANCED ABM NOSE TIPS

January 1974

Archie Ossin
Don M. Cawthon

Martin Marietta Aerospace
Orlando Division
P. O. Box 5837
Orlando, Florida 32805

Final Report - Contract DAAG46-73-C-0053

D/A Project 1W162113A661
AMCMS Code 612113.11.07000

Prepared for

ARMY MATERIALS AND MECHANICS RESEARCH CENTER
Watertown, Massachusetts 02172

i b

FOREWORD

This report was prepared by Martin Marietta Aerospace, Orlando Division, for the Army Materials and Mechanics Research Center, Watertown, Massachusetts, under contract DAAG46-73-C-0053 (Reference 1). This work is part of the AMMRC program on Development of Hardened ABM Materials, Mr. John F. Digman, Program Manager. The AMMRC Technical Supervisor was Mr. Lewis R. Aronin.

This report covers the work conducted from 24 October 1972 through 24 October 1973.

The work reported was performed by personnel from the Aeromechanical Division. Mr. Archie Ossin was the Task Leader and Mr. William A. Bauman was Program Manager

ABSTRACT

This document reports the results of a twelve month research study of a transpiration cooling system concept having application to the nose tip and control surface leading edges of an advanced ABM. This concept uses a reactive gas coolant and a hot wall matrix. Testing has been conducted to determine the permeability and inertial resistance coefficients of candidate refractory porous and discrete hole matricies. Testing was also conducted to determine the amount of heat transfered from the hot matrix to the coolant gas. The results show that system weight savings would be realized from use of the CONAP concept when compared to a water system. The data taken have been correlated with curve fits and used to conduct preliminary concept design analyses.

CONTENTS

ILLUSTRATIONS

TABLES

SUMMARY

This investigation consists of the initial task in the development of efficient transpiration cooling technology for Advanced Interceptor Requirements in order to provide a lighter weight, more erosion resistant system than conventional water systems. The Controlled Atmospheric Protected System (CONAP) is a concept which utilizes a reactive gas, ammonia, as the coolant and a refractory metal as the matrix. The injection of ammonia into the boundary layer medium cools the matrix and reacts with the boundary layer oxygen. In principle this control of oxygen allows operation at high surface temperature, which greatly lowers the coolant flow requirements while limiting the oxidation of the hot surface materials to acceptable values.

The purpose of this initial study was to evaluate available porous refractory materials and their applicability as nose tip or air vane leading edge materials in a flight environment. Characteristics of the materials and the operating efficiency of the concept were evaluated by laboratory testing.

These laboratory tests consisted of obtaining flow characteristic data (permeability and inertial resistance coefficient) for a variety of porous tungsten and discrete hole tungsten matricies; also, the heat transferred from a hot tungsten matrix to the ammonia gas passing through was measured. The materials and concepts that were evaluated and the tests performed are shown in Table I.

The tests were performed on each of the materials and concepts shown. Heat transfer coefficient data and flow characteristics data were obtained for a wide range of porous tungsten materials ranging from 50 percent (by volume) tungsten to 80 percent tungsten. Complete correlations of the data have been obtained. The results of these tests and correlations are briefly summarized in Table II and described below. Local mass flow in porous tungsten materials can be greatly increased to meet local flow requirements by augmentation with blind holes without significantly affecting the internal heat transfer coefficient. This concept has potential usage for the sonic point on a nose tip or the stagnation line on an air vane leading edge. Schlieren photographs show that the blind holes do not starve other areas of coolant. Surface vapor deposition modification to porous tungsten matricies can decrease the mass flow in a local area without affecting the heat transfer coefficient. This concept can be effectively used on the sidewall of a nose tip or air vane leading edge to minimize the variation between actual and ideal coolant mass flow rates.

TABLE I

Test Summary

Flow Direction	Materials and Concepts Evaluated	
	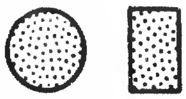	Porous tungsten
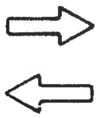	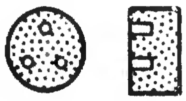	Porous tungsten modified with blind holes to increase flow
	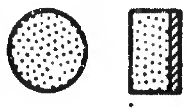	Porous tungsten modified with vapor deposition to decrease flow
	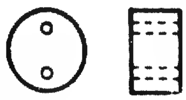	Discrete hole tungsten – copper
	Tests Conducted	
	• Internal heat transfer coefficient • Flow characteristics tests (permeability and inertial resistance coefficient)	

TABLE II

Summary of Results

Task	Result
Select available materials for evaluation	All available porous refractory materials were evaluated (Wah Chang, Sylvania, Mallory and Astro Met materials were used)
Obtain laboratory test data to determine a. Inertial resistance coefficient b. Permeability c. Heat transfer coefficient	Data was obtained on all candidate materials plus porous materials augmented with blind holes and porous materials with vapor deposited tungsten. Results indicated CONAP concept to be more efficient than a water system
Select the optimum material	Using the laboratory test data, the 80 percent Wah Chang and 80 percent Sylvania materials were selected as optimum
Establish a preliminary conceptual design	Using the laboratory test data the 80 percent Wah Chang material modified with blind holes at the sonic point and a 20 micron vapor deposition on the sidewall was selected.

The heat transfer coefficient and flow characteristic data, once correlated, were used to optimize the materials and concepts for use in a flight environment. The efficiency of the CONAP concept can be compared to an equivalent water system since the internal heat transfer coefficient is now known for a wide range of materials. This comparison, made for a typical advanced interceptor trajectory (Figure 1), shows that the CONAP system using a porous tungsten matrix and ammonia coolant is 50 percent lighter than a water system. Figure 1 also shows that the CONAP system, augmented with blind holes, is 40 percent lighter than a water system. To optimize the CONAP system efficiency in a flight environment, the heat transfer coefficient and flow characteristic data were used to conceptually design several nose tips that could be used in an Advanced Interceptor application. The mass flow variation between ideal coolant requirements and actual mass flow (Figure 2) was used as a major criterion for selection of the best materials and concepts. The results of the conceptual design activity showed that use of the Sylvania and Wah Chang porous tungsten materials (80 percent by volume) resulted in the lowest coolant flow variation. Figure 3 shows a flow characteristic correlation, the reciprocal of the permeability versus the inertial resistance coefficient, of all of the materials tested. The figure identifies those materials which fall into the region of low efficiency due to the excessive sidewall mass flow that could not be effectively reduced even with a maximum of 20 microns of tungsten vapor deposit. The region of high material efficiency also has limitations due to very high chamber pressure requirements (P_c > 6000 psi) and low wall thicknesses (t < 0.1 inches). The Sylvania and the Wah Chang (80 percent by volume) porous tungsten fall within the optimum range shown between the two vertical lines in Figure 3. The specific nose tip design that minimizes the mass flow variation is shown in Figure 4. This design consists of a Wah Chang 80 percent porous tungsten material augmented with blind holes at the sonic point to increase the coolant flow, locally, and modified with a 20 micron vapor deposit on the sidewall to decrease the flow rate, locally.

Scanning electron micrographs (50X to 10,000X) of the materials and concepts tested, as well as Schlieren photographs of a surrogate flow field exiting the tungsten and modified tungsten matricies, basically reinforce and corroborate the data correlations and conclusions of this report.

Based on the results of this evaluation, a thermal test program consisting of plasma arc tests over a range of heating rates and stagnation pressures is recommended for future evaluation.

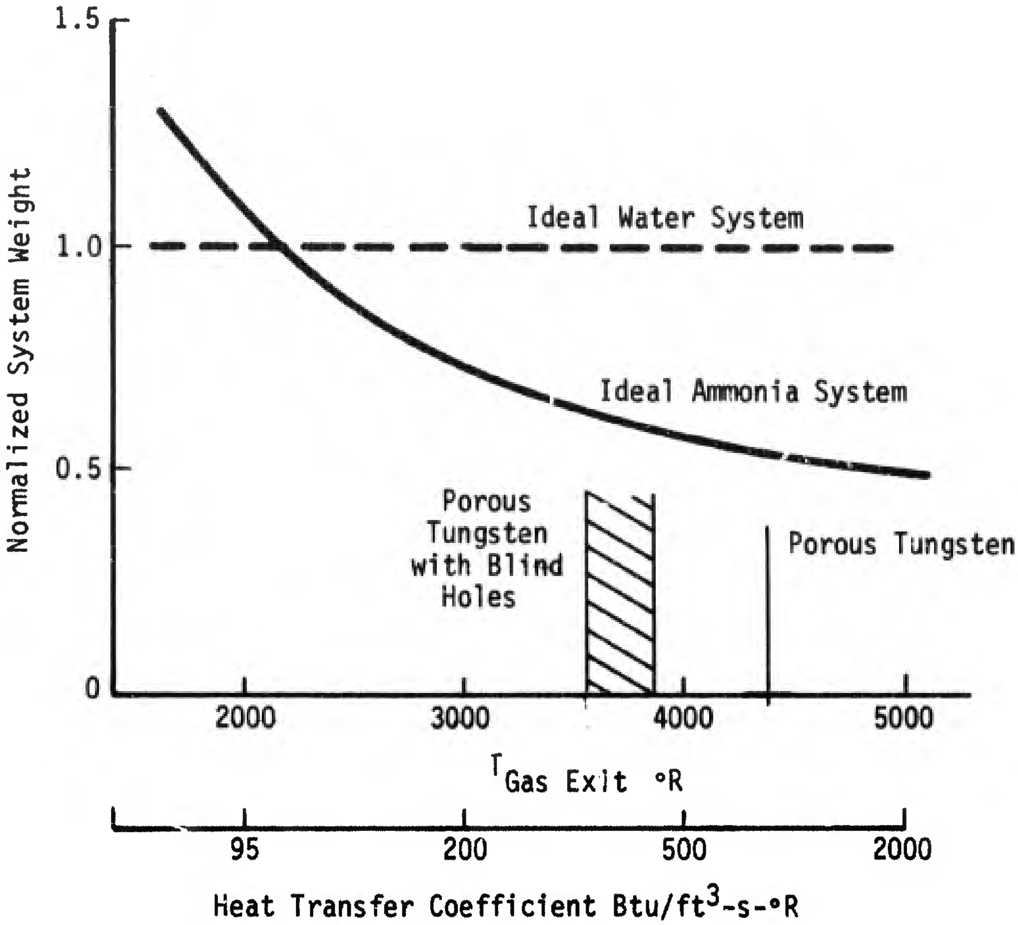

Figure 1. Transpiration Cooling System Weight Comparison

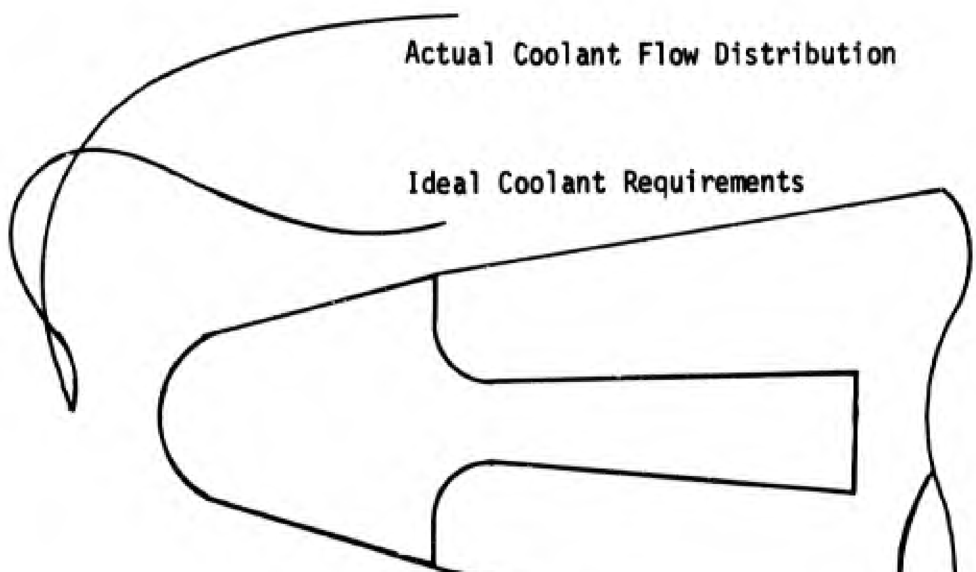

Figure 2. Mass Flow Variation Around the Nose Tip

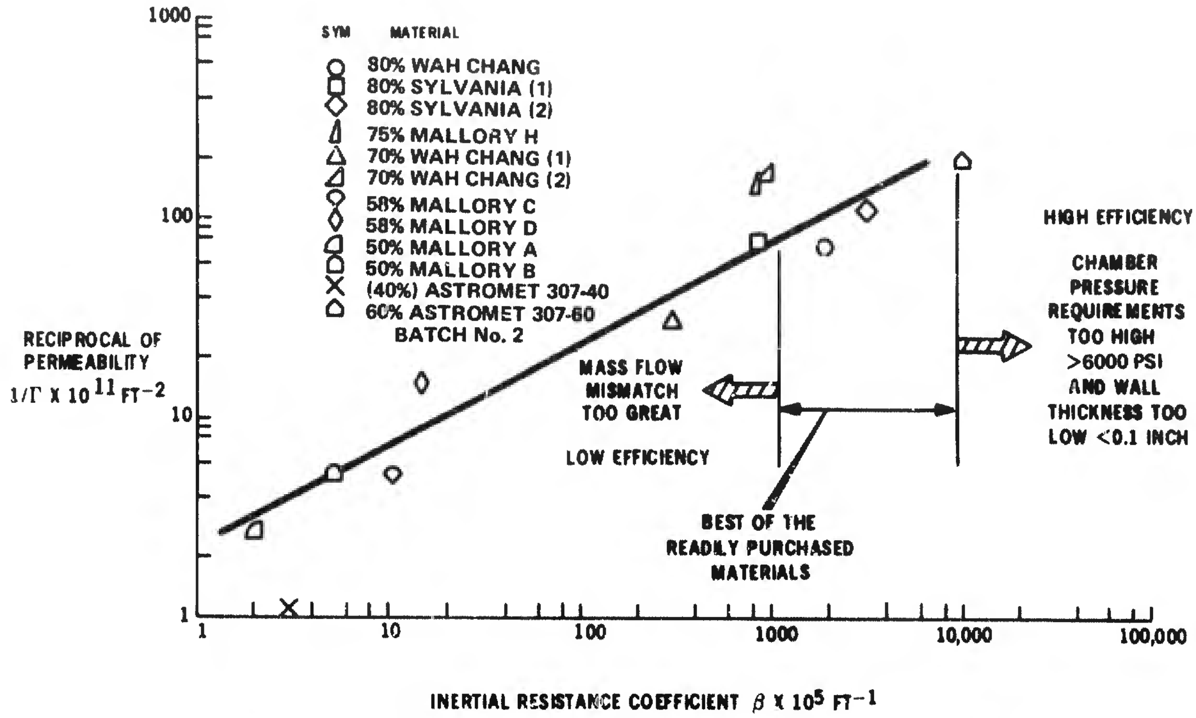

Figure 3. Flow Characteristic Correlation of Several Porous Tungsten Materials

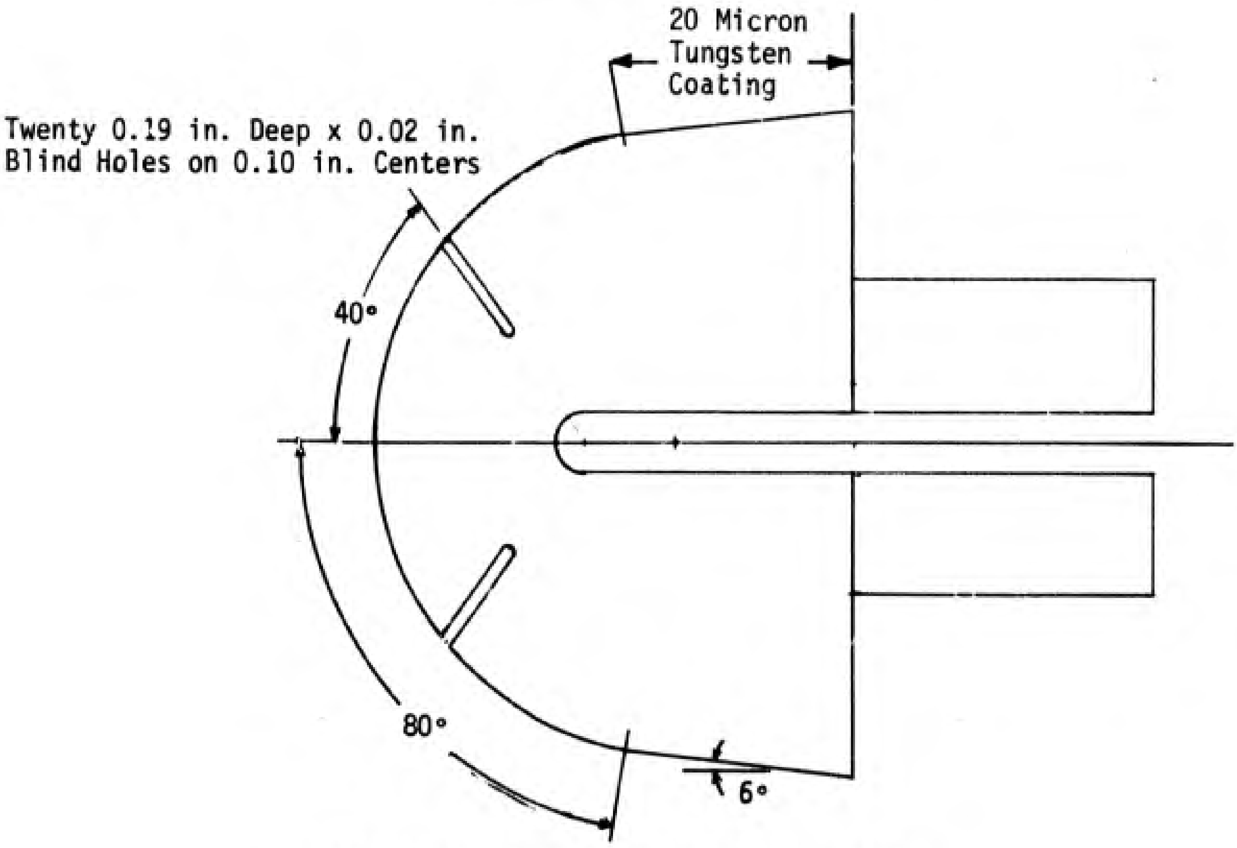

Figure 4. Nose Tip Conceptual Design

1. INTRODUCTION

1.1 Background

As the peak velocity of an ABM interceptor is increased, active cooling systems become increasingly attractive for use in nose tips and air vane leading edges (Reference 2). At currently anticipated burnout velocities for advanced interceptors the combination of severe thermal and pressure environments produces large recession rates with current interceptor nose tip and air vane leading edge materials. Coupled with this environment is a particle environment arising from both natural and induced causes which further increase surface erosion. Large recession rates directly affect vehicle performance. Excessive nose tip recession will create a vehicle center of pressure shift which can result in increased control system weights. Air vane blunting and area loss cause a large change in control force and hinge moment that also reflects in increased control system weights.

Candidate systems for the nose tip include reinforced phenolic passive tips and transpiration cooling. Candidate systems for the air vane leading edge include passive systems, refractory metals, and transpiration cooling, as shown in Figure 1-1. Transpiration cooled metal surfaces offer the advantages of reduced erosion because of their inherently high resistance to impact damage.

The use of a coolant transpired through a metal matrix wall as a heat protection surface for the nose tip of a hypersonic vehicle is not new and has been receiving considerable attention in recent years as a means of achieving a shape-stable nose tip for high ballistic factor reentry vehicles (References 3, 4, and 5). Ground and flight tests have been conducted on systems with water as the coolant and stainless steel as the matrix with the coolant introduced to the wall surface through either discrete holes or by distributed porosity. The basic principles are well proven and, although there are uncertainties in the downstream cooling effectivity of the fluid film layer and a required safety factor, transpiration cooling has been used in practice (Reference 5) to provide zero-recession nose tips under the most severe ICBM reentry conditions.

Although water has a relatively high efficiency as a coolant and has a good storage density, the work of Reference 6 shows that if water is replaced as a coolant with a reactive gas that is used with a high surface temperature matrix, numerous system benefits could theoretically be realized. These include lighter coolant weights and lighter expulsion system weights. A material that can operate at high surface temperature is an ideal matrix material since high surface temperatures greatly reduce the net incoming heat flux; also, with a material that can operate at a high temperature local

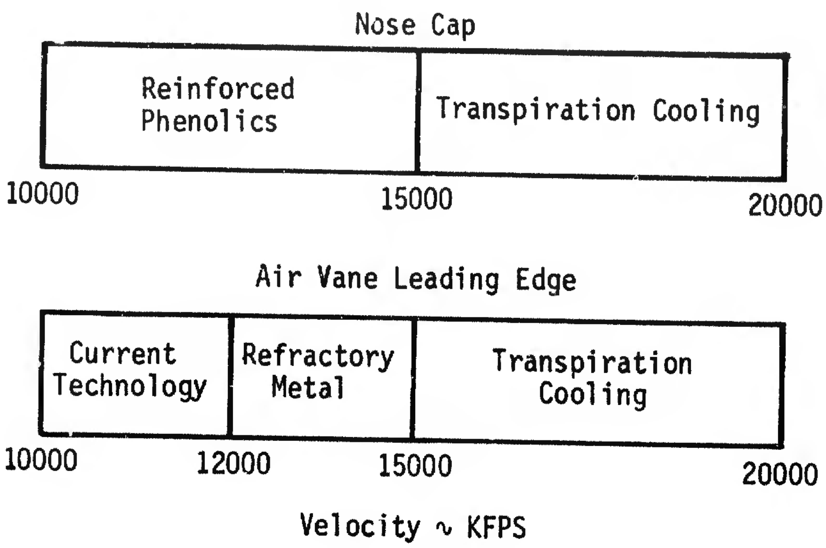

Figure 1-1. Candidate ATI Systems

hot spots are not catastrophic. A porous refractory metal such as tungsten would be an excellent material for this application except that at high surface temperatures tungsten must be protected from attack by the boundary layer oxygen.

The CONAP concept which combines the reactive coolant, ammonia, with the high temperature tungsten matrix depends upon the ability of the injected coolant to greatly reduce or shut off the flow of oxygen reaching the refractory hot wall. A series of tests were conducted to demonstrate experimentally the feasibility of this concept (Reference 7). The results of these tests showed that at a heat flux of 3500 Btu/ft^2-s and an enthalpy of 4000 Btu/lb, no measurable recession occurred in a 5-second test where ammonia was used to deplete oxygen at the surface of a porous tungsten matrix. As a result of these tests, system development tasks were defined to provide the data required to perform a design of an actual tip or air vane leading edge. These tasks included the evaluation of the flow characteristics which control the mass flow distribution within the porous tungsten matrix and the evaluation of the internal heat transfer coefficient which controls the amount of heat absorbed by the coolant as it passes through the matrix. The importance of knowing the internal heat transfer coefficient is demonstrated in Figure 1-2 which summarizes a system weight comparison between a water system and a CONAP system. The comparison is made parametrically as a function of gas exit temperature which has a direct correspondence to the internal heat transfer coefficient. The weight comparison, which is normalized to the water system, shows that if heat transfer coefficients are high, on the order of 1000 Btu/ft^3-s-°R at the flow rates of interest (around 5 lb/ft^2-s), a weight savings of 50 percent could be realized by using the CONAP system. Low internal heat transfer coefficients of CONAP, however, would make the CONAP concept less attractive. A knowledge of the values of heat transfer coefficient as a function of coolant mass flux was therefore essential.

Equal importance is placed on the definition of the flow characteristics - permeability and inertial resistance coefficient - of the available porous tungsten materials. The flow characteristics of a material and the modifications to those flow characteristics, such as blind hole augmentation and surface porosity variations through vapor deposition, greatly influence the coolant mass flow distribution that will be delivered.

Once these parameters are defined a selection of the optimum materials can be made.

1.2 Study Objectives

This study was initiated to acquire the data necessary to assess the performance of a nose tip or air vane leading edge in a flight environment. An overall experimental approach has been taken with a series of laboratory tests to provide the required data.

The specific objectives of this study are to:

1. Determine the flow characteristics (permeability and inertial resistance coefficient) of all materials and concepts considered

2 Determine the internal heat transfer coefficient for an ammonia gas passing through the tungsten matricies considered

3 Evaluate and optimize several tungsten matrix material concepts which include a wide range of porous materials, materials with discrete holes, materials that combine porosity with discrete holes, and materials whose surface is vapor deposited with another material

4 Establish CONAP system efficiency for these material concepts through the use of the flow characteristic and heat transfer coefficient data

5 Select those concepts and those combinations of concepts which show the most promise for future system use

6 Define the test model configurations for further work in plasma arc tests at low and high pressure.

1.3 Approach

The test plan devised to meet the objectives of this program considers both porous tungsten and discrete hole tungsten matricies. Obtaining and verifying internal heat transfer coefficients and flow characteristics for both discrete hole and porous matricies allows the greatest latitude of design in future system applications. Discrete hole matrix concepts, although not nearly as efficient in conserving system coolant weights as porous materials, have much greater strength capability. In the event that this becomes the predominate requirement for some systems due to its anticipated superior erosion capability, data were taken to verify the fact that standard pipe flow and heat transfer coefficients can be used or easily modified to adequately predict both ammonia flow coefficients and heat transfer data while ammonia is flowing through a discrete hole in a hot tungsten matrix.

In the flight application the pressure and heat transfer distributions around a porous nose tip and air vane leading edge create a need for the coolant/matrix system to deliver only a required amount of flow to each area. Porous materials, although very efficient as compared to discrete holes, could be even more efficient if the flow characteristics could be varied within the matrix to minimize the mass flow variation as illustrated in Figure 1-3. No materials are currently available with a variable permeability and significant development is required to create this capability. The approach taken to minimize the flow variation was to use existing materials and modify their basic flow properties. Consequently, two concepts were added to the basic porous matrix concept to provide a more efficient system. Augmented holes were considered for use in areas where the flow requirements were high; vapor deposition of tungsten was considered for use in areas where the flow rate requirements are low. Flow augmentation was accomplished with the addition of blind holes which were not drilled completely through the material but only drilled partially into the matrix material. This concept was considered because it was anticipated that flow

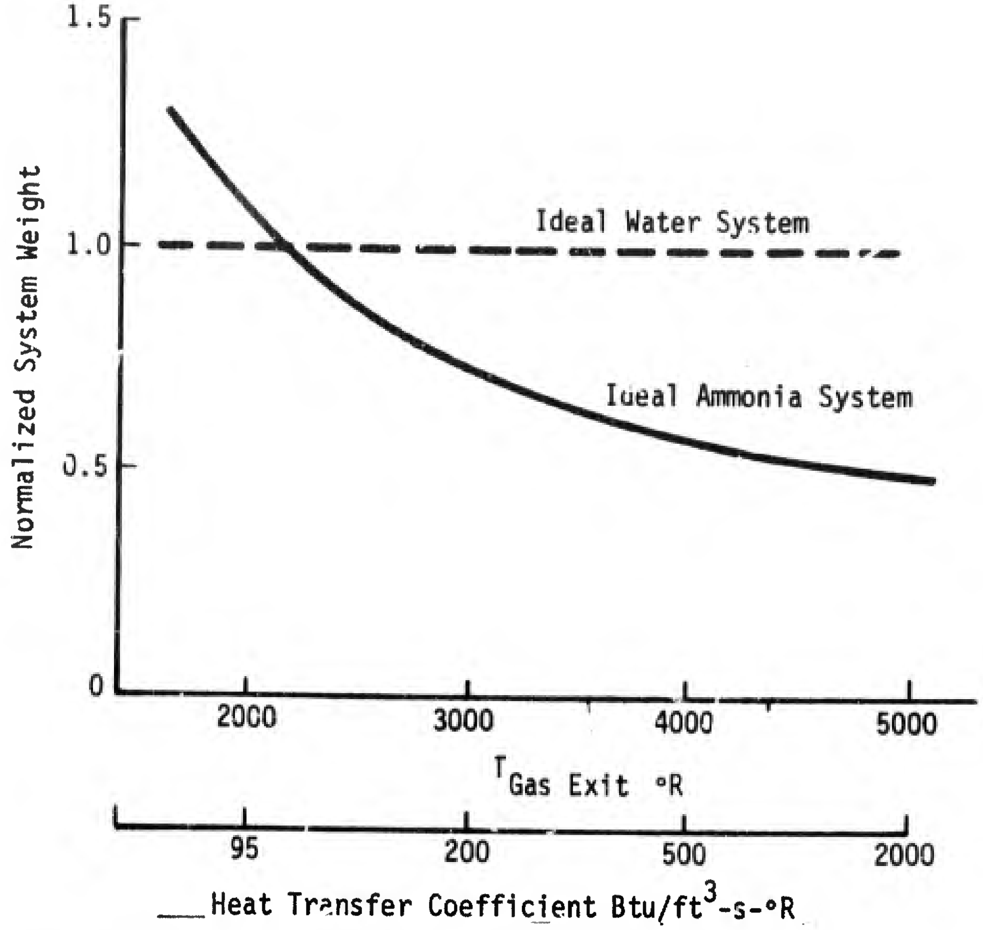

Figure 1-2. Transpiration Cooling System Weight Comparison

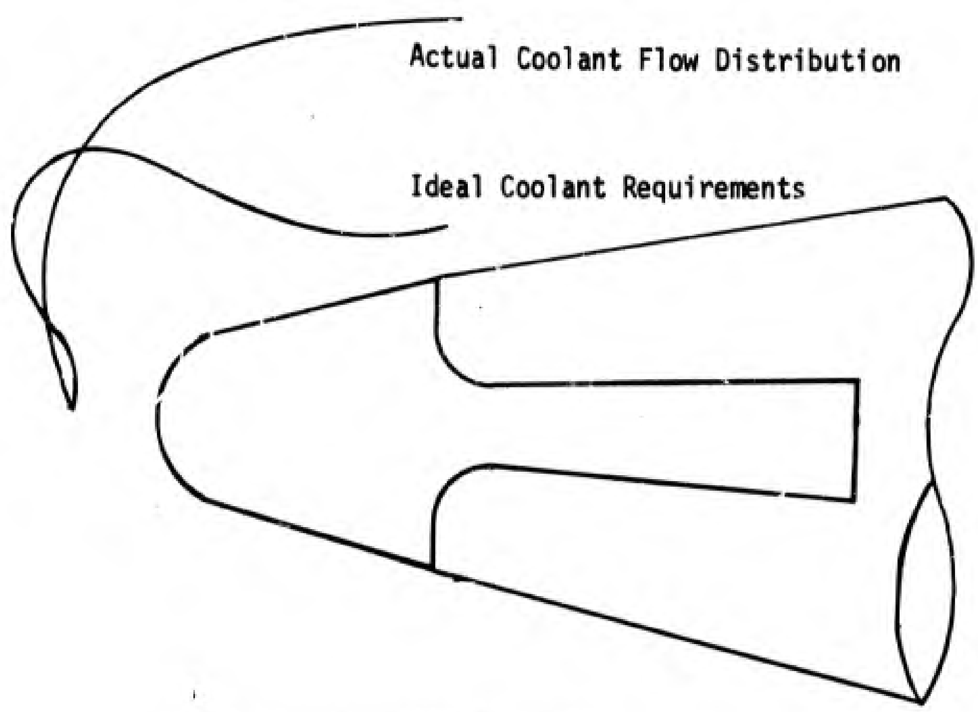

Figure 1-3. Mass Flow Variation Around The Nose Tip

rates could be increased in a local area without significant degradation of the heat transfer coefficient in that area. The second method by which local flow can be controlled is by depositing tungsten vapor onto the surface pores and decreasing the surface porosity. With this concept, a vapor is deposited on the surface of the porous tungsten and adheres to and effectively enlarges the grains. This concept decreases the flow in a local area without greatly affecting the heat transfer coefficient. This type of concept is useful in the sidewall region of a nose tip or air vane leading edge, where a decrease in coolant flow is desireable, because the high pressure potential across the porous wall forces more coolant through the wall than is required to neutralize the low heat rate. Both of these concepts can greatly aid in tailoring the flow to minimize the variation between actual coolant flow and required coolant flow.

Table 1-I shows the material concepts on which heat transfer coefficient tests and the flow characteristics tests were conducted.

TABLE 1-I

Matrix Concepts and Configurations

Matrix Concept	Configuration	Flow Direction
Porous tungsten	1/4 in. 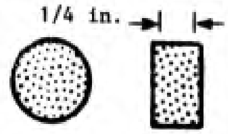	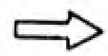
Porous tungsten augmented with blind holes	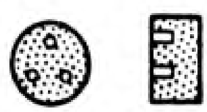	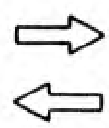
Tungsten copper with one discrete hole	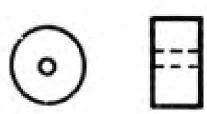	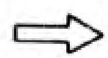
Tungsten copper with patterned discrete holes	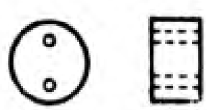	
Porous tungsten with flow control by vapor deposition	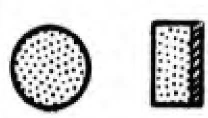	

2. MATERIAL DESCRIPTION

Two types of commercially available porous tungsten materials were evaluated in this study. Astro Met Associates supplied tungsten material that was manufactured to final shape in the porous state. This material required no further processing prior to use as test specimen. The other type of material used was tungsten-copper, which consisted of an interconnected pore tungsten matrix, infiltrated with copper. This material was received in bar stock from which the specimen was machined. Further processing of this material was required to extract the copper; however, machining was performed prior to the extraction of the copper. The tungsten copper material was obtained from three suppliers, Wah Chang, Sylvania, and Mallory Metallurgical.

Copper removal was performed in a vacuum furnace in which the samples were inductively heated to 2550°F in a 0.5 x 10^{-5} mm Hg vacuum. A total of four hours was required to melt and evaporate the copper. Prior to the evaporation process, and at intervals during the process, the samples were etched with a nitric acid-water solution to expedite the copper removal process. The initial etch was 24 hours while subsequent etches, generally three in number, were about 1/4 hour each. A detailed description of the equipment used can be found in Appendix B.

A material description and metallographic evaluation of the materials supplied by the various vendors follows:

2.1 Wah Chang

The Wah Chang tungsten-copper materials obtained were 80 volume percent tungsten – 20 volume percent copper, and 70 volume percent tungsten – 30 volume percent copper. Scanning electron micrographs taken of the surface of these Wah Chang materials are shown in Figures 2-1 through 2-6. Figures 2-1 through 2-3 show the 80 percent tungsten augmented with blind holes. The tungsten appears very uniform in structure and porosity, and no evidence exists that the placement of the hole in the sample distorted the surface or in anyway harmed the sample.

Figures 2-4 through 2-6 are similar photographs for the 70 volume percent tungsten material. Again the uniformity is very good, although not as good as the 80 percent tungsten. For both materials, the pore size appears to be 3 to 8 microns. Although these samples were tested at high temperatures, particle surfaces have edges which are quite angular and appear rough. Apparently, the material uniformity permitted adequate gas flow to prevent melting or smoothing of the material surfaces by diffusion.

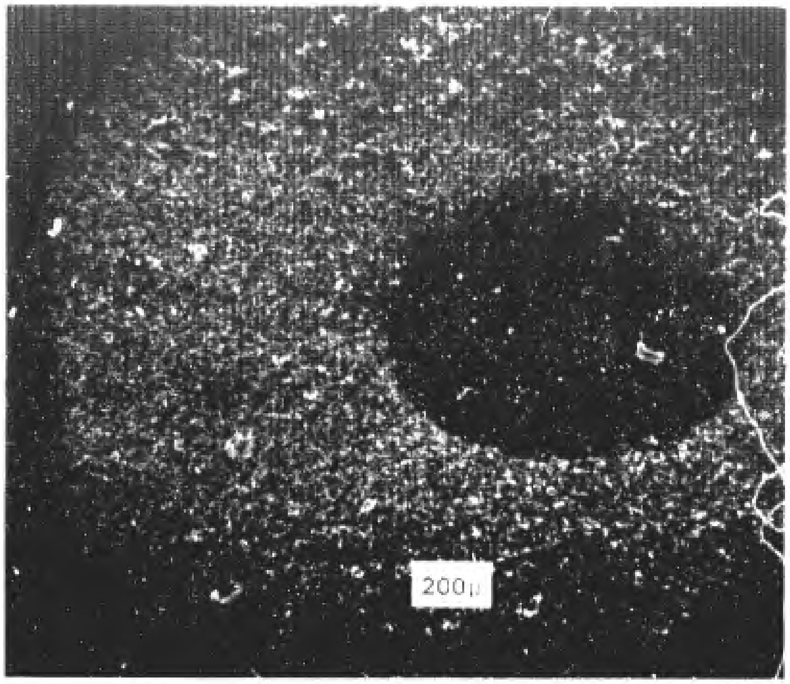

Figure 2-1. Scanning Electron Micrograph of Surface of Porous Tungsten Sample Wah Chang, 80 Volume Percent, Showing a Typical Blind Hole; 60X

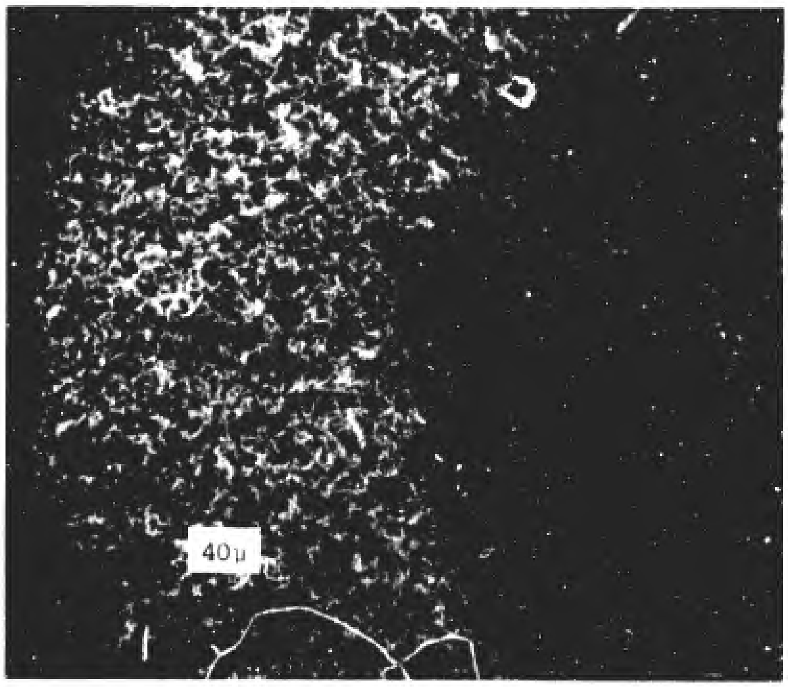

Figure 2-2. Typical Blind Hole, 80 Percent Wah Chang, 250X

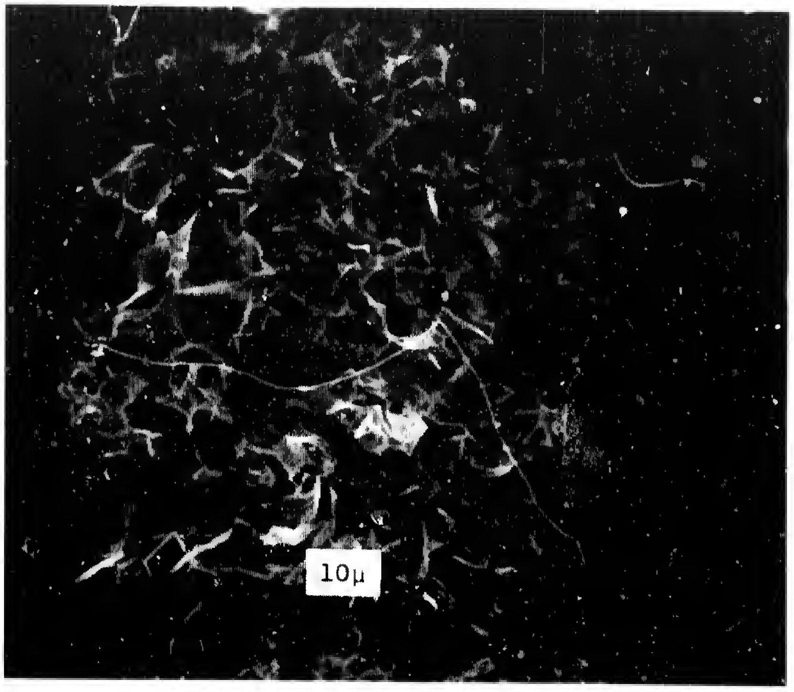

Figure 2-3. Typical Blind Hole, 80 Percent Wah Chang, 1000X

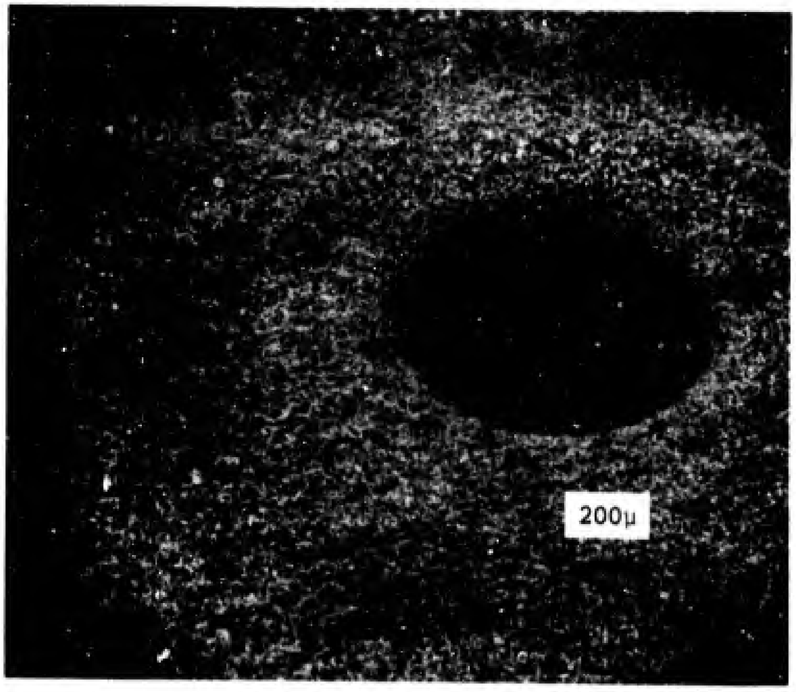

Figure 2-4. Typical Blind Hole, 70 Percent Wah Chang, 50X

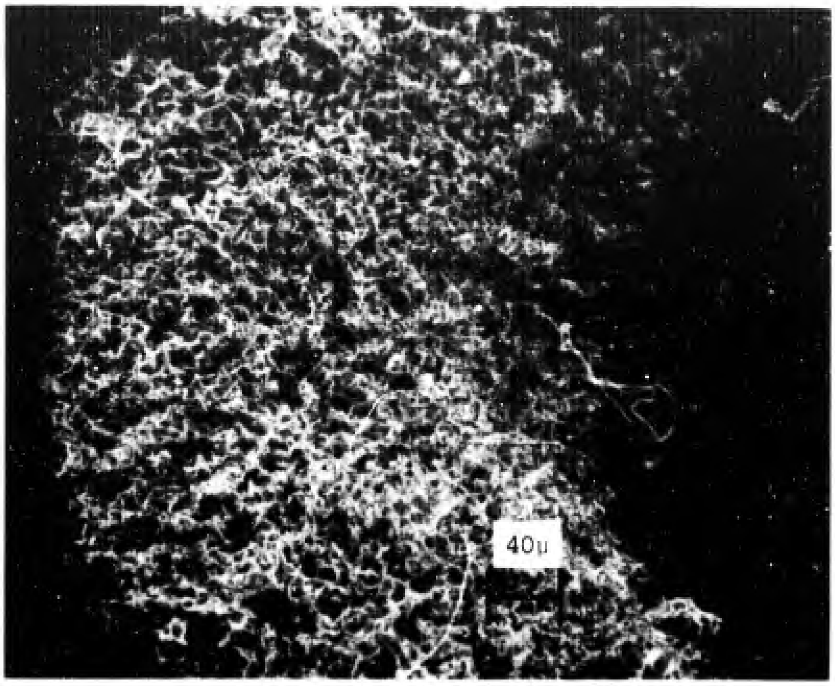

Figure 2-5. Typical Blind Hole, 70 Percent Wah Chang, 250X

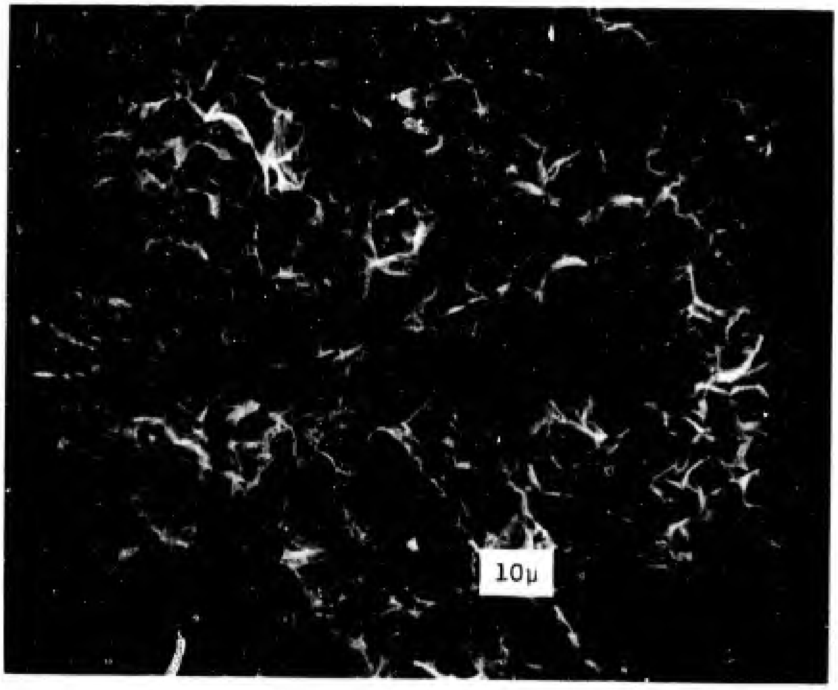

Figure 2-6. Typical Blind Hole, 70 Percent Wah Chang, 1000X

2.2 Sylvania

Sylvania also produces an alloy of 80 volume percent tungsten - 20 volume percent copper. The Sylvania material, Figures 2-7 and 2-8, appears as uniform or perhaps even more uniform than the Wah Chang tungsten. The surfaces are rough and angular, but these samples were not heated to elevated temperatures. Note that in every case where ''untested'' is specified, elevated temperature testing was not done on the particular sample photographed. The original particle size of the Sylvania material appears to be much the same as the Wah Chang tungsten. The Sylvania pore size seems to average 3 to 5 microns in diameter.

2.3 Astro Met Associates, Inc.

Astro Met makes several series of porous materials with tungsten. These series (100, 300, and 500) represent different initial powders and different proprietary processing methods. Properties, including permeability and inertial resistance coefficient, are variable within any one series.

Three types of tungsten were ordered from Astro Met in the form of cylinders, 1/2 inch diameter by 1/4 inch thick. Six samples of each type of series were to be furnished, final machined to size. The types were 10/15-60, 307-40, and 307-60. Although processing is proprietary to Astro Met, the following information is known. Type 10/15-60 is a 100 series material with 15 micron pores forming interstital tetrahedra among particles roughly blocky and spherical shape. The density is 60 percent of theoretical. This material was fabricated, machined to size, and received for test. Type 307-40 is a 300 series material with pores about 7 mils in size, forming blocky voids with channels about 0.1 the diameter of the voids. The particles tend to be tetrahedral in shape and the material is 40 percent of theoretical density. The 307-60 material is also a 300 series material and is very similar to the 307-40 material. The density, however, is 60 percent of theoretical, the permeability is lower, and the inertial resistance coefficient is higher.

Astro Met samples are shown in Figures 2-9 through 2-28. Figures 2-9, 2-10, and 2-11 show the 307-40 material. In addition to the finer pores of 10 to 20 microns, shown in Figures 2-10 and 2-11, pores as large as 200 microns may be seen in Figures 2-9 and 2-10. These large pores, which appear to be distributed fairly uniformly, tend to increase the permeability of the specimen. Figure 2-11 shows the tungsten grain boundaries, which do not necessarily correspond to the original particle boundary. The tungsten surfaces are relatively smooth and rounded in comparison to previous photographs and, as will be shown later, in comparison to some of the other Astro Met material. This implies that the high temperature testing may have caused some surface fusion or diffusion.

The 10/15-60 material is shown in Figures 2-12, 2-13 and 2-14. This porous tungsten is much more uniform than the 307-40 material and all pores seem to be approximately 15 microns in size. The surfaces of this sample are also rounded and smooth. In Figure 2-14, some grain boundaries may be seen although generally each particle is one grain. Some additional grains apparently resulted from recrystallization at the points where particles touched. The flow characteristics of this material allowed excessive coolant flow rates for a given pressure drop across the specimen, and thus the material was not considered for ultimate usage.

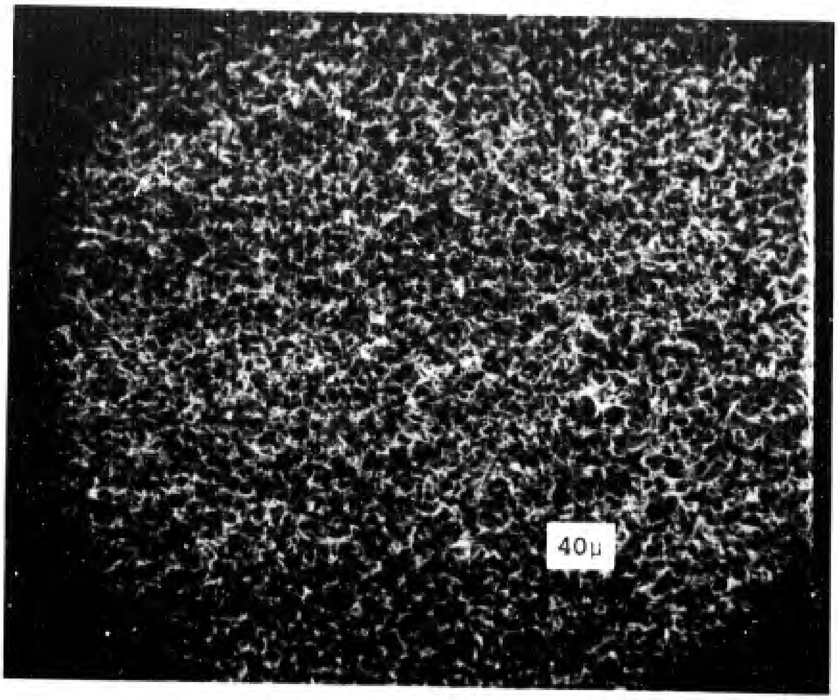

Figure 2-7. Untested 80 Percent Sylvania, 250X

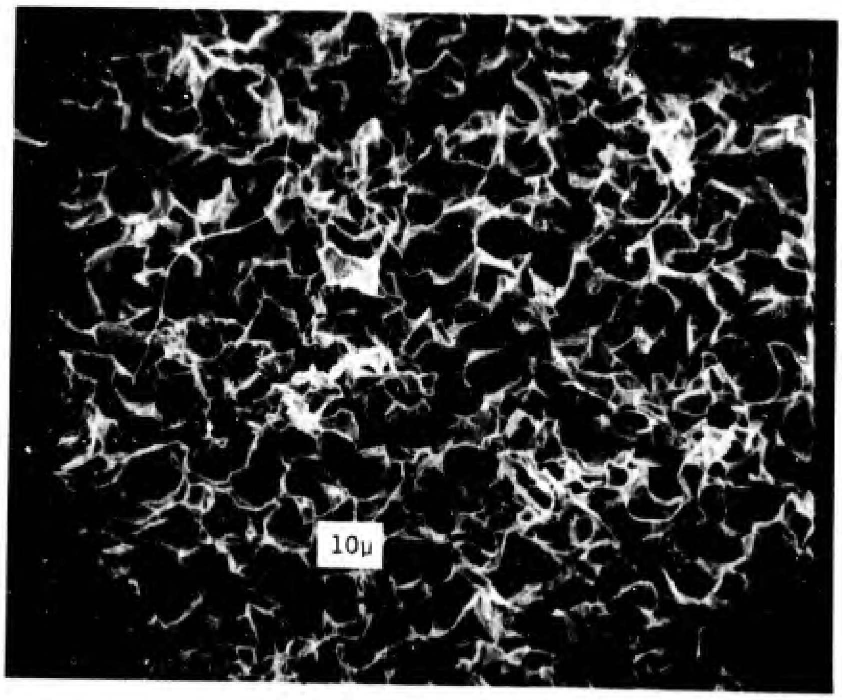

Figure 2-8. Untested 80 Percent Sylvania, 1000X

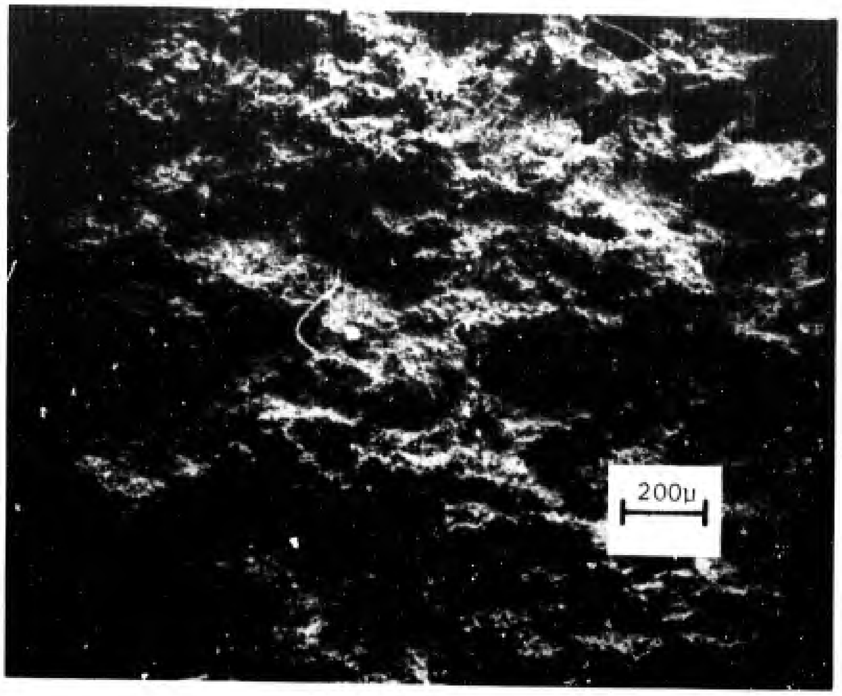

Figure 2-9. Astro Met 307-40, 50X

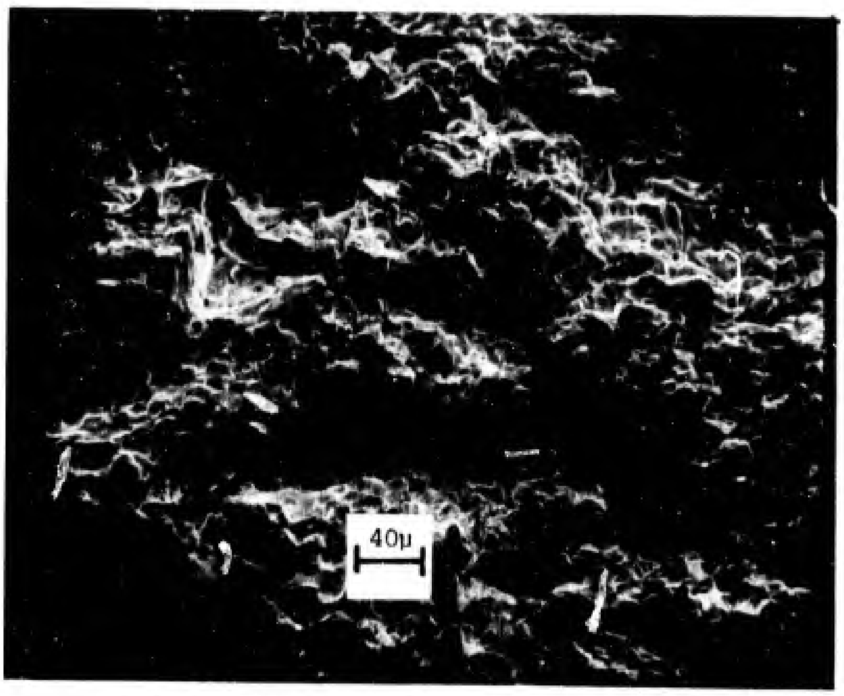

Figure 2-10. Astro Met 307-40, 250X

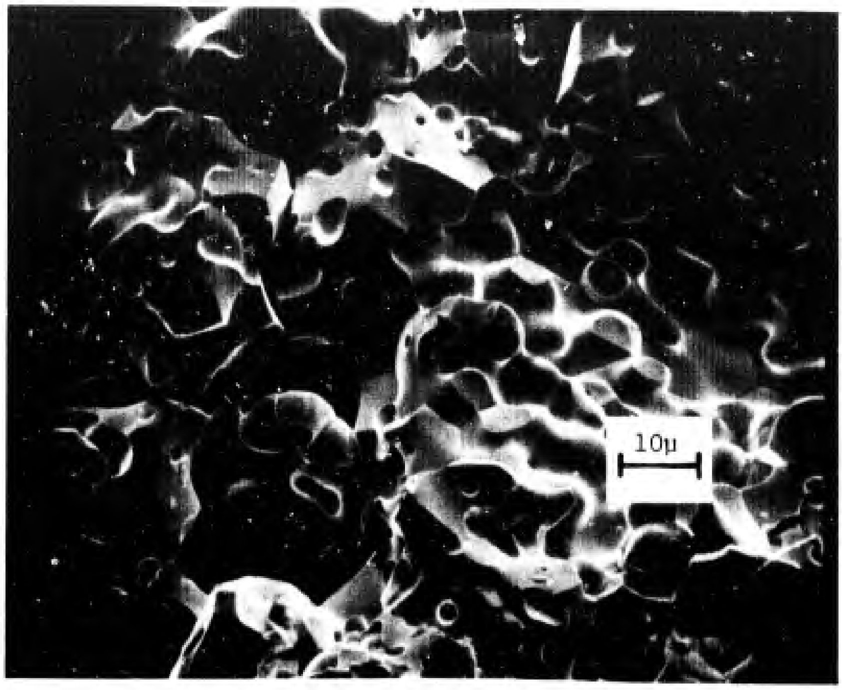

Figure 2-11. Astro Met 307-40, 1000X

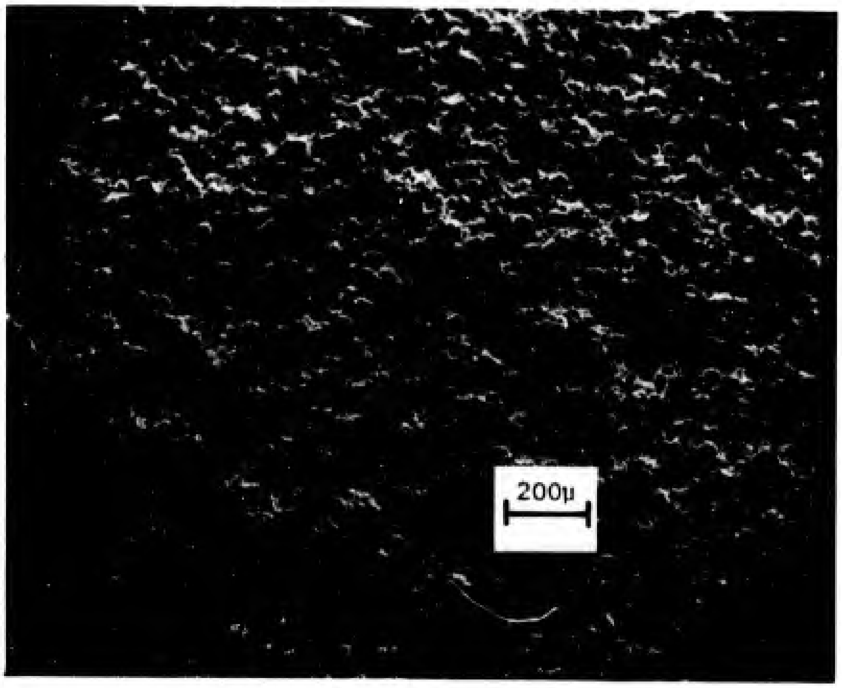

Figure 2-12. Astro Met 10/15-16, 50X

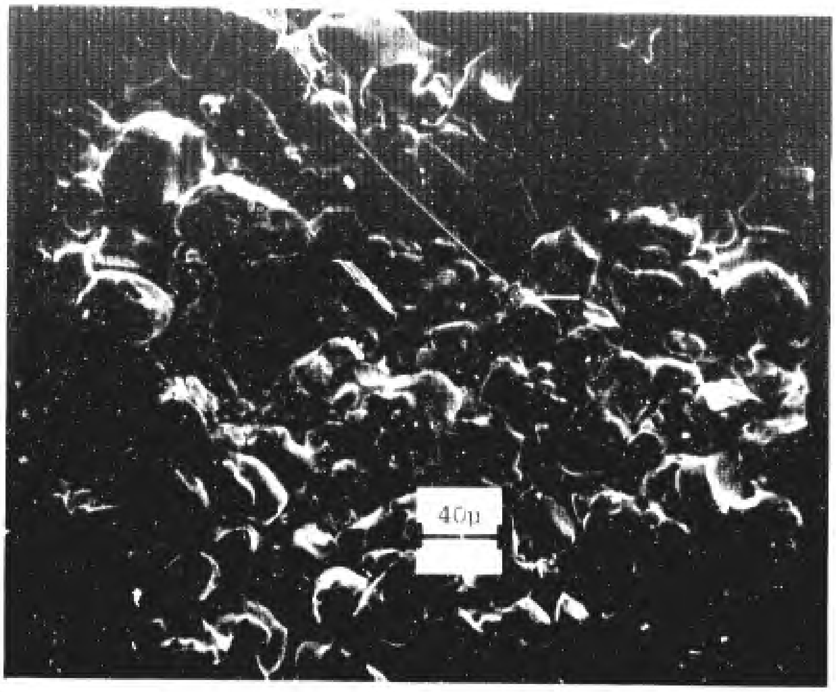

Figure 2-13. Astro Met 10/15-16, 250X

Figure 2-14. Astro Met 10/15-16, 1000X

The 307-60 material was supplied in two batches. The 307-60 batch No. 1 material is shown in Figures 2-15, 2-16 and 2-17. Here the surface is smooth and rounded. This porous tungsten is similar to 307-40 except for density. The 307-60 material (Figure 2-15) has a few scattered large holes of a maximum of 200 microns in diameter, similar to the large pores of 307-40 material. Figure 2-15 shows the machining marks on the surface. In Figure 2-17, a few scattered small holes, approximately 10 microns, may be seen. Again, the structure does not seem to be uniform and homogeneous. Grain boundaries may be observed in Figure 2-17; the grains appear to be smaller on the average than the particles of Figure 2-9. The flow characteristics of the 307-40 and the 307-60 batch No. 1 materials are comparable. Figures 2-18 through 2-20 illustrate 307-60 material which has not been exposed to high temperature testing. Again, the surface shows a rough and angular nature. Figures 2-21 and 2-22 show the 307-60 batch No. 2 material in the untested condition. The coarse and fine holes are apparent just as in previous samples. The batch No. 2 307-60 material has a much lower permeability and a much higher inertial resistance coefficient than either the 307-60 batch No. 1 or the 307-40 materials, as will be shown in Chapter 3.

To show the effect of a vapor deposited coating, gold was applied to a sample of the batch No. 2 307-60 (Figures 2-23 and 2-24). This coating has little effect on the large pores, but as seen in Figure 2-24 the coating fairly well plugs any of the very fine holes. The nodular-growth nature of the vapor deposit is apparent. The gold coating, as expected, decreased the flow through the porous matrix.

2.4 Mallory Metallurgical Company

Mallory produces several tungsten-copper alloys; eight alloys of varying density and fabrication techniques were supplied, from which samples were machined and the copper extracted by the method given above. Table 2-I outlines the sample configurations. Regular sintering was done at temperatures less than 2400°F, while high temperature sintering was done at about 2400°F.

TABLE 2-I

Tungsten-Copper Material Produced by
Mallory Metallurgical

Sample Designation	Volume Percentage of Tungsten	Process Designation
A	50	3W3 regular temperature
B	50	3W3 high temperature
C	58	10W3 high temperature
D	58	10W3 regular temperature
E	64.6	30W3 high temperature
F	64.6	30W3 regular temperature
G	80	50W3 regular temperature
H	75	40W3 high temperature

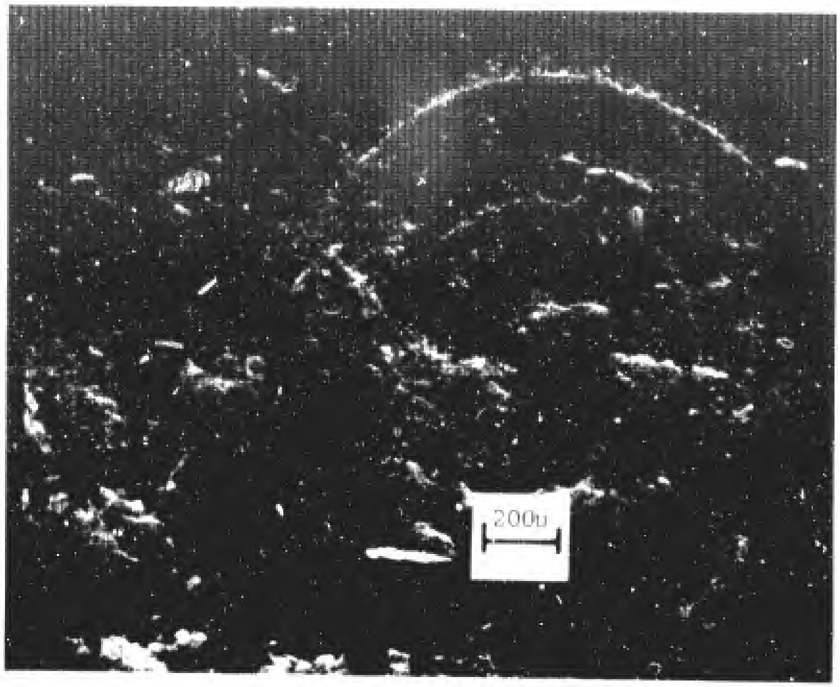

Figure 2-15. Astro Met 307-60, 50X

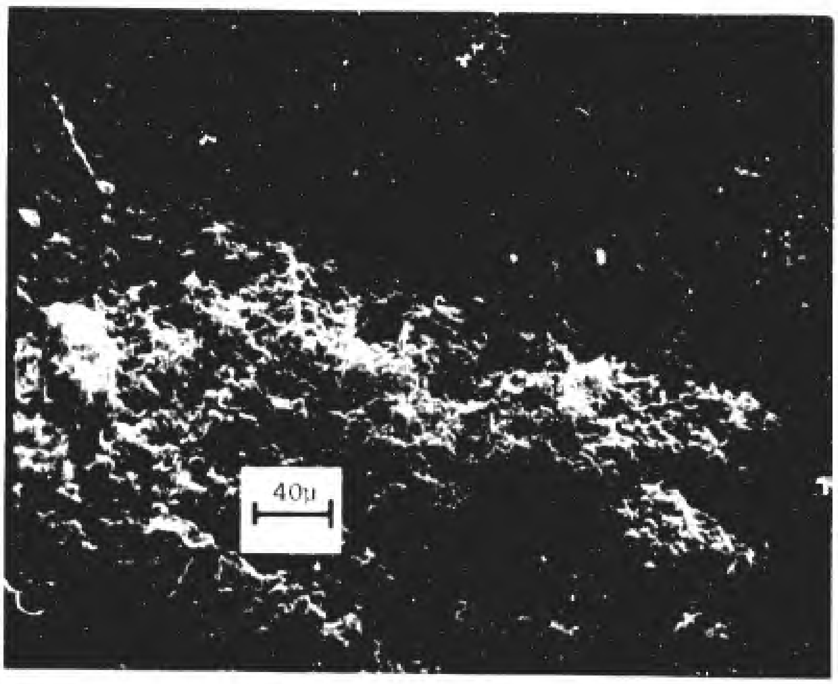

Figure 2-16. Astro Met 307-60, 250X

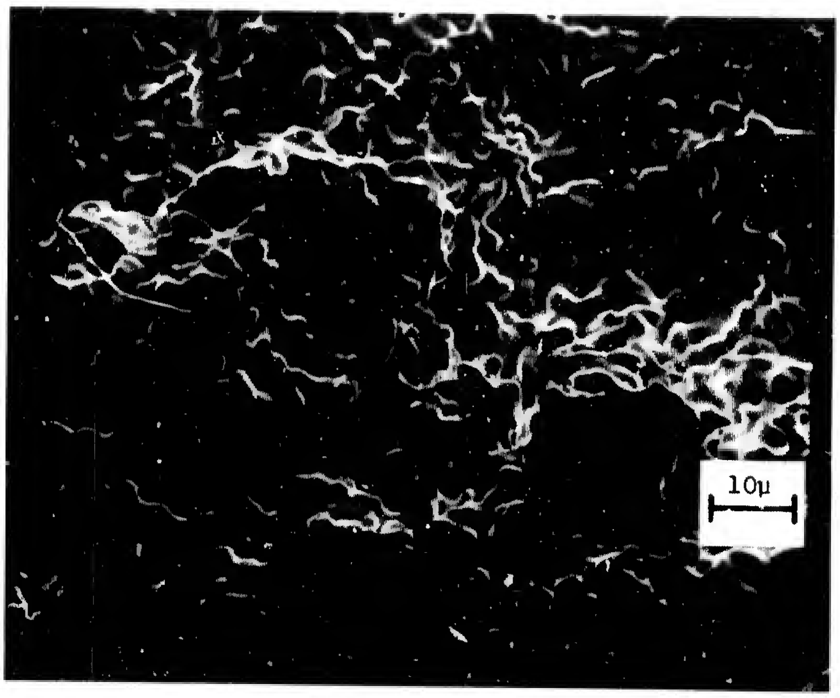

Figure 2-17. Astro Met 307-60, 1000X

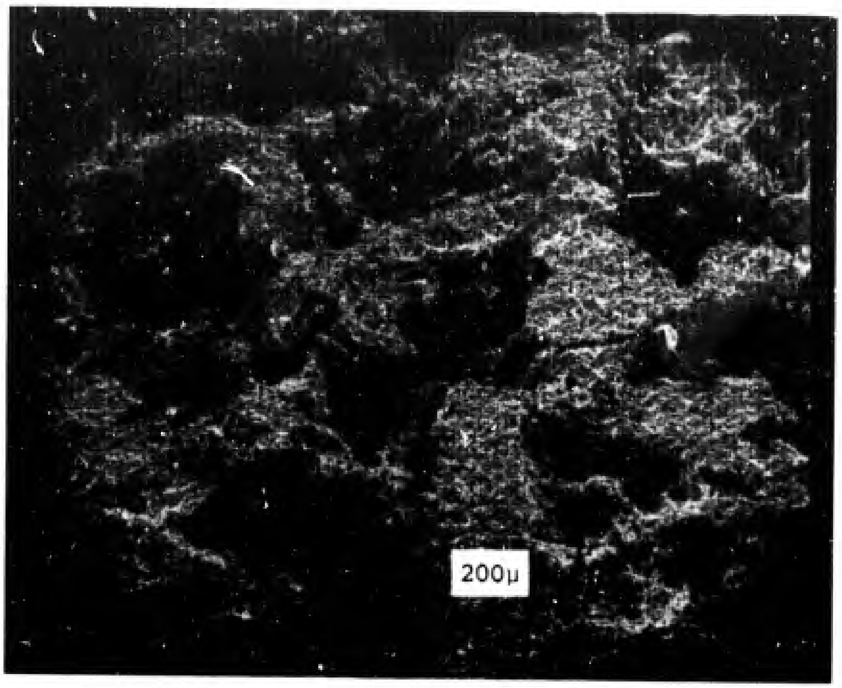

Figure 2-18. Untested Astro Met 307-60, 50X

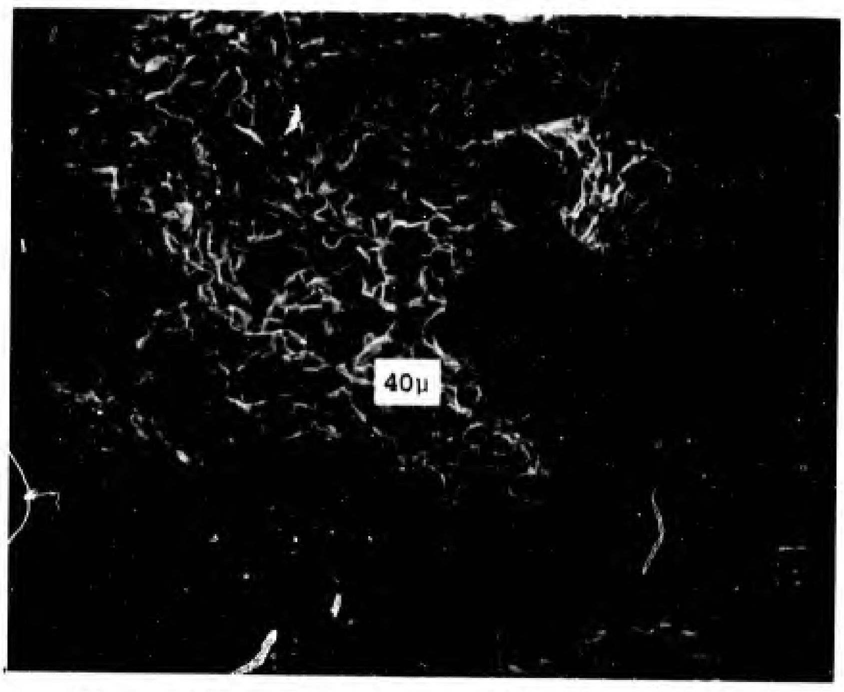

Figure 2-19. Untested Astro Met 307-60, 250X

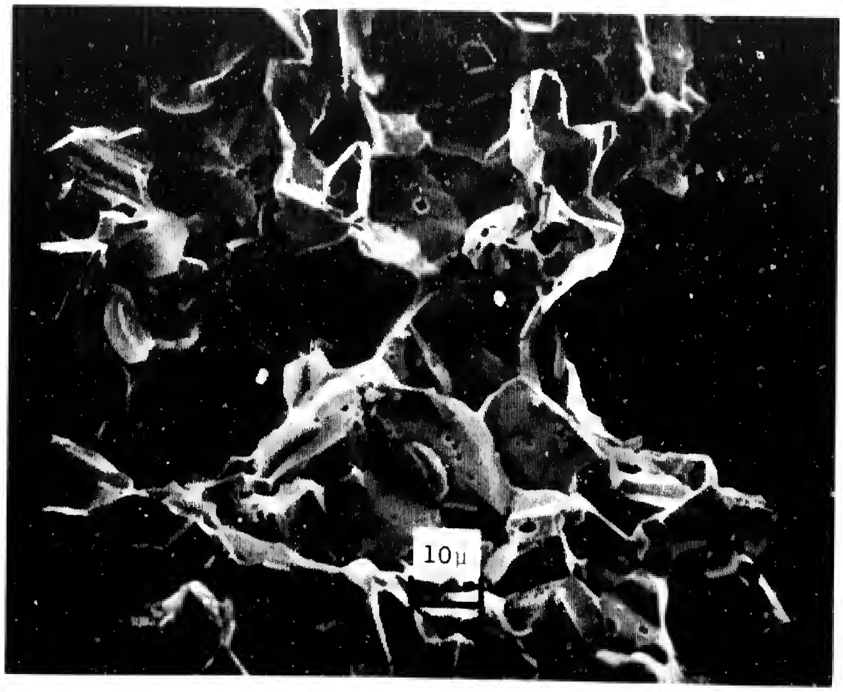

Figure 2-20. Untested Astro Met 307-60, 1000X

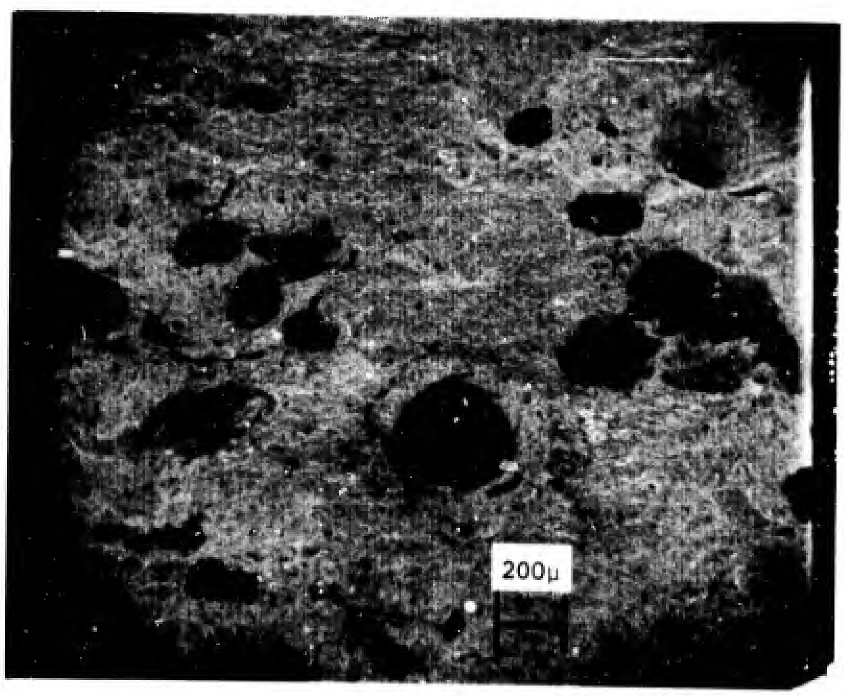

Figure 2-21. Untested Astro Met 307-60,
Batch 2, 50X

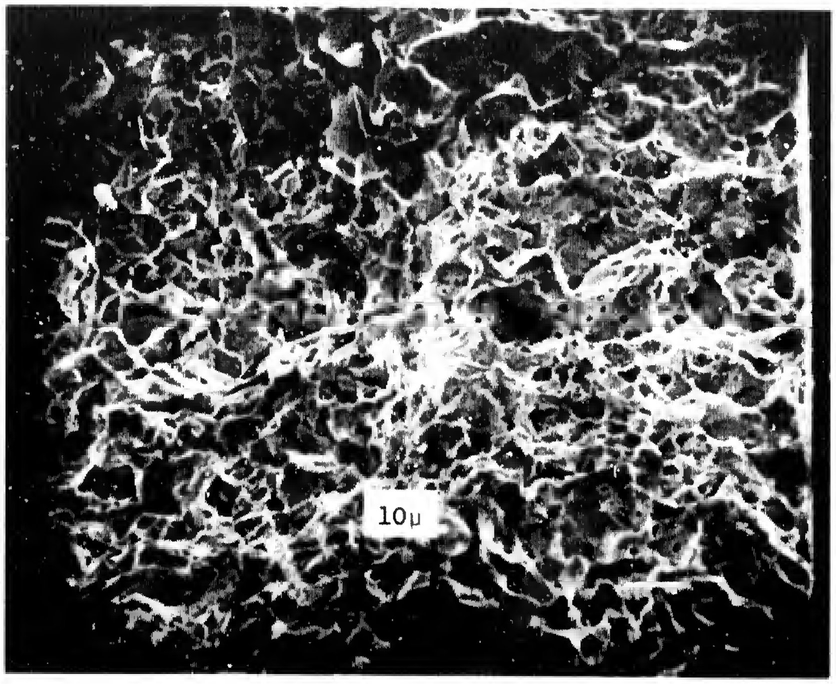

Figure 2-22. Untested Astro Met 307-60, Batch 2, 1000X

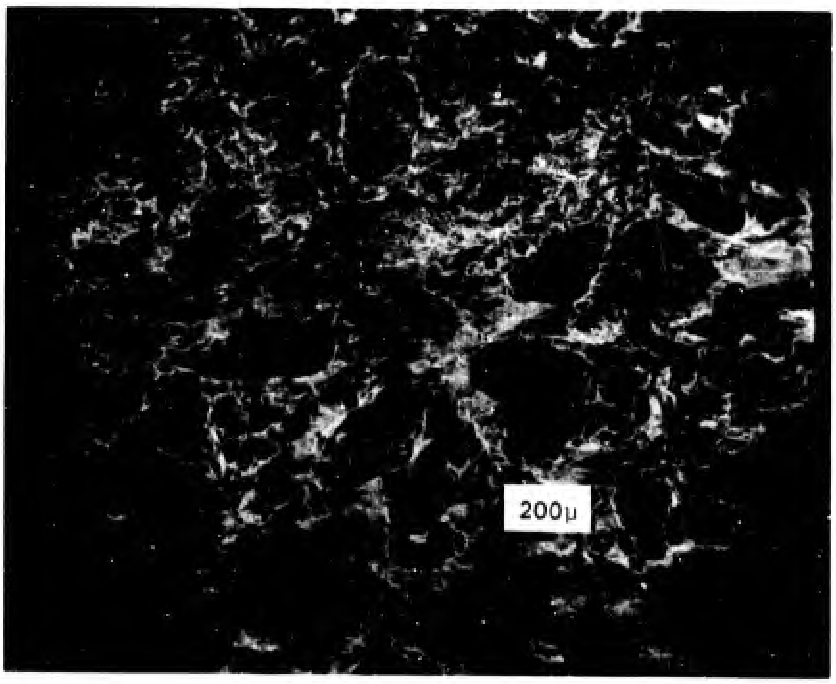

Figure 2-23. Untested Astro Met 307-60, Batch 2, Vapor-Deposited Gold on Surface, 50X

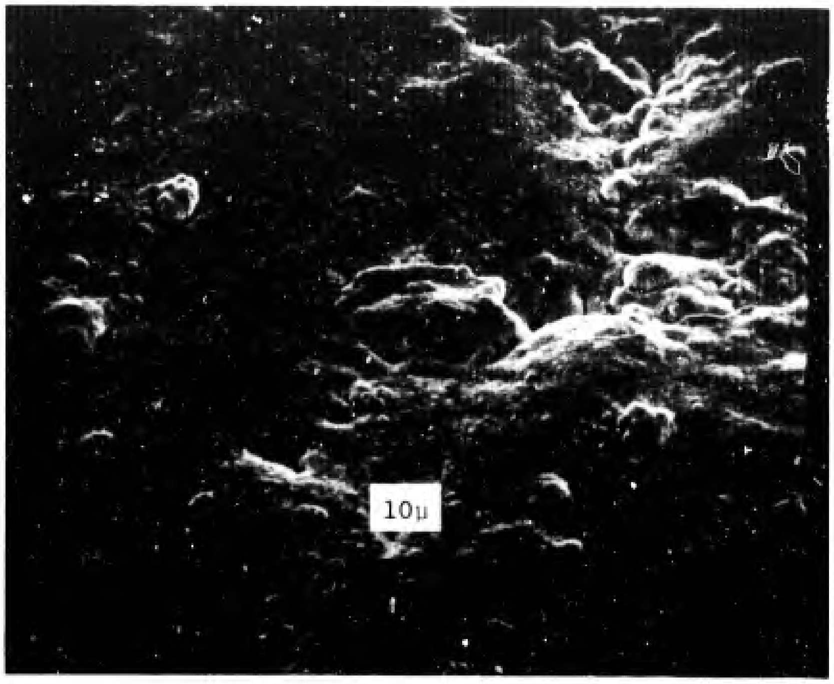

Figure 2-24. Untested Astro Met 307-60, Batch 2, Vapor-Deposited Gold on Surface, 1000X

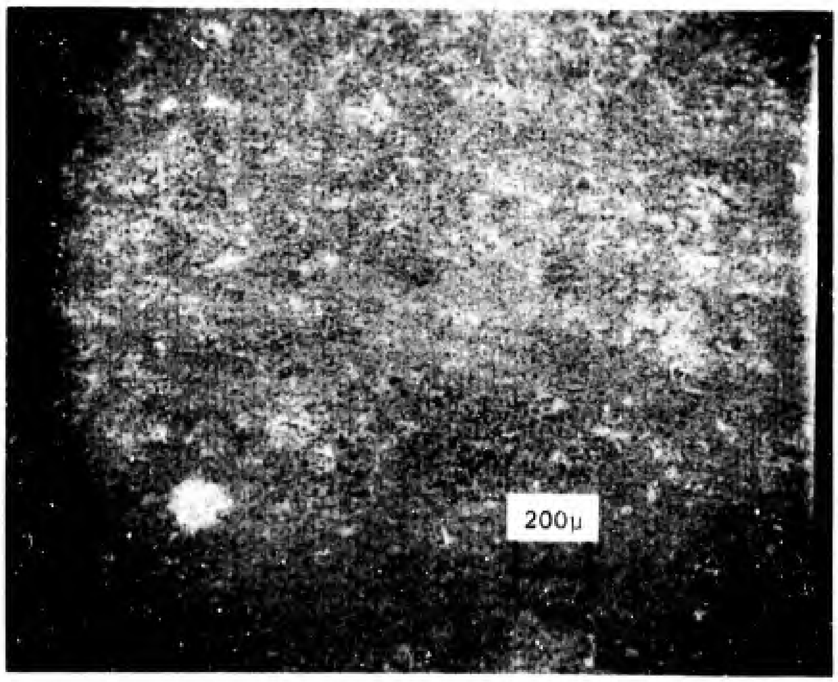

Figure 2-25. Mallory A, 50X

All of the Mallory material is very uniform in nature. Mallory A, Figures 2-25 and 2-26, appears to have been made from very fine powder and is quite porous, as would be anticipated from the low density of 50 percent. The larger pores average about 5 microns in size. Mallory C material, Figures 2-27 and 2-28, has pores of about the same size, 5 microns, but the particle size appears larger, apparently resulting from sintering at the high temperatures or starting with a coarser particle. In Figure 2-27 some surface contamination is seen. Epoxy was used to bond the samples into a holder to take Schlieren photographs and removing the samples afterwards without contaminating the surface was difficult.

Several of the Mallory materials were coated from 1 to 5 microns in thickness by tungsten vapor deposition. The Mallory D material which was vapor deposited with tungsten is shown in Figures 2-29 through 2-32. Again the base material is very porous, is uniform, and has pores as large as 10 microns. The nodular nature of the vapor deposited tungsten is readily seen at the higher magnifications, particularly in Figures 2-31 and 2-32. For comparison the uncoated side of sample D is shown in Figure 2-33, which may be compared directly with Figure 2-31. The tungsten vapor deposit reduced the size of the pores in the primary structure by enlarging the tungsten grains themselves.

Figures 2-34 and 2-35 illustrate the Mallory E material, while Figures 2-36 and 2-37 show the H tungsten. Again, some contamination is present in these photographs. Both materials are uniform with pores as large as 5 microns. As with most Mallory materials, the surface of the particles is fairly smooth and regular, whether the samples were heated in testing or not. The G material is similar to the Wah Chang and Sylvania materials.

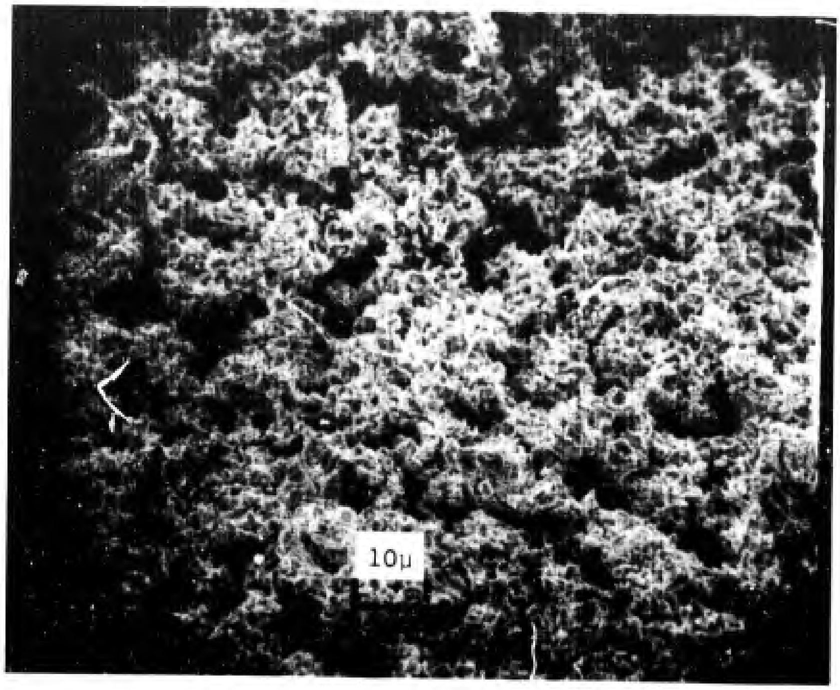

Figure 2-26. Mallory A, 1000X

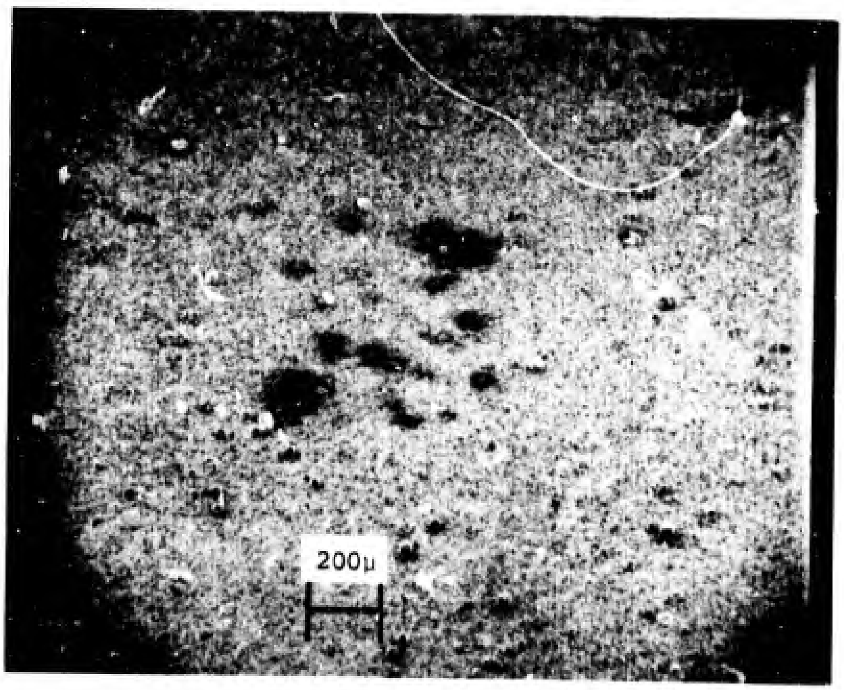

Figure 2-27. Mallory C, 50X

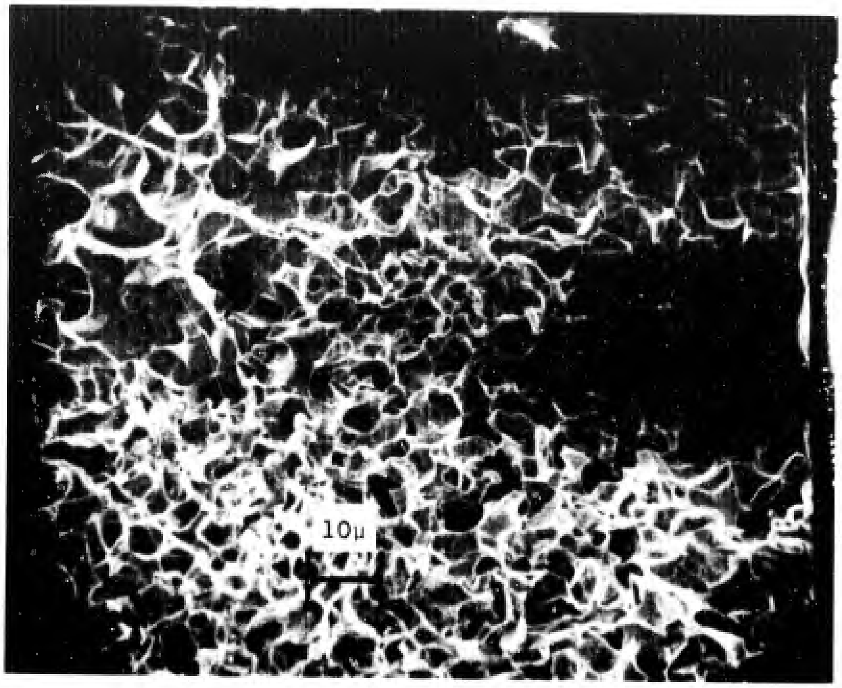

Figure 2-28. Mallory C, 1000X

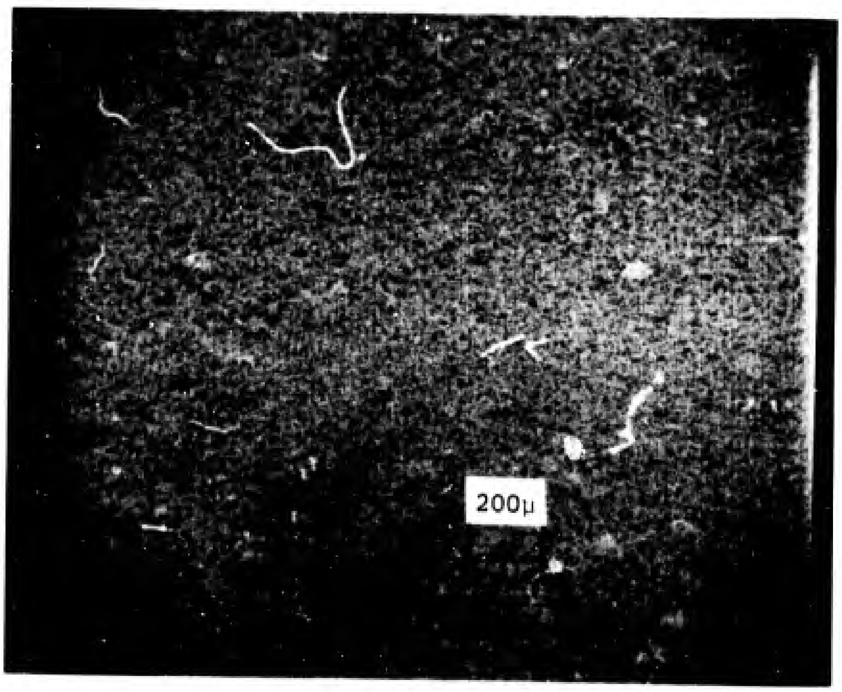

Figure 2-29. Untested Mallory D, 1.5 Micron Vapor-Deposited Tungsten on Surface, 50X

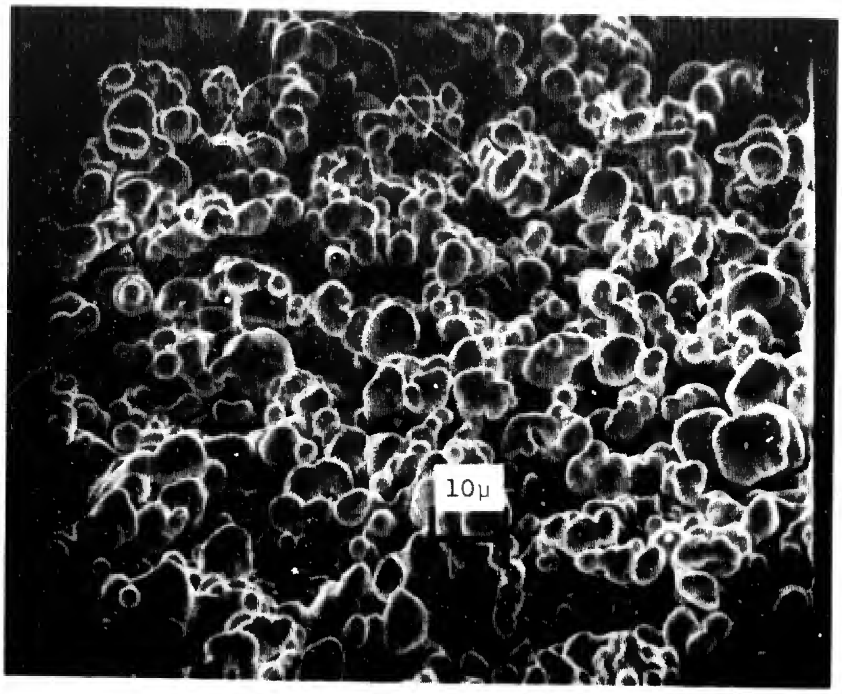

Figure 2-30. Untested Mallory D, 1.5 Micron Vapor-Deposited Tungsten on Surface, 1000X

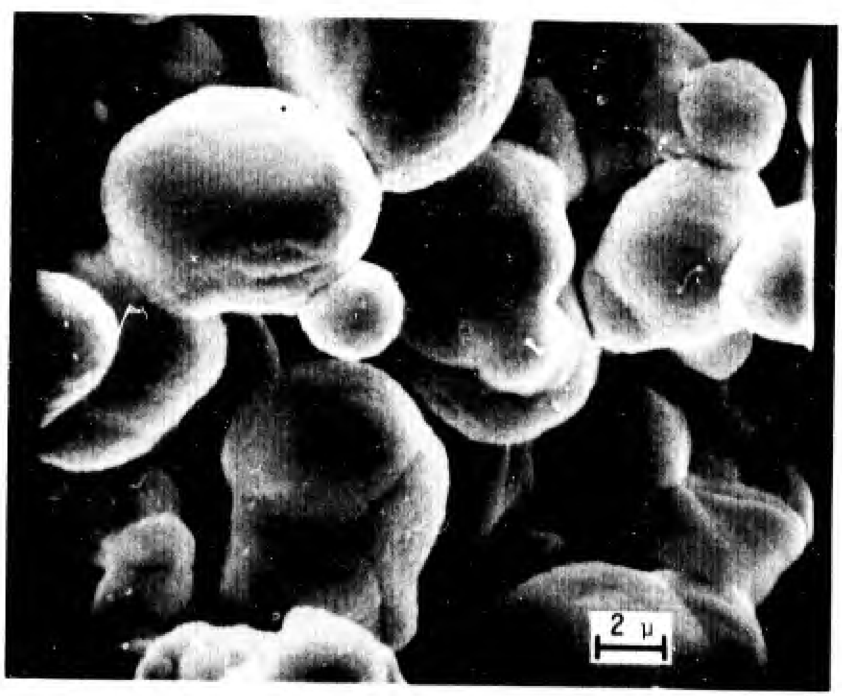

Figure 2-31. Untested Mallory D, 1.5 Micron Vapor-Deposited Tungsten on Surface, 5000X

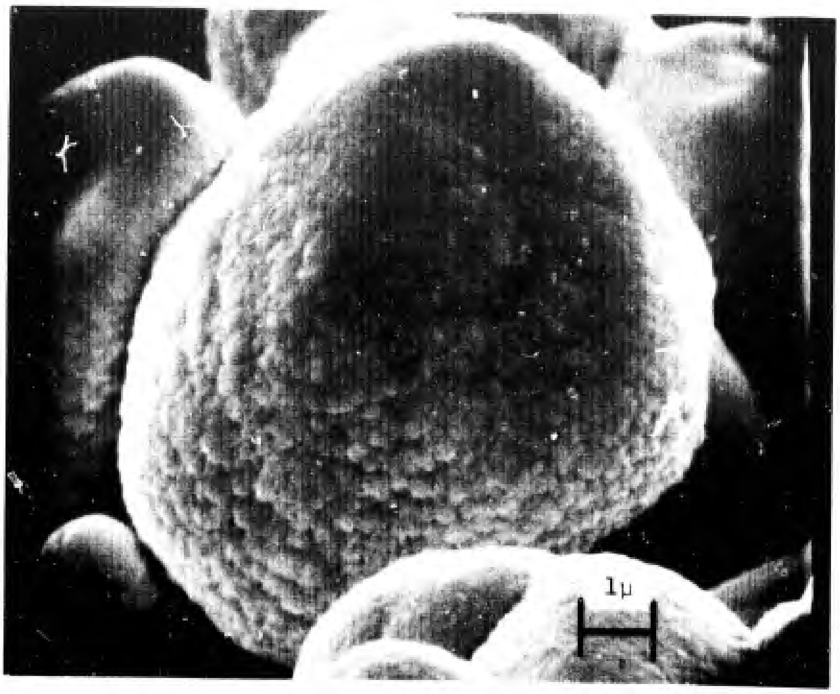

Figure 2-32. Untested Mallory D, 1.5 Micron
Vapor-Deposited Tungsten on
Surface 5000X

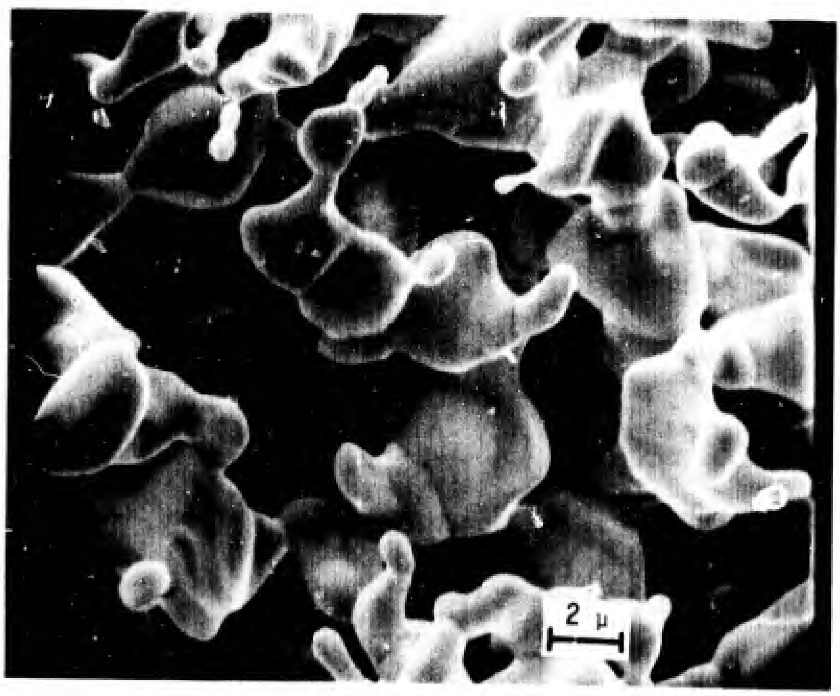

Figure 2-33. Untested Mallory D, 5000X

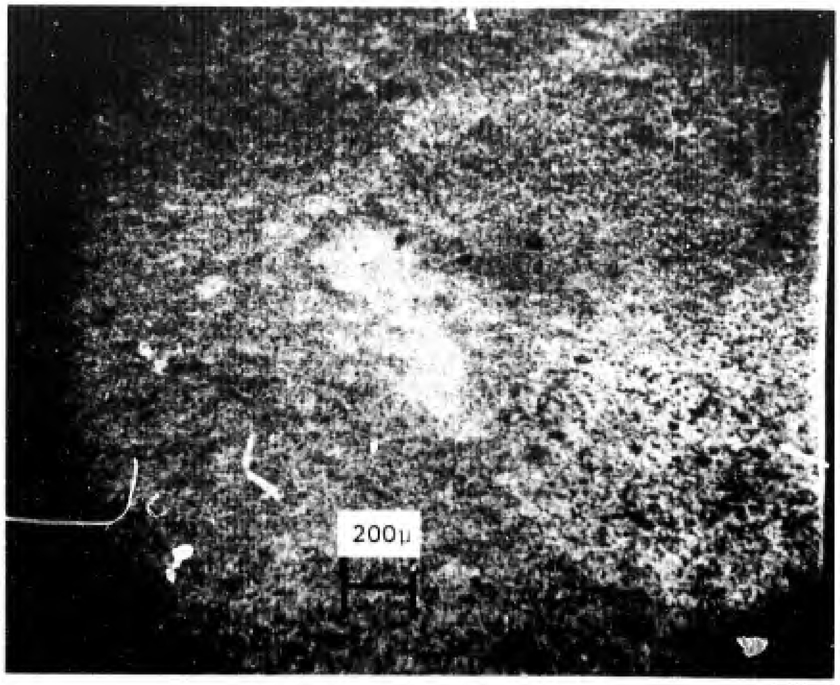

Figure 2-34. Untested Mallory E, 50X

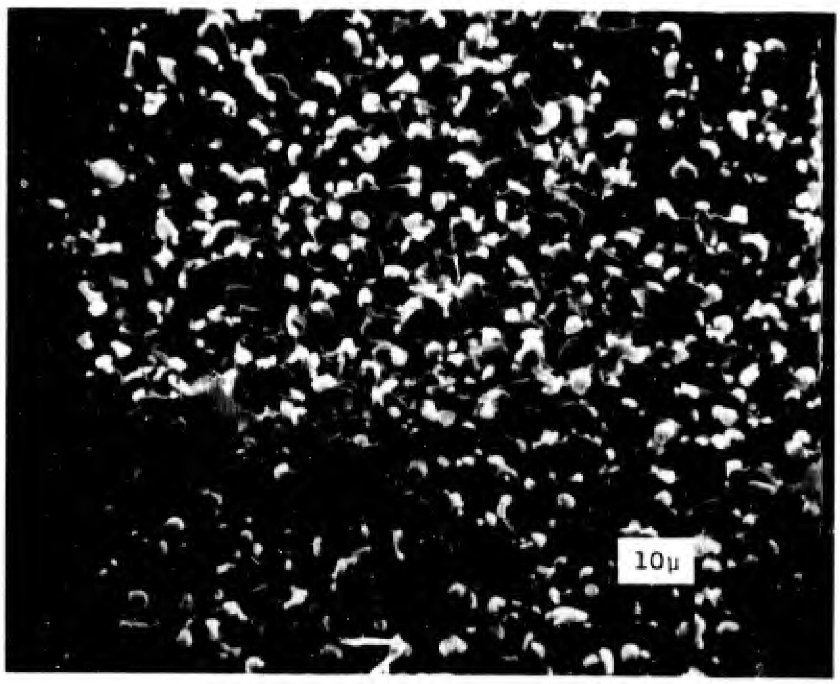

Figure 2-35. Untested Mallory E, 1000X –
Some Surface Contamination

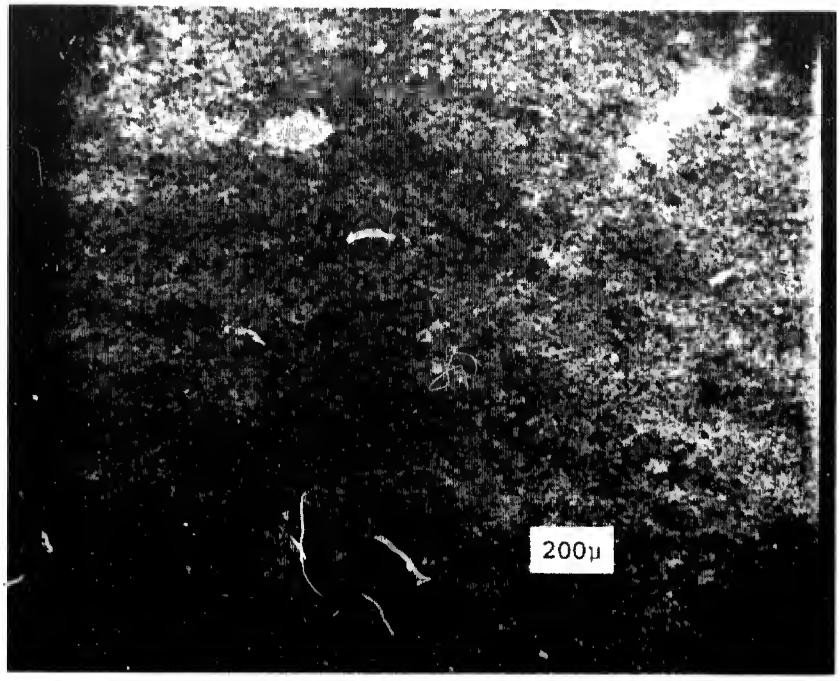

Figure 2-36. Untested Mallory H, 50X

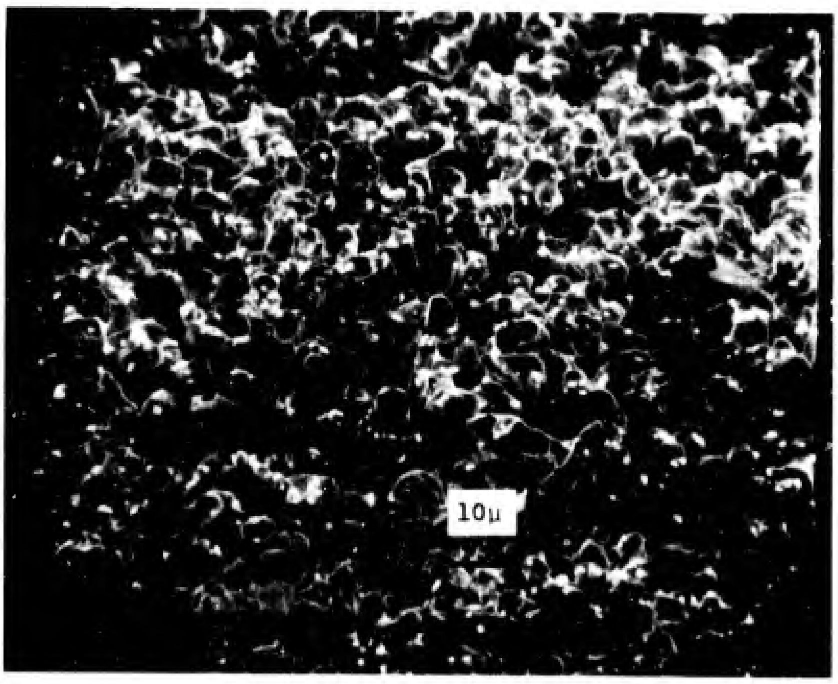

Figure 2-37. Untested Mallory H, 1000X

3. TEST RESULTS

3.1 Flow Characteristics Tests

The local mass flow transpiring through a porous matrix is defined by the temperature and pressure gradient across the matrix as well as the flow characteristics of the matrix itself. While the pressure and temperature gradients are functions of the flight environment, internal heat transfer coefficient, coolant thermophysical properties, and inlet pressure, the matrix permeability (Γ) and inertial resistance coefficient (β) are properties of the porous matrix alone. Both Γ and β must be determined experimentally for a specific material and, once known, define the flow characteristics of the material. Since Γ and β are properties of the matrix the flow characteristics tests were performed using nitrogen over a pressure drop range of 100 to 800 psid at room temperature. A description of the test apparatus and test procedure and a discussion of the data reduction procedure is given in Appendix A. The flow characteristic test matrix is shown in Table 3-I.

TABLE 3-I

Flow Characteristics Test Conditions

Concept	Pressure Drop psig	Matrix Thickness inches	Sample
1	800 600 400 200	1/4	Porous tungsten
2	800 600 400 200	1/4	Porous tungsten augmented with blind holes
3	600	1/4	Tungsten copper with one discrete hole
4	600	1/4	Tungsten copper with several discrete holes
5	800 600 400 200	1/4	Porous tungsten with flow control by vapor deposition

The test results are presented in Tables 3-II through 3-V referenced to the appropriate figures. Table 3-II summarizes the flow characteristic results for the unaltered porous tungsten materials. Values of β and Γ shown in all the tables result from a least squares, straight line curve fit to the cold flow data obtained on each specimen. These data, consisting of mass flow rate, gas temperature, and pressure drop across the porous tungsten specimen, are combined to form the parameters $(P^2-P_o^2)/2\mu\dot{m}ZRTX$ and $\dot{m}/\mu$. When this first parameter is plotted as the ordinate and the second as the abscissa, the reciprocal of permeability is the intercept of a straight line fitted to the data and the resistance coefficient is the slope of the line. Table 3-II indicates that the high volume density materials manufactured by Sylvania and Wah Chang have low numerical values of permeability and high values of inertial resistance coefficient. This trend indicates that a high pressure drop is required to force a given amount of flow through these materials, whereas a higher value of permeability and lower resistance coefficient indicates that a small pressure drop is required to force the flow through the porous matrix. The Mallory material tested had the widest range of flow characteristics, since the volume percentage of tungsten in the original tungsten copper ranged from 50 to 75 percent. Two groups of the Astro Met material were tested, the 60 percent by volume tungsten (307-60) group and the 40 percent by volume tungsten (307-40) group. The 307-60 material consisted of two batches, each batch representing a different manufacturing process. The 307-60 batch No. 1 material and the 307-40 material substantially have the same resistance to flow, although the 307-60 batch No. 1 specimens exhibited slightly lower average permeabilities and higher resistance coefficients than did the 307-40 specimens. The flow characteristics of double specimens that were selected from each group were also measured and are tabulated in Table 3-II; as expected little change in β or Γ resulted. The flow characteristics of the Astro Met 307-60 batch No. 2 material are vastly different from the batch No. 1 material. Although this shows Astro Met's capability to vary flow characteristics within the same material group by changing the manufacturing process, the data reproducibility from batch to batch has not been verified in this program.

Figures 3-1 through 3-5 show some of the data from which the parameters in Table 3-II have been taken. Figure 3-1, for example, shows the differences in permeability and resistance coefficient of two samples taken from different ends of an 80 percent Sylvania tungsten-copper stock. This difference indicates that further work is required to develop material acceptance standards for flight hardware use.

A summary of the flow characteristic testing on the porous tungsten materials augmented with blind holes is shown in Table 3-III and 3-IV. The Wah Chang 70 percent material was used as the base material from which the effect of the number of blind holes could be determined; flow characteristics data are shown in Table 3-III and Figure 3-6 respectively. The effect on flow characteristics of the depth of the blind holes is tabulated in Table 3-III and shown in Figure 3-7. Wah Chang 80 percent material was used as the base material from which the effect of depth was obtained. The effects of blind holes on flow rate through a porous medium can best be seen however on a curve where mass flow is shown as a function of pressure drop across the

TABLE 3-II

Flow Characteristics of Porous Tungsten Materials (Concept 1)

Material Manufacturer	Specimen Identification	Percent Tungsten By Volume	Permeability (ft^2)	Resistance Coefficient (1/ft)	Reference Figure Number
Wah Chang		80	1.37×10^{-13}	1.93×10^{8}	
Sylvania	End 1	80	1.26×10^{-13}	0.871×10^{8}	3-1
Sylvania	End 2	80	0.89×10^{-13}	3.14×10^{8}	3-1
Wah Chang	End 1	70	3.27×10^{-13}	3.02×10^{7}	
Wah Chang	End 2	70	0.61×10^{-13}	9.4×10^{7}	
Mallory	A	50	0.36×10^{-11}	0.21×10^{6}	3-2
Mallory	B	50	0.14×10^{-11}	0.52×10^{6}	3-2
Mallory	C	58	0.19×10^{-11}	1.04×10^{6}	3-2
Mallory	D	58	0.65×10^{-12}	1.49×10^{6}	3-2
Mallory	E	65	0.24×10^{-12}	0.47×10^{6}	3-2
Mallory	F	65	0.25×10^{-12}	0.13×10^{6}	3-2
Mallory	H	75	0.69×10^{-13}	0.84×10^{8}	3-2
Astro Met	307-60(1) Batch 2	60	0.17×10^{-13}	6.28×10^{9}	3-3
Astro Met	307-60(3) Batch 2	60	0.63×10^{-13}	1.33×10^{9}	3-3
Astro Met	307-60(4) Batch 2	60	0.48×10^{-13}	1.54×10^{9}	3-3
Astro Met	307-60(6) Batch 2	60	0.30×10^{-13}	1.42×10^{9}	3-3
Astro Met	307-60(7) Batch 2	60	0.32×10^{-13}	0.69×10^{9}	3-3
Astro Met	307-60(8) Batch 2	60	0.26×10^{-13}	3.23×10^{9}	3-4
Astro Met	307-60(1) Batch 1	60	0.458×10^{-10}	0.62×10^{6}	3-4
Astro Met	307-60(2) Batch 1	60	0.79×10^{-10}	0.109×10^{7}	3-4
Astro Met	307-60(3) Batch 1	60	0.111×10^{-9}	0.368×10^{6}	3-4
Astro Met	307-60(4) Batch 1	60	0.165×10^{-10}	0.299×10^{6}	3-4
Astro Met	307-60(5) Batch 1	60	0.364×10^{-10}	0.432×10^{6}	3-4
Astro Met	307-60(6) Batch 1	60	0.713×10^{-11}	0.195×10^{6}	3-4
Astro Met	307-60(7) Batch 1	60	0.955×10^{-11}	0.428×10^{6}	3-5
Astro Met	307-40(1)	40	0.158×10^{-10}	0.507×10^{6}	3-5
Astro Met	307-40(1)	40	0.144×10^{-10}	0.224×10^{6}	3-5
Astro Met	307-40(2)	40	0.133×10^{-10}	0.195×10^{6}	3-5
Astro Met	307-40(3)	40	0.112×10^{-10}	0.299×10^{6}	3-5
Astro Met	307-40(4)	40	0.115×10^{-10}	0.365×10^{6}	3-5
Astro Met	307-40(5)	40	0.789×10^{-11}	0.242×10^{6}	3-5
Astro Met	307-40(5), 307-40(1)*	40	0.232×10^{-10}	0.139×10^{6}	3-5
Astro Met	307-40(6), 307-40(2)*	40	0.99×10^{-11}	0.184×10^{6}	3-5
Astro Met	307-60(1), 307-60(5) Batch 1*	60	0.288×10^{-10}	0.425×10^{6}	3-4
Astro Met	307-60(2), 307-60(6) Batch 1*	60	0.386×10^{-10}	0.534×10^{6}	3-4

*Double Specimen

TABLE 3-III

Flow Characteristics of Porous Tungsten Materials Augmented with Blind Holes (Concept 2)

Material Manufacturer	Percent Tungsten By Volume	Hole Configuration	Permeability (ft^2)	Resistance Coefficient (1/ft)	Reference Figure Number
Wah Chang	70	1 blind hole 0.020 dia x 0.15 inch deep	2.24×10^{-13}	2.84×10^{6}	3-6
Wah Chang	70	5 blind holes 0.020 dia x 0.15 inch deep	1.92×10^{-13}	2.97×10^{6}	3-6
Wah Chang	70	9 blind holes 0.020 dia x 0.15 inch deep	1.61×10^{-13}	1.86×10^{6}	3-6
Wah Chang	70	17 blind holes 0.020 dia x 0.15 inch deep	1.48×10^{-13}	2.45×10^{6}	3-6
Wah Chang	80	25 blind holes 0.020 dia x 0.030 inch deep	1.22×10^{-13}	2.96×10^{7}	3-6
Wah Chang	80	25 blind holes 0.020 dia x 0.060 inch deep	1.47×10^{-13}	1.31×10^{7}	3-7
Wah Chang	80	25 blind holes 0.020 dia x 0.090 inch deep	1.83×10^{-13}	0.95×10^{7}	3-7

TABLE 3-IV

Effect of Flow Direction on the Flow Characteristics of Porous Tungsten Materials Augmented with Blind Holes (Concept 2) (Using Wah Chang 80 Percent Tungsten with 25 Blind Holes)

Hole Depth (inch)	Flow Direction	Permeability	Resistance Coefficient	Reference Figure Number
0.060	Blind holes downstream	1.47×10^{-13}	1.31×10^{7}	3-8
0.060	Blind holes upstream	1.6×10^{-13}	2.03×10^{7}	3-8
0.090	Blind holes downstream	1.83×10^{-13}	0.95×10^{7}	3-8
0.090	Blind holes upstream	2.82×10^{-13}	1.47×10^{7}	3-8

TABLE 3-V

Flow Characteristics of Tungsten with Discrete Holes (Concepts 3 and 4)

Material Manufacturer	Hole Configuration	Flow Coefficient	Reynolds No.
Wah Chang	5 through holes 0.025 inch dia	0.65	5×10^{3}
Wah Chang	5 through holes 0.025 inch dia	0.70	1.5×10^{4}
Wah Chang	5 through holes 0.030 inch dia	0.53	5×10^{3}
Wah Chang	5 through holes 0.030 inch dia	0.55	1.5×10^{4}
Wah Chang	1 through hole 0.030 inch dia	0.53	5×10^{3}
Wah Chang	1 through hole 0.030 inch dia	0.55	1.5×10^{4}

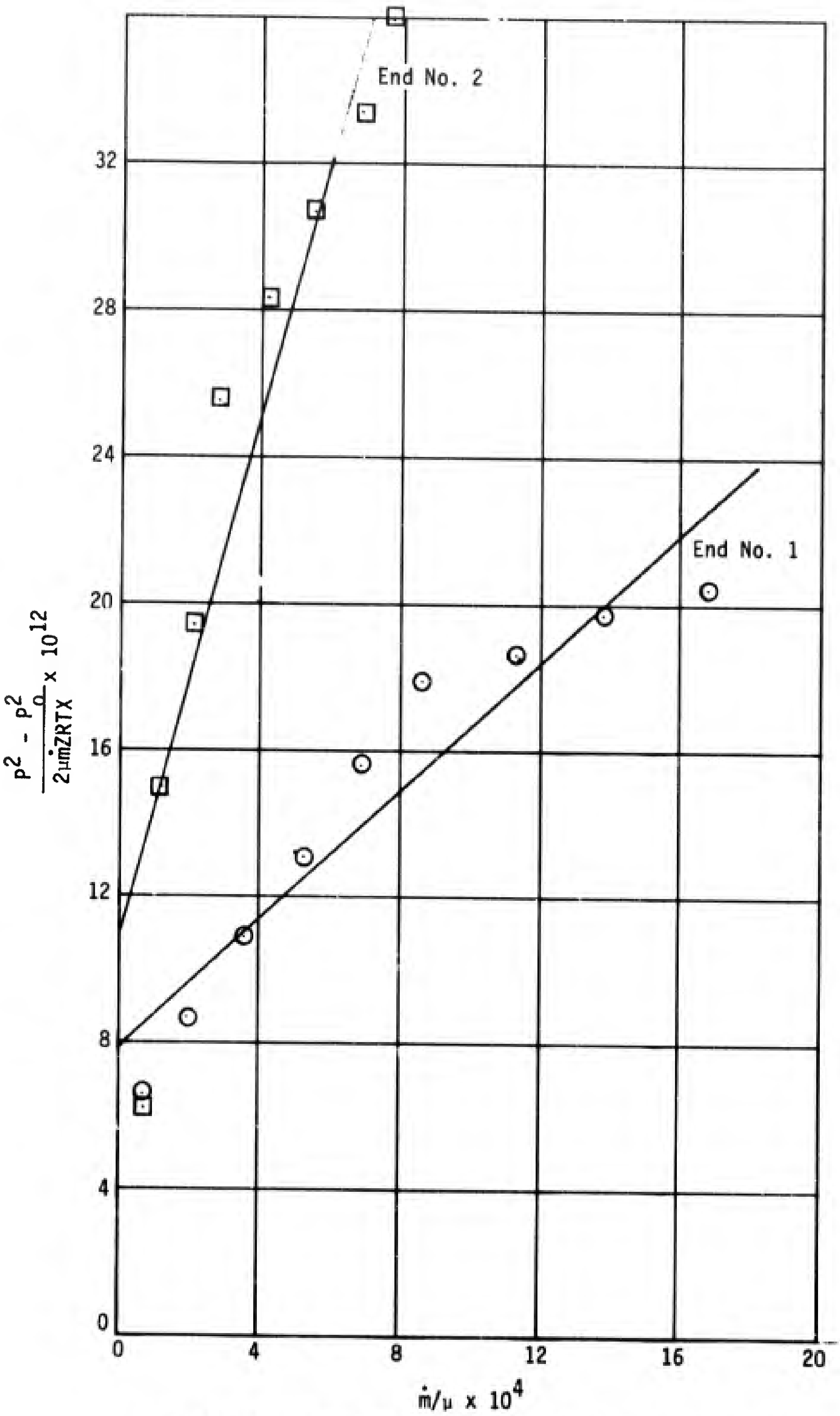

Figure 3-1. Flow Characteristics of Sylvania Tungsten

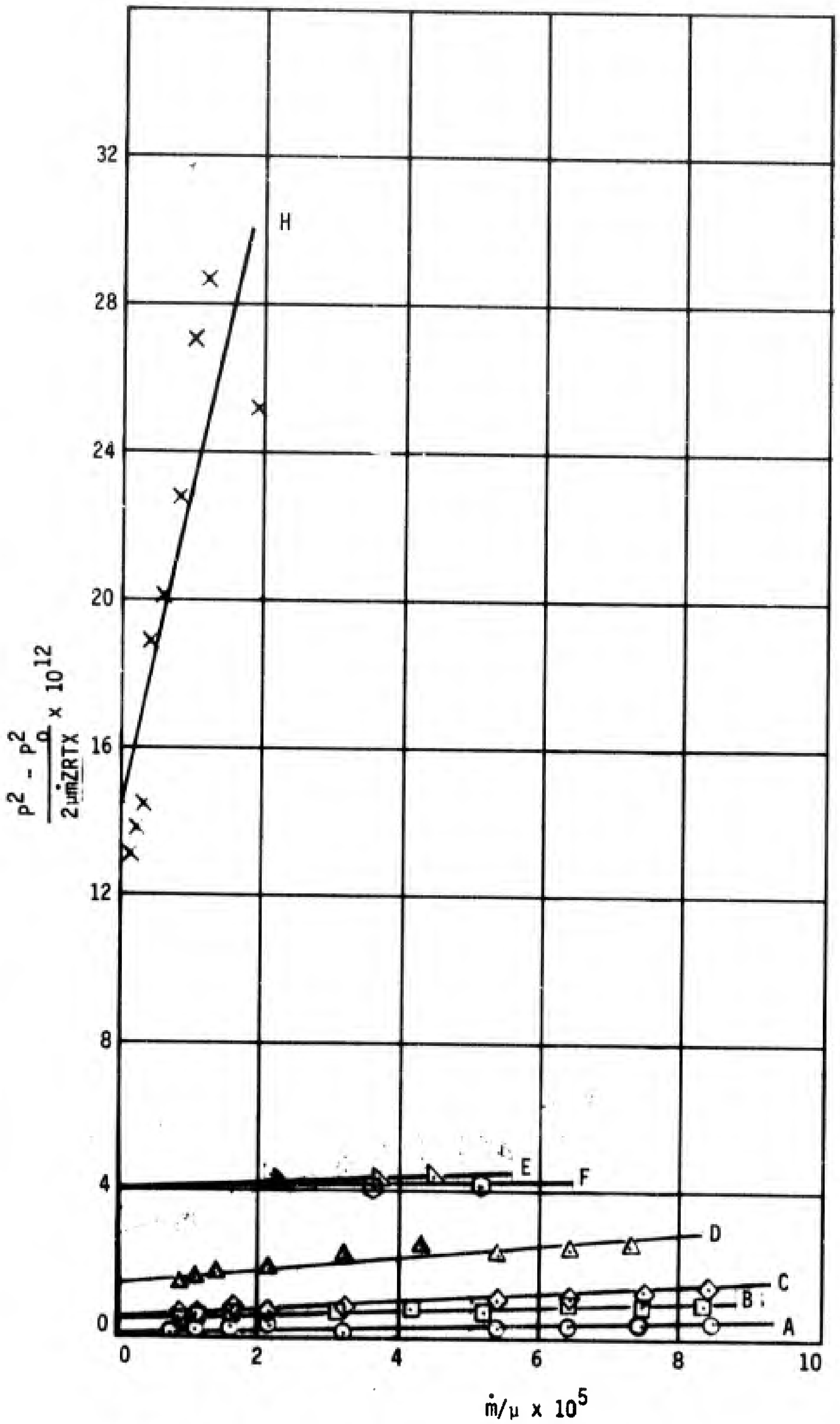

Figure 3-2. Flow Characteristics of Mallory Tungsten

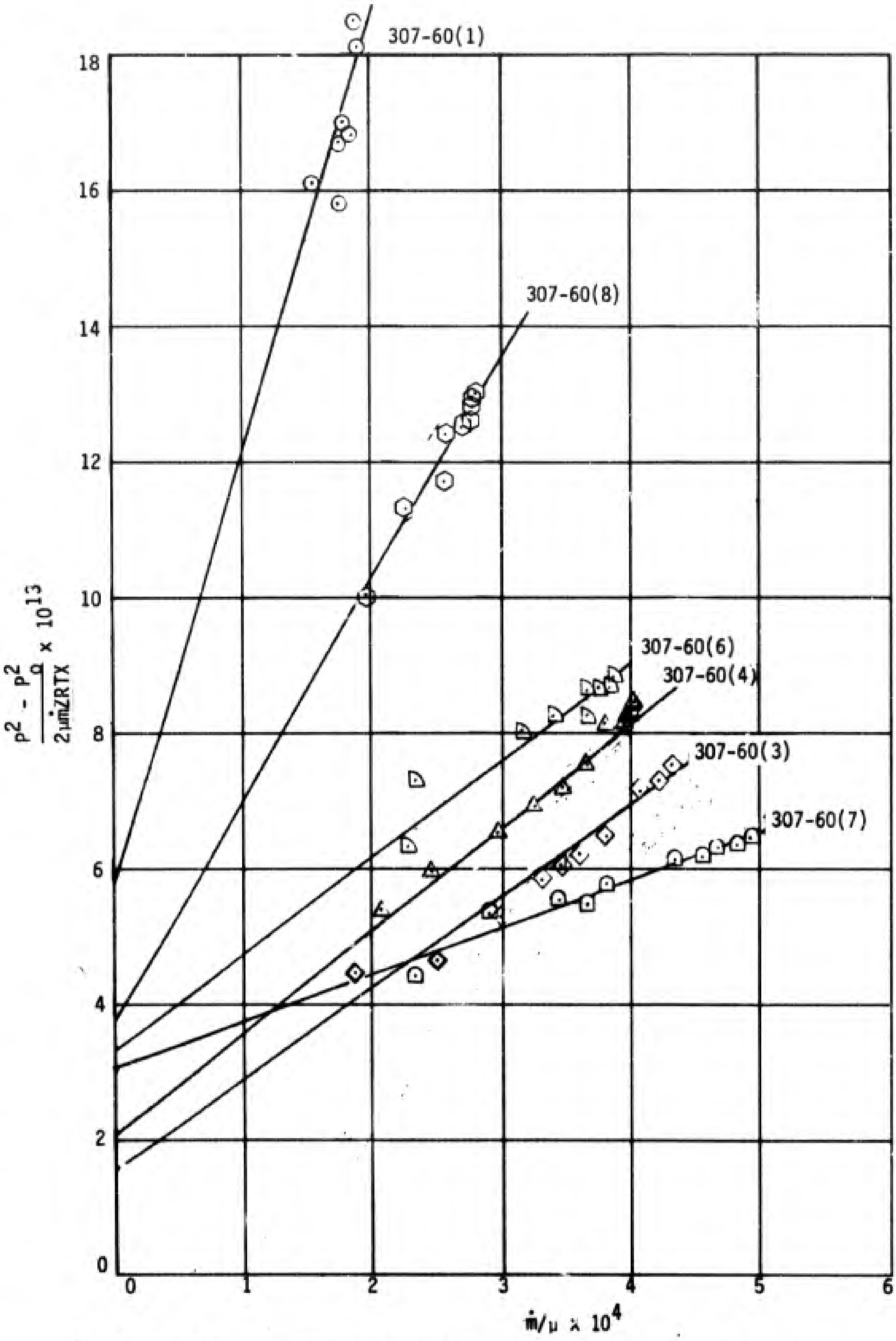

Figure 3-3. Flow Characteristics of Astro Met Tungsten 307-60

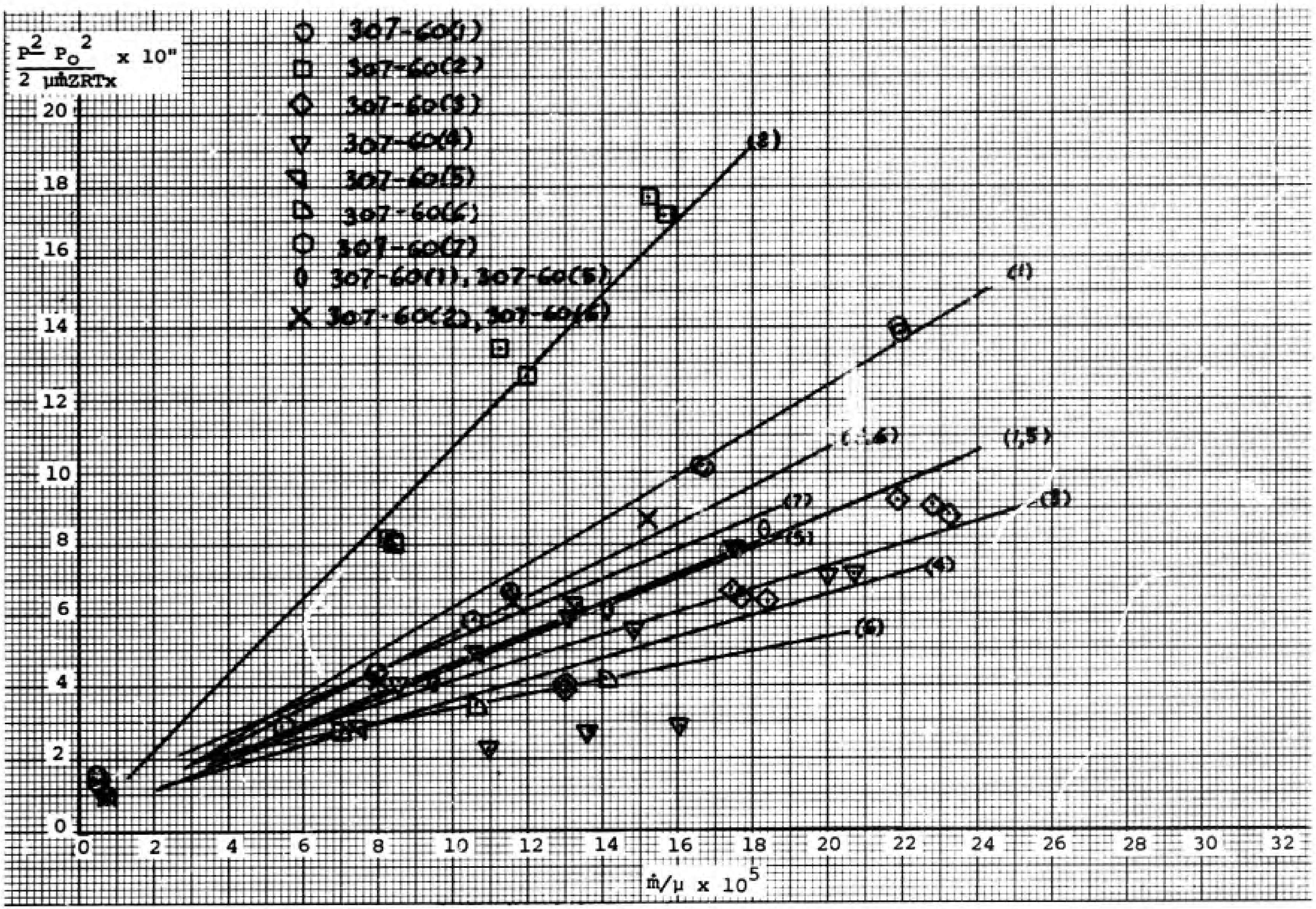

Figure 3-4. Flow Characteristics of Astro Met Tungsten 307-60

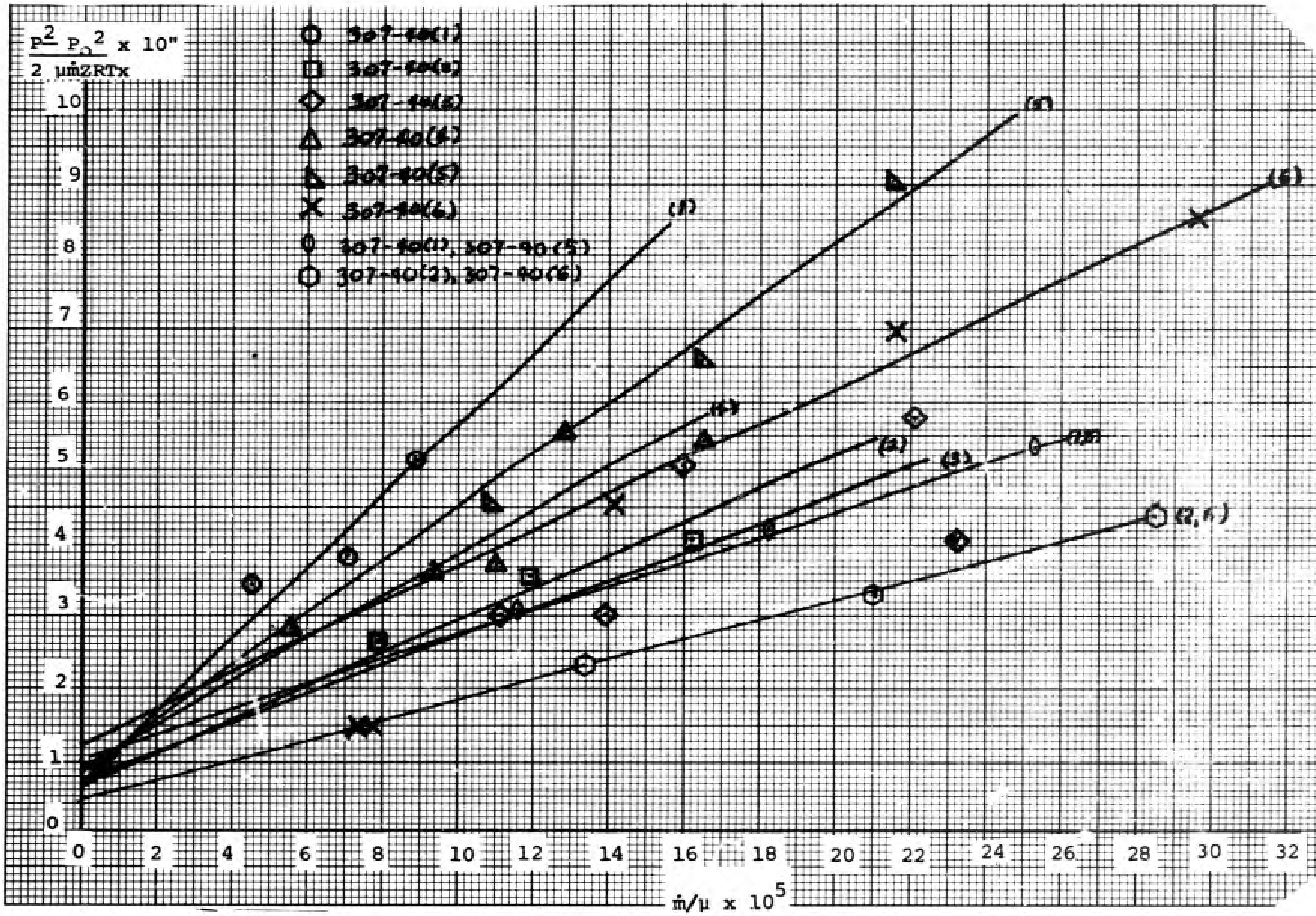

Figure 3-5. Flow Characteristics of Astro Met Tungsten 307-40

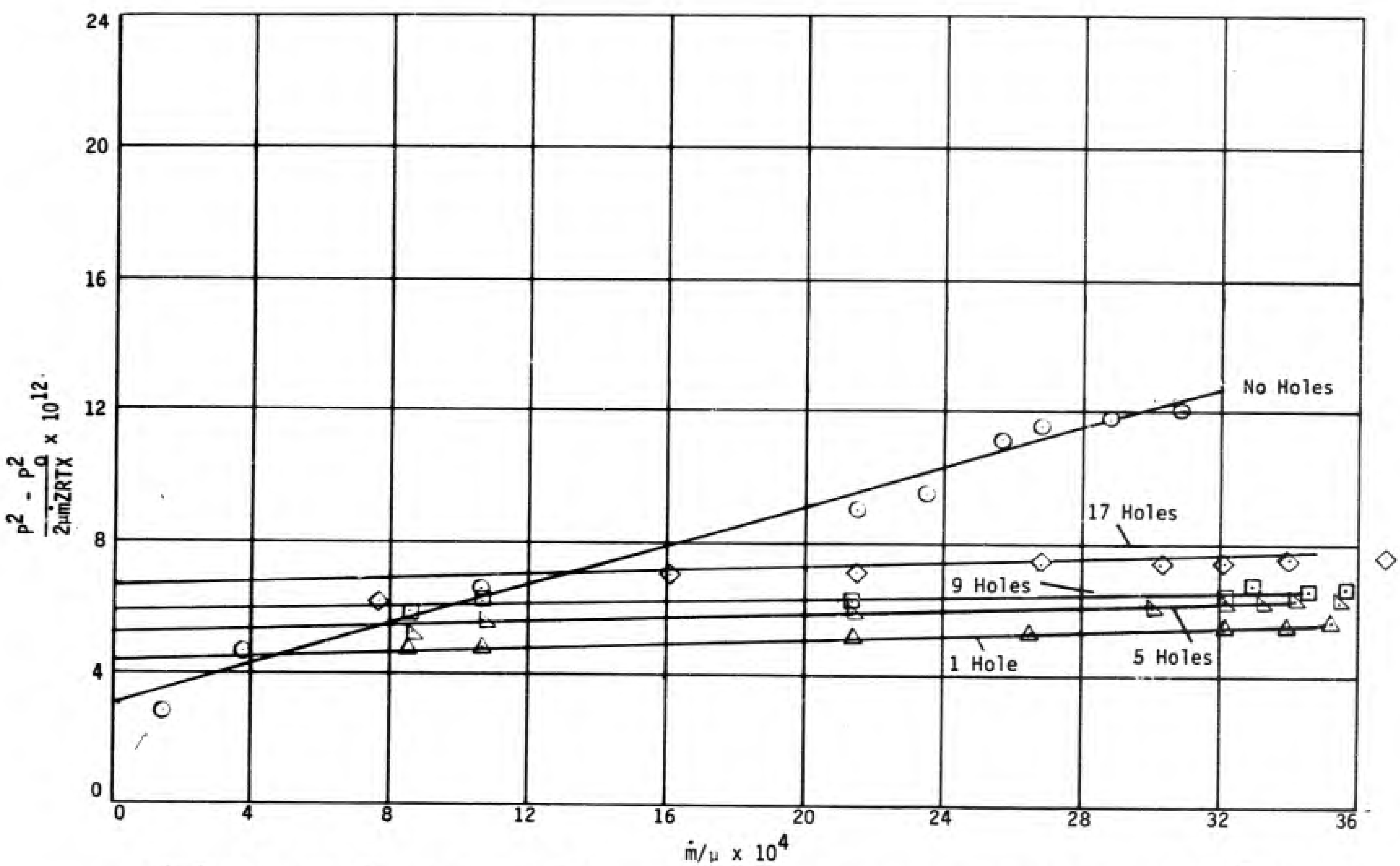

Figure 3-6. Flow Characteristics of 70 percent Wah Chang Tungsten Augmented with Blind Holes

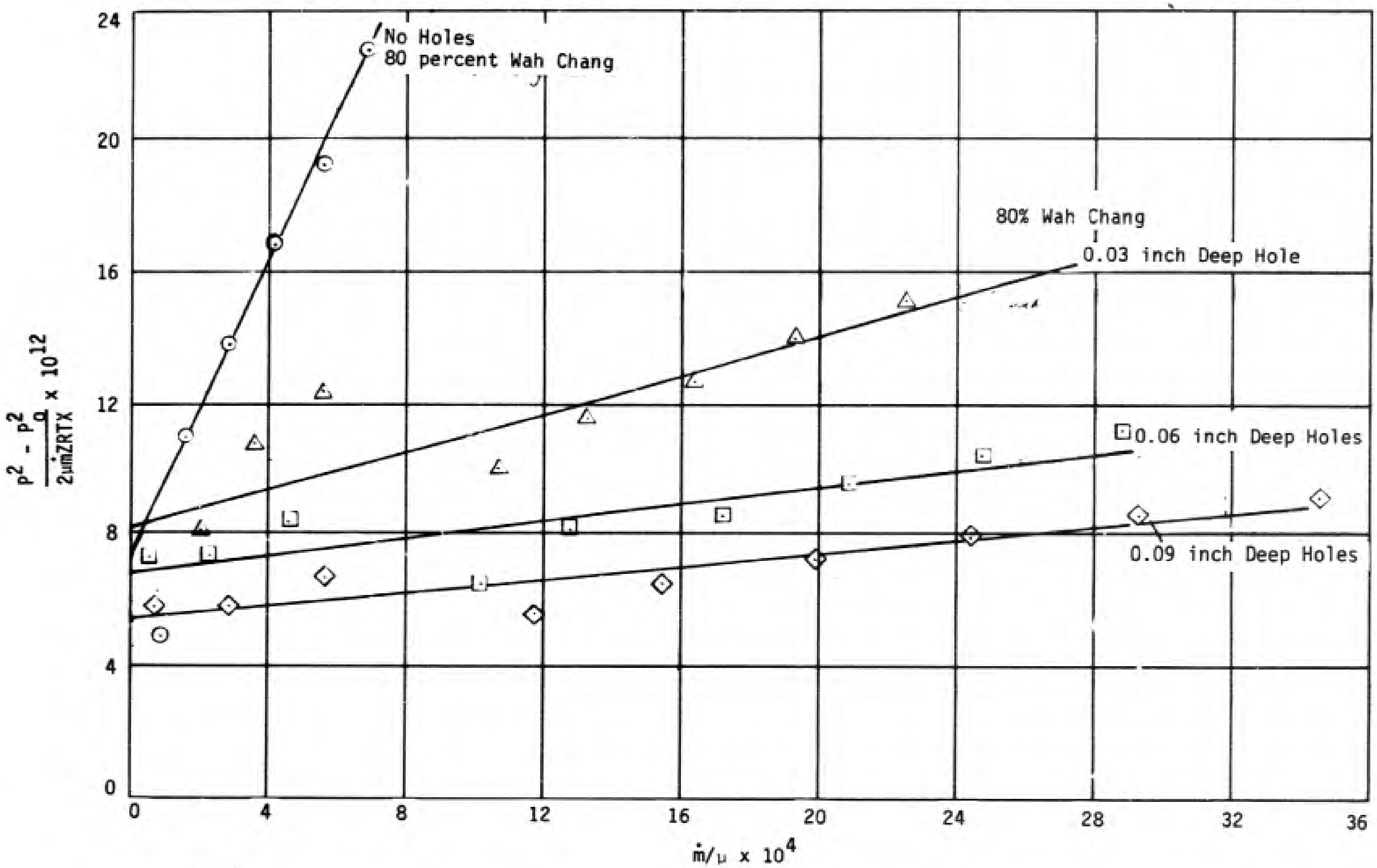

Figure 3-7. Flow Characteristics of 80 Percent Wah Chang Tungsten Augmented with Blind Holes

matrix. Figures 3-8 and 3-9 show this effect. Figure 3-8 shows the increase in mass flow as a function of hole depth. For example, at a ΔP = 600 psid, 0.09 inch holes can quadruple the flow rate in 80 percent tungsten. This technique can be very useful if a large amount of flow is required in a localized area because of very high heating such as the sonic point.

Figure 3-6 shows the effect of the number of blind holes on the flow characteristics of porous tungsten matricies. Flow properties of the matricies with blind holes are compared with an identical matrix without blind holes. Specimens with 1, 5, 9, and 17 holes, which were 0.02 inch diameter x 0.15 inch deep, were drilled in a 0.25 inch thick porous tungsten matrix. The specific values of permeability (the reciprocal of the intercept on the ordinate axis) and of inertial resistance coefficient (the slope of the curve) are tabulated in Tables 3-II and 3-III for each case.

The presence of blind holes has decreased the permeability by a maximum of 50 percent for the 17 blind hole case and has decreased the inertial resistance coefficient more than an order of magnitude for all cases. Since the slopes of the curves are almost the same, it can be expected that at the high mass flow rates of interest in this program, $\dot{m} > 0.5$ lb/ft^2-s, the mass flow-pressure drop relationship will show a very weak dependence on the number of blind holes in a matrix. The mass flow-pressure drop relationship shown in Figure 3-9 verifies this observation. It is apparent that the flow rate increase resulting from the addition of one blind hole is so large that additional blind holes do not appreciably enhance the flow any further. Although a detailed flow field analysis would be required to fully explain this phenomenon, it was determined that this analysis was not warranted at this time.

The difference in mass flow for a given pressure drop between downstream blind holes and upstream blind holes is shown in Figure 3-10. The flow characteristics for these cases are tabulated in Table 3-IV. There is a slight difference in the amount of flow passing through a specimen at a given pressure drop; blind holes placed on the upstream side are more effective. Because of geometrical limitations, upstream blind holes can only be easily placed on the stagnation point of a nose tip or on a stagnation line of an air vane leading edge.

With the data from Tables 3-III and 3-IV, the effect of hole depth on the inertial resistance coefficient is shown in Figure 3-11. From Figures 3-7 and 3-11, it can be concluded that blind hole depth has little effect on permeability but has a large effect on inertial resistance coefficient.

The characteristics of compressible fluids passing through pipes are well known and documented. The characterization of fluids passing through hot tungsten copper, with discrete hole diameters of interest for this study, are shown in Table 3-V and Figure 3-12. The flow, as expected, can be represented in terms of the flow function, $\dfrac{w\sqrt{TR}}{P_T A}$

where:

w = mass flow rate
T = temperature
R = gas constant
P_T = pressure
A = flow area

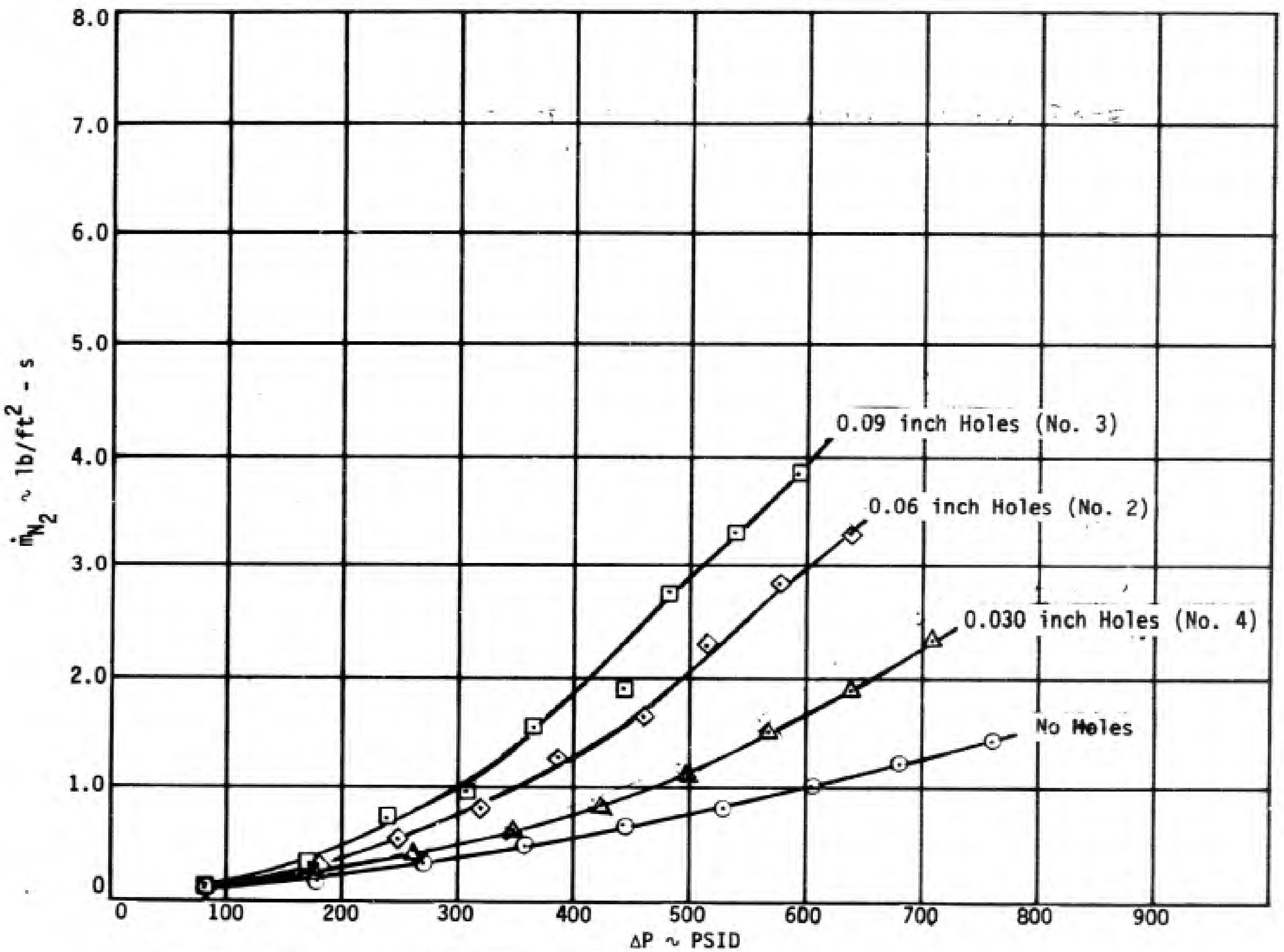

Figure 3-8. Effect of Blind Hole Depth on Flow Through 80 Percent Tungsten

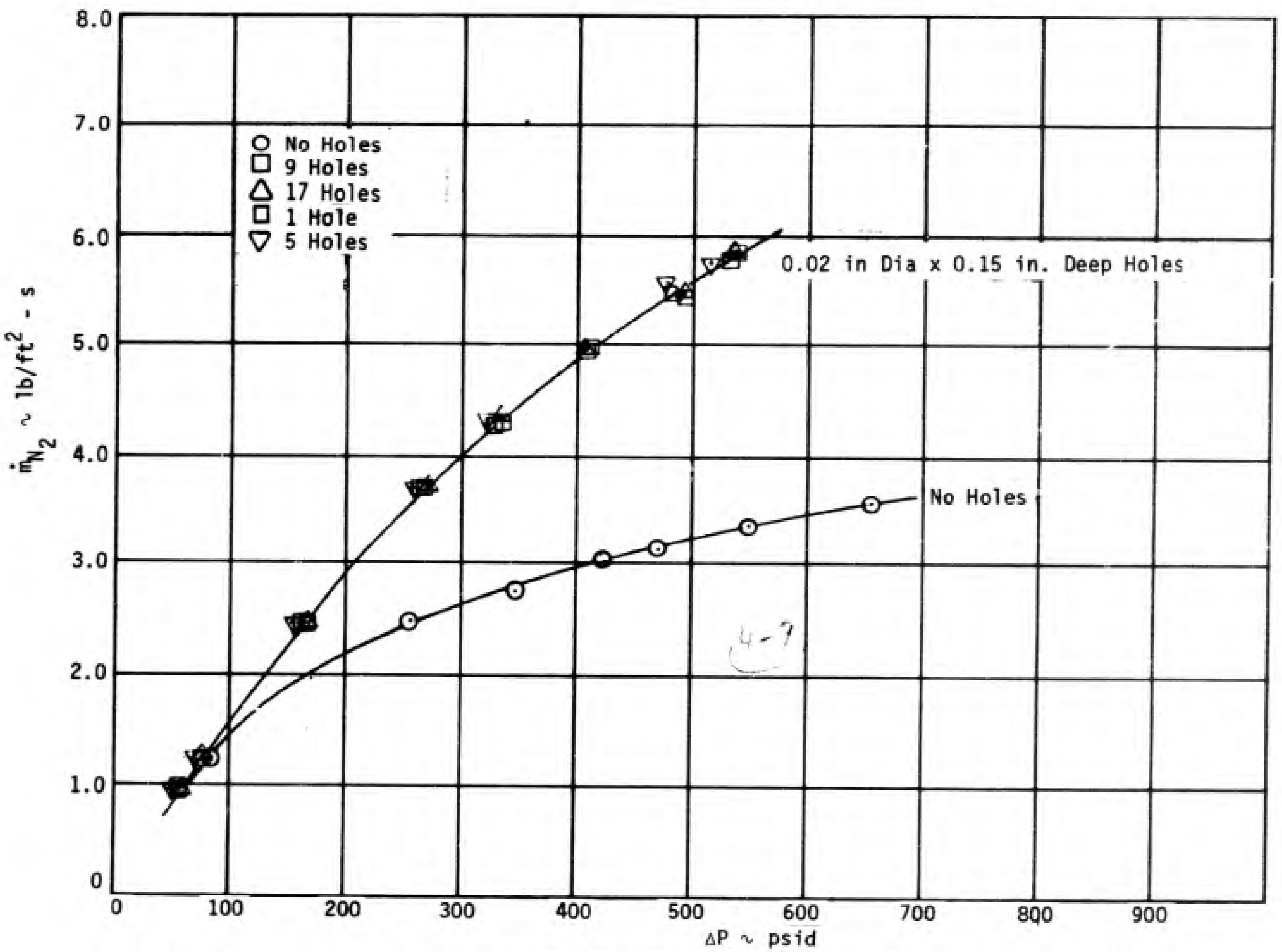

Figure 3-9. Effect of Blind Hole Number on Flow Through 70 Percent Tungsten

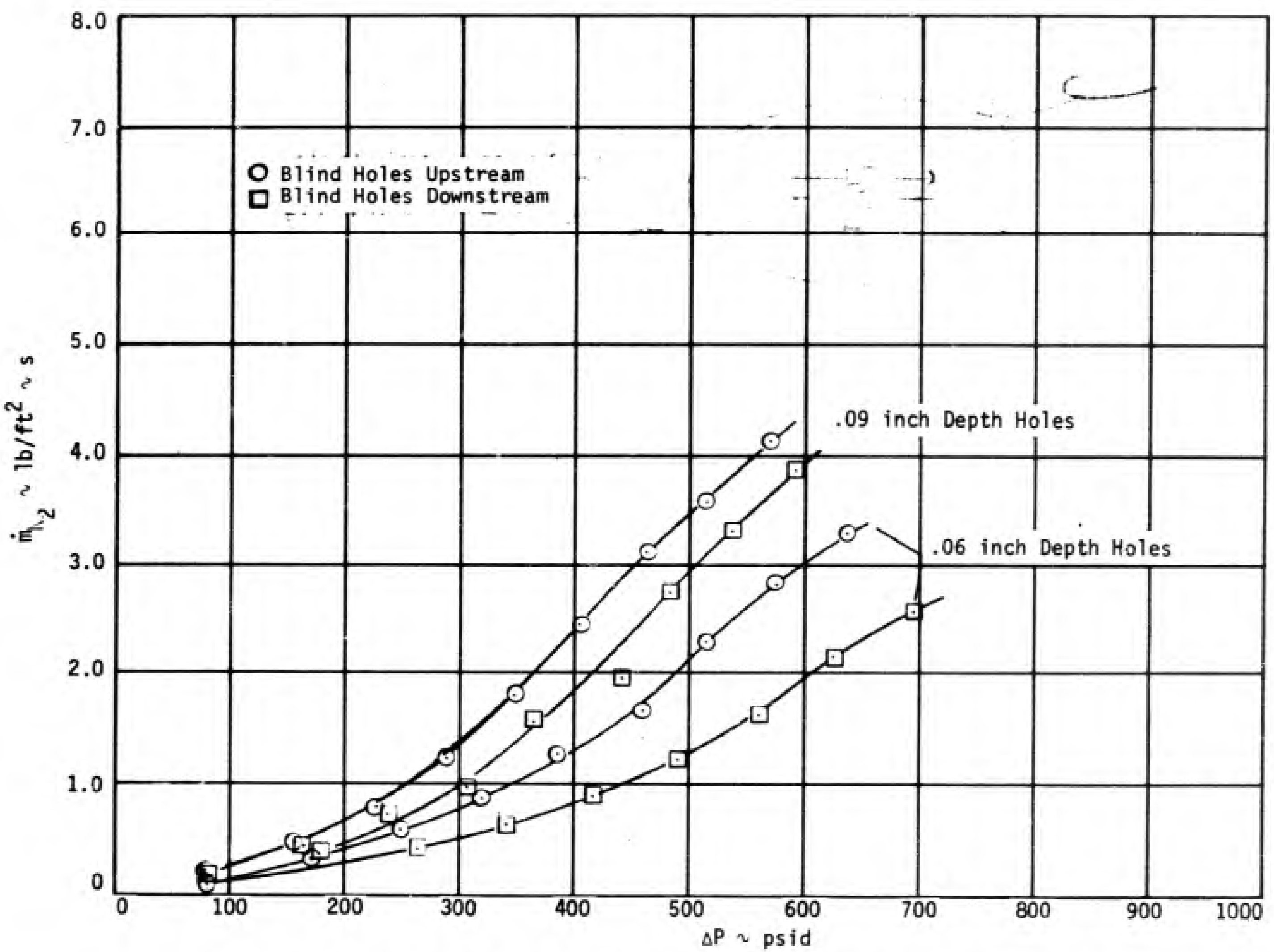

Figure 3-10. Effect of Upstream and Downstream Blind Holes Flow

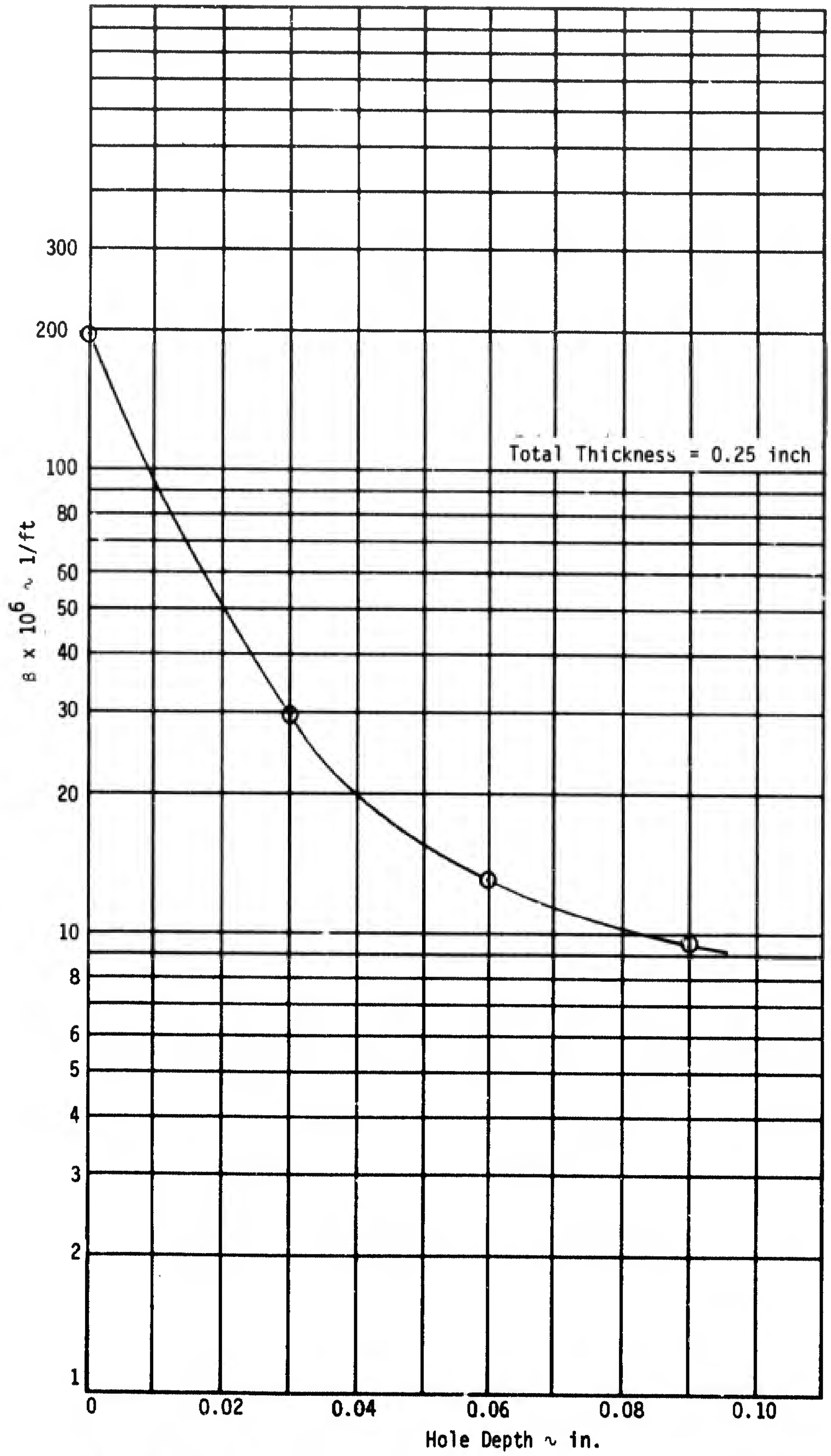

Figure 3-11. Effect of Hole Depth on 80 Percent Wah Chang Tungsten

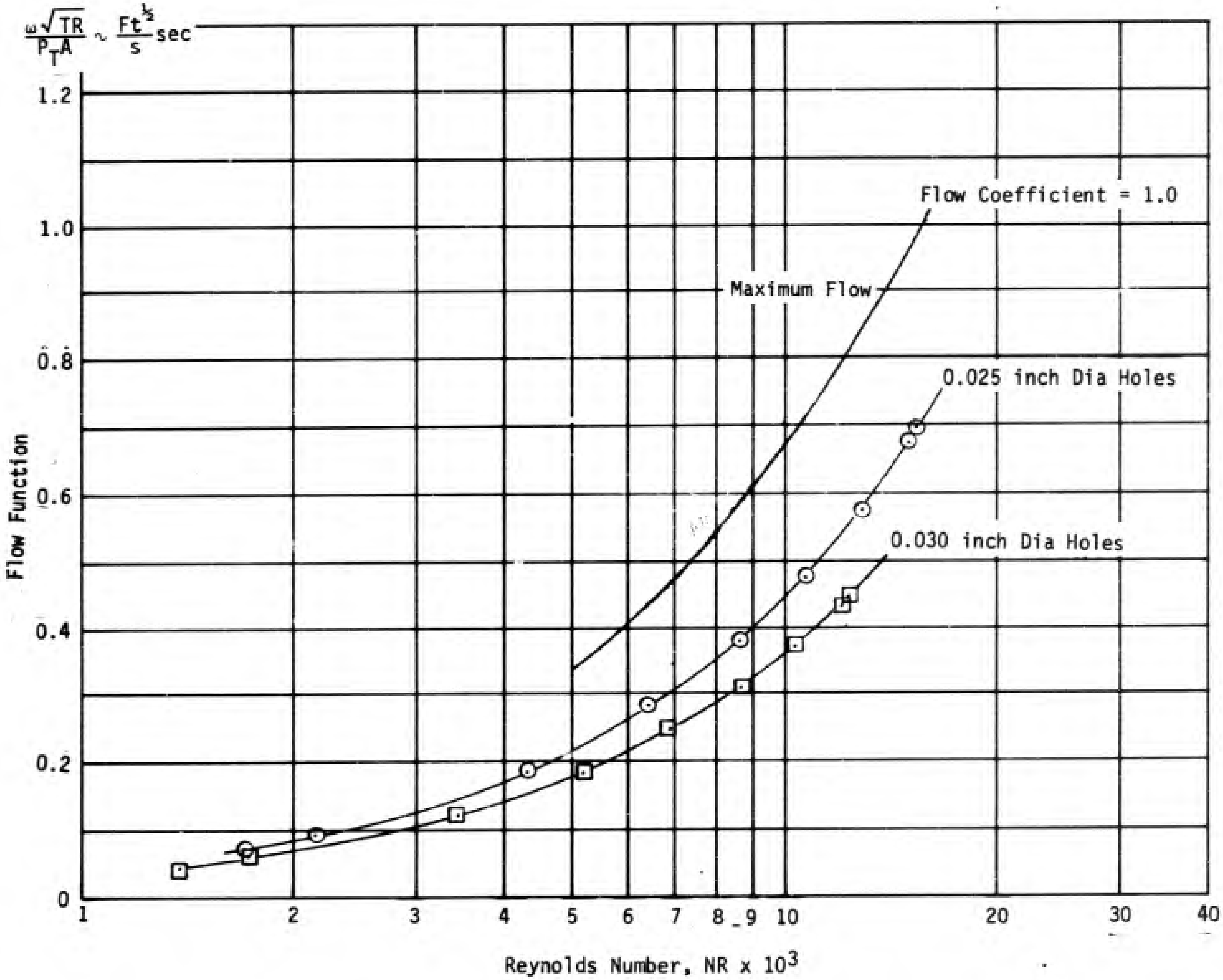

Figure 3-12. Flow Characteristics of Discrete Holes

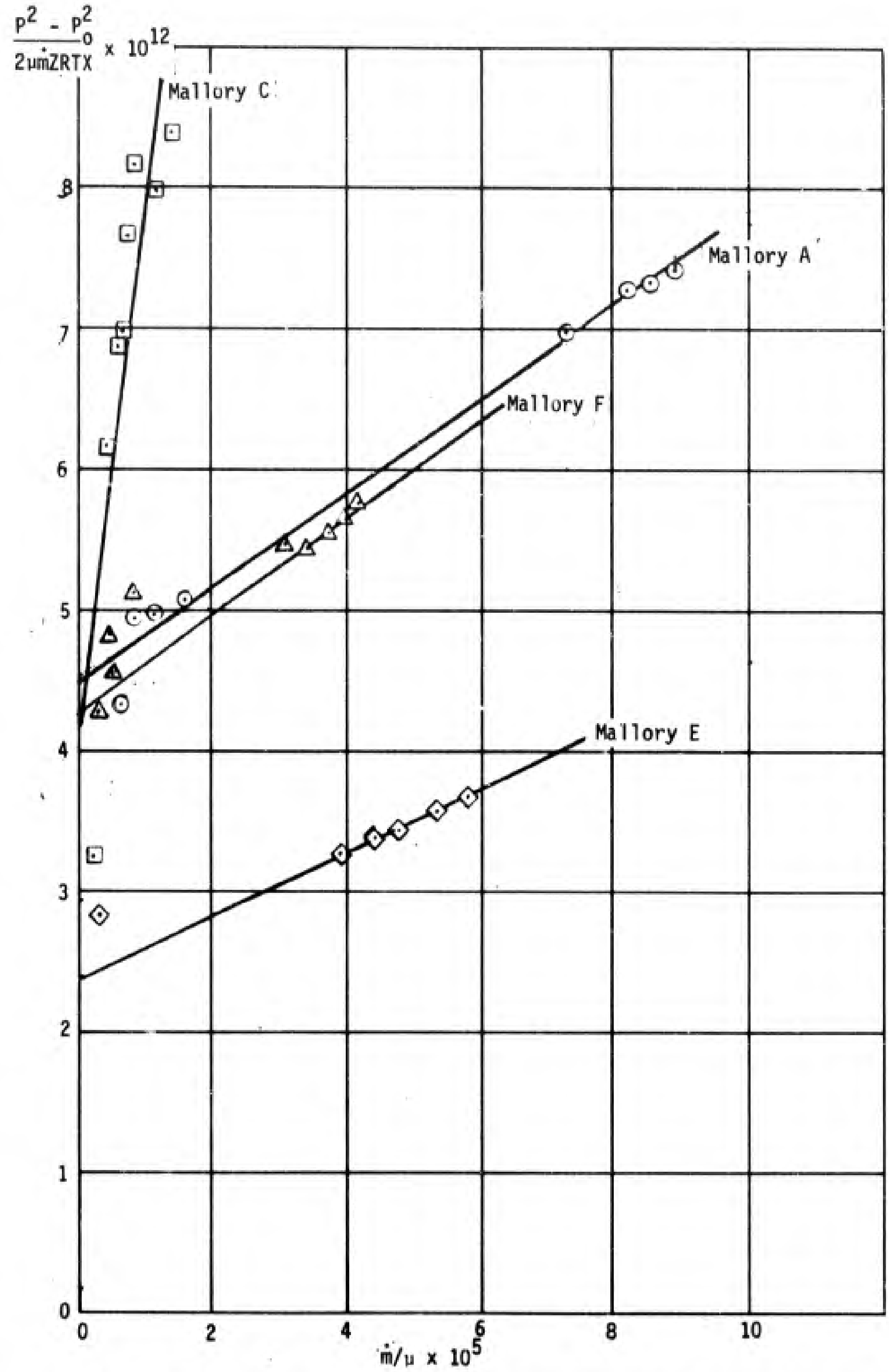

Figure 3-13. Flow Characteristics of Tungsten-Coated Mallory Tungsten

Flow coefficients have been derived for the 0.025 inch diameter discrete holes and the 0.030 inch diameter holes as a function of Reynolds Number and are reported in Table 3-V. The flow function of an ideal gas with a γ of 1.4 is also shown in Figure 3-12.

The data presented in Table 3-VI show the results of flow control by vapor deposition. The purpose of this concept is to reduce mass flow in a region in which it is not needed. For example, in a sidewall region of a nose tip or air vane leading edge, the pressure drop is very high because of the low sidewall local pressure, thereby creating the potential for a high sidewall mass flux. However, the heat rate is much less than that found in the stagnation or sonic regions and a high mass flow rate is not necessary. A decrease in permeability and increase of resistance coefficient can be achieved through vapor deposition which in effect partially closes the surface pores. The sputtering technique for vapor deposition is described in Chapter 2 and Appendix B. Both tungsten vapor and gold vapor were used in these experiment.

Although gold would not be an acceptable material for the flow control of a CONAP nose tip or air vane, it was employed for these cold flow experiments in order to determine the variation in flow with sputtering thickness for two different metals. A comparison of Figure 3-14 (tungsten) and Figure 3-15 (gold) at a thickness of 1 micron indicates little difference between the two.

TABLE 3-VI

Flow Characteristics of Porous Tungsten Materials with Flow Control By Vapor Deposition (Concept 5)

Material Manufacturer	Specimen Identification	Percent Tungsten By Volume	Vapor Deposition Material and Thickness	Permeability	Resistance Coefficient
Mallory	A	50	1 micron tungsten	0.22×10^{-11}	0.34×10^{6}
Mallory	C	58	2 micron tungsten	0.24×10^{-11}	3.62×10^{6}
Mallory	E	65	3 micron tungsten	0.42×10^{-12}	2.25×10^{6}
Mallory	F	65	5 micron tungsten	0.23×10^{-12}	3.45×10^{6}
Astro Met	307-60(6) Batch 1	60	0.5 micron gold	2.03×10^{-11}	3.85×10^{5}
Astro Met	307-60(6) Batch 1	60	1.0 micron gold	1.64×10^{-11}	5.55×10^{5}
Astro Met	307-60(6) Batch 1	60	1.5 micron gold	3.04×10^{-12}	2.89×10^{5}

Mallory A, C, E and F materials were used for tungsten vapor deposition and Astro Met 307-60 batch No. 1 material was used for gold vapor deposition. Flow characteristic data is tabulated in Table 3-VI. Figure 3-13 shows the flow characteristics of the Mallory materials after vapor deposition. A comparison of mass flow rates through porous tungsten materials with and without vapor deposition is shown in Figures 3-14 and 3-15. Figure 3-14 shows the effect of tungsten vapor surface deposits on the Mallory materials. Figure 3-15 shows the effect of progressive 0.5 micron deposits on one Astro Met 370-60 batch No. 1 specimen. For example at 200 psid pressure drop, a 1.5 micron vapor deposition can reduce the flow rate by roughly 40 percent. Figures 3-16 and 3-17 show how permeability and resistance coefficient are affected by the thickness of gold vapor deposition. Note that the ''thickness'' is measured by the thickness of vapor deposited on a flat, smooth tare specimen placed next to the work piece.

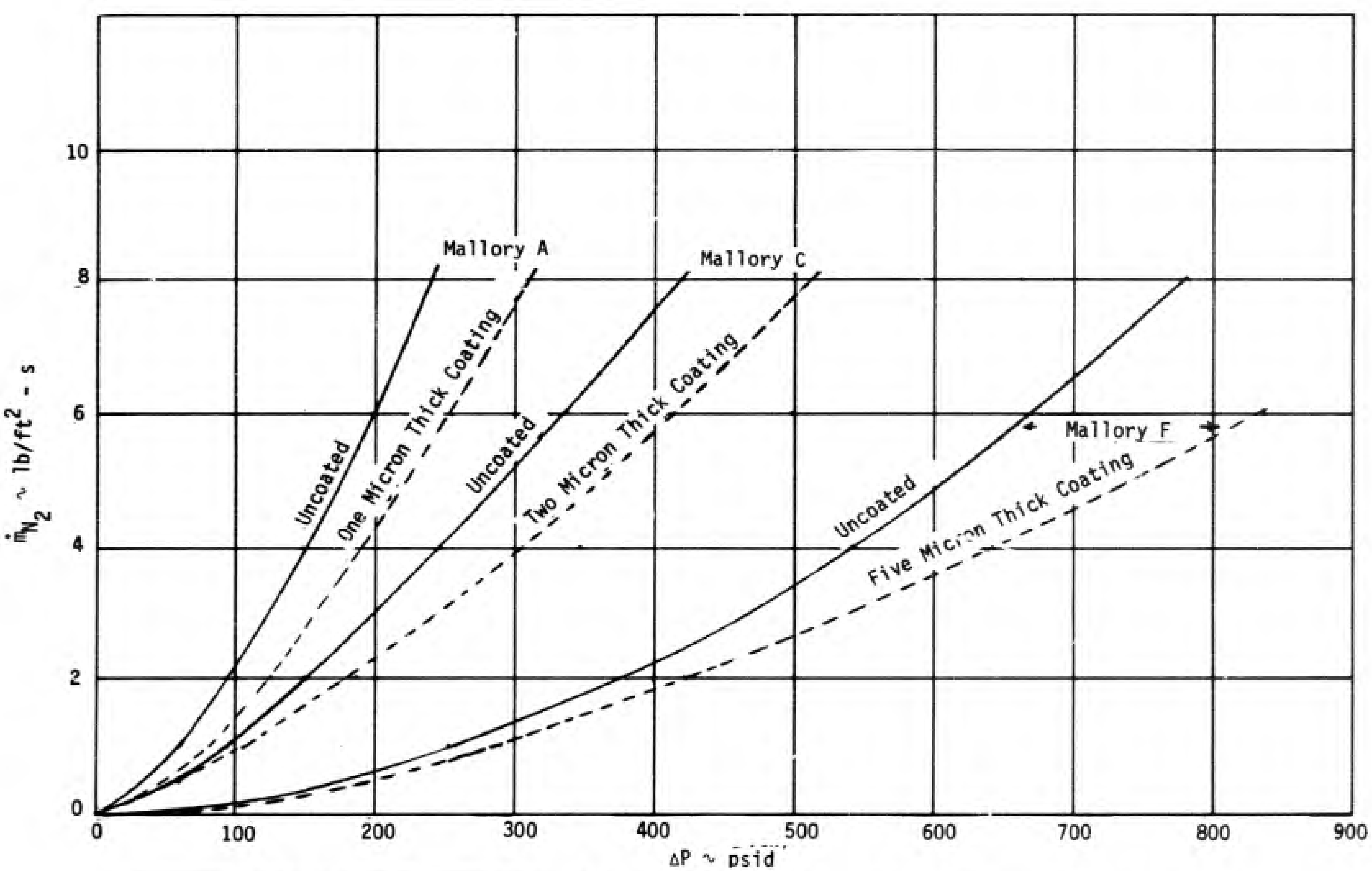

Figure 3-14. Effect of Tungsten Coating Thickness on Flow through Porous Tungsten

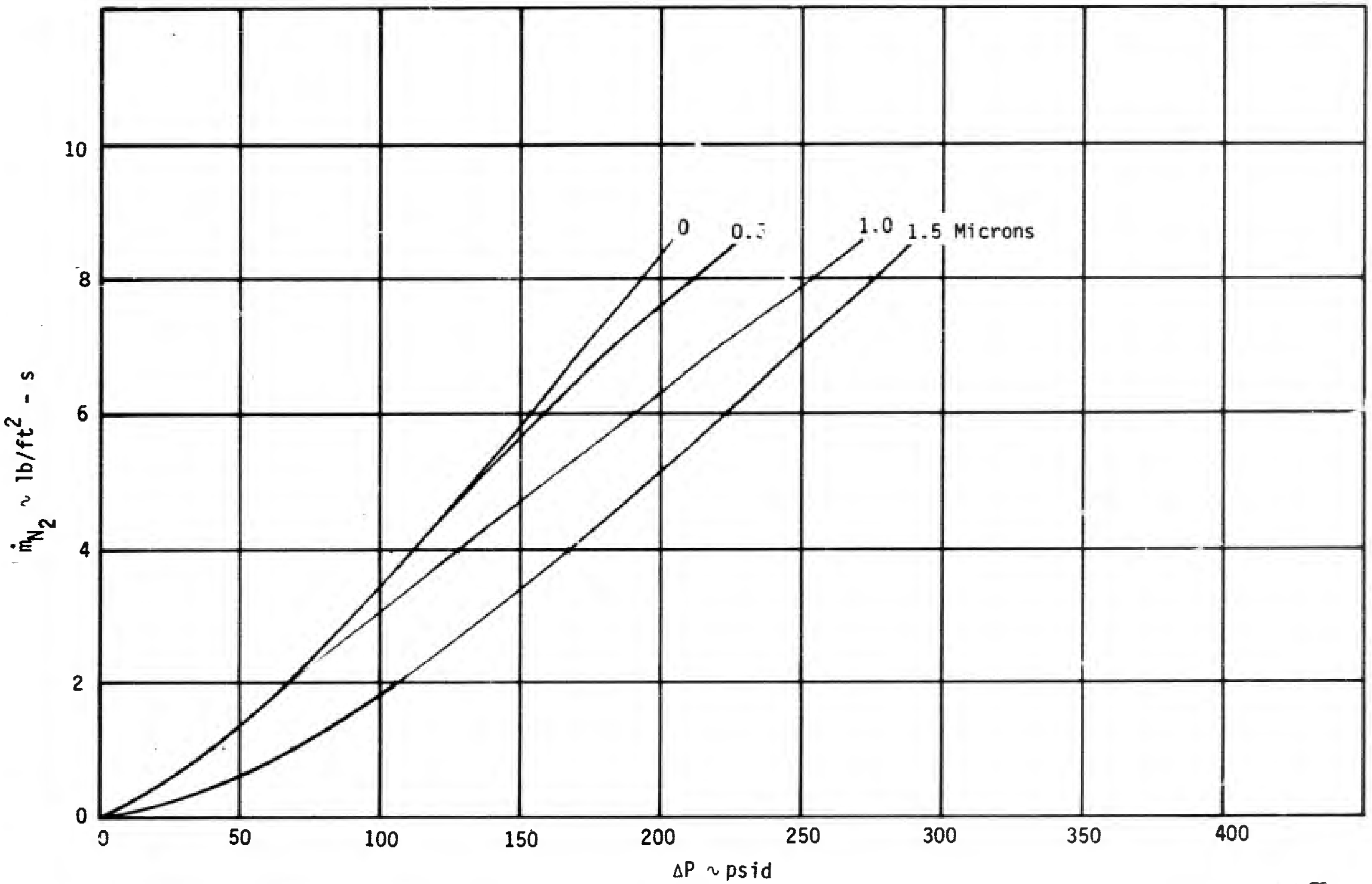

Figure 3-15. Effect of Gold Coating Thickness on Flow through Porous Tungsten

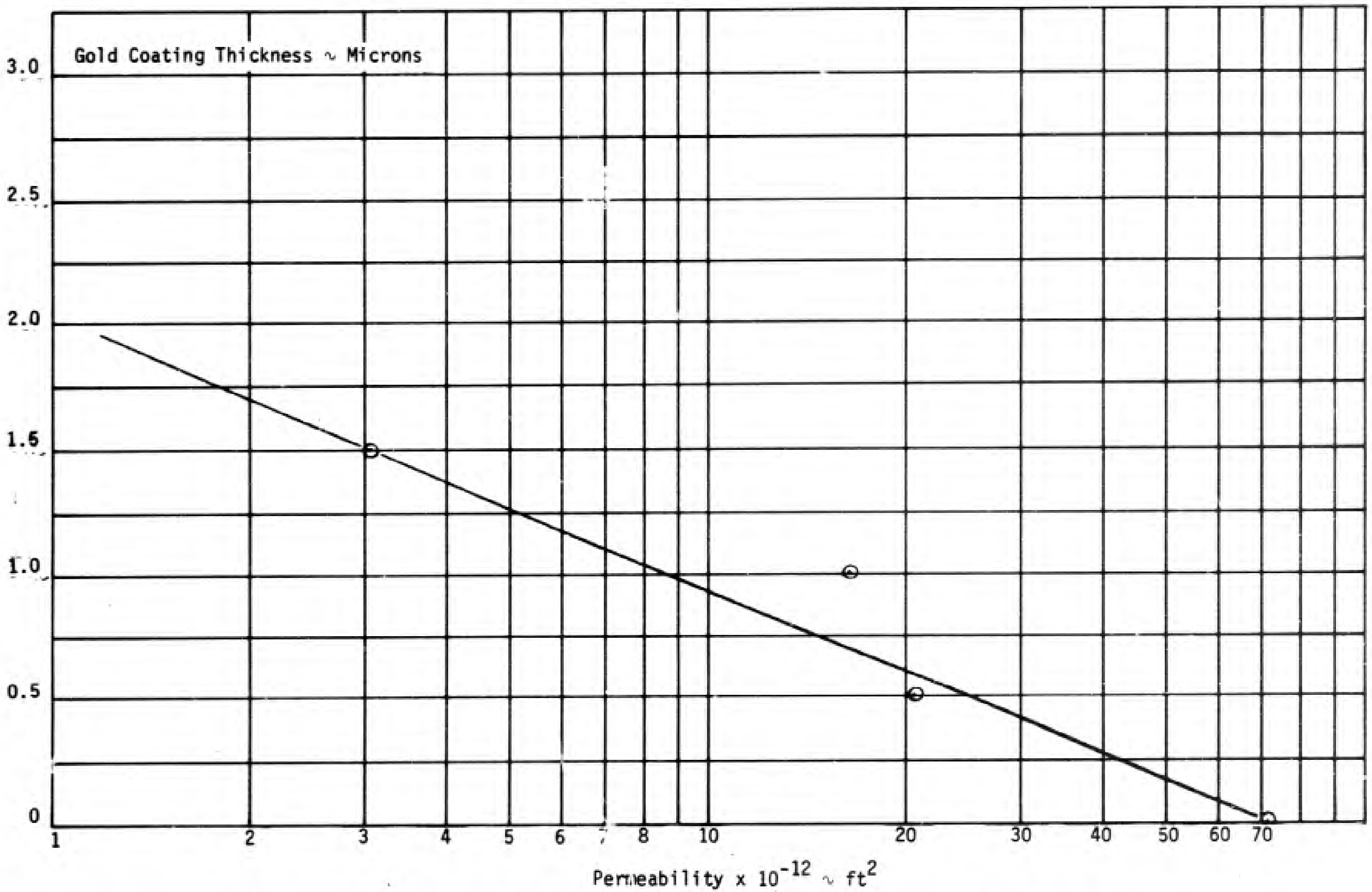

Figure 3-16. Effect of Gold Coating on Permeability of Astromet Porous Tungsten

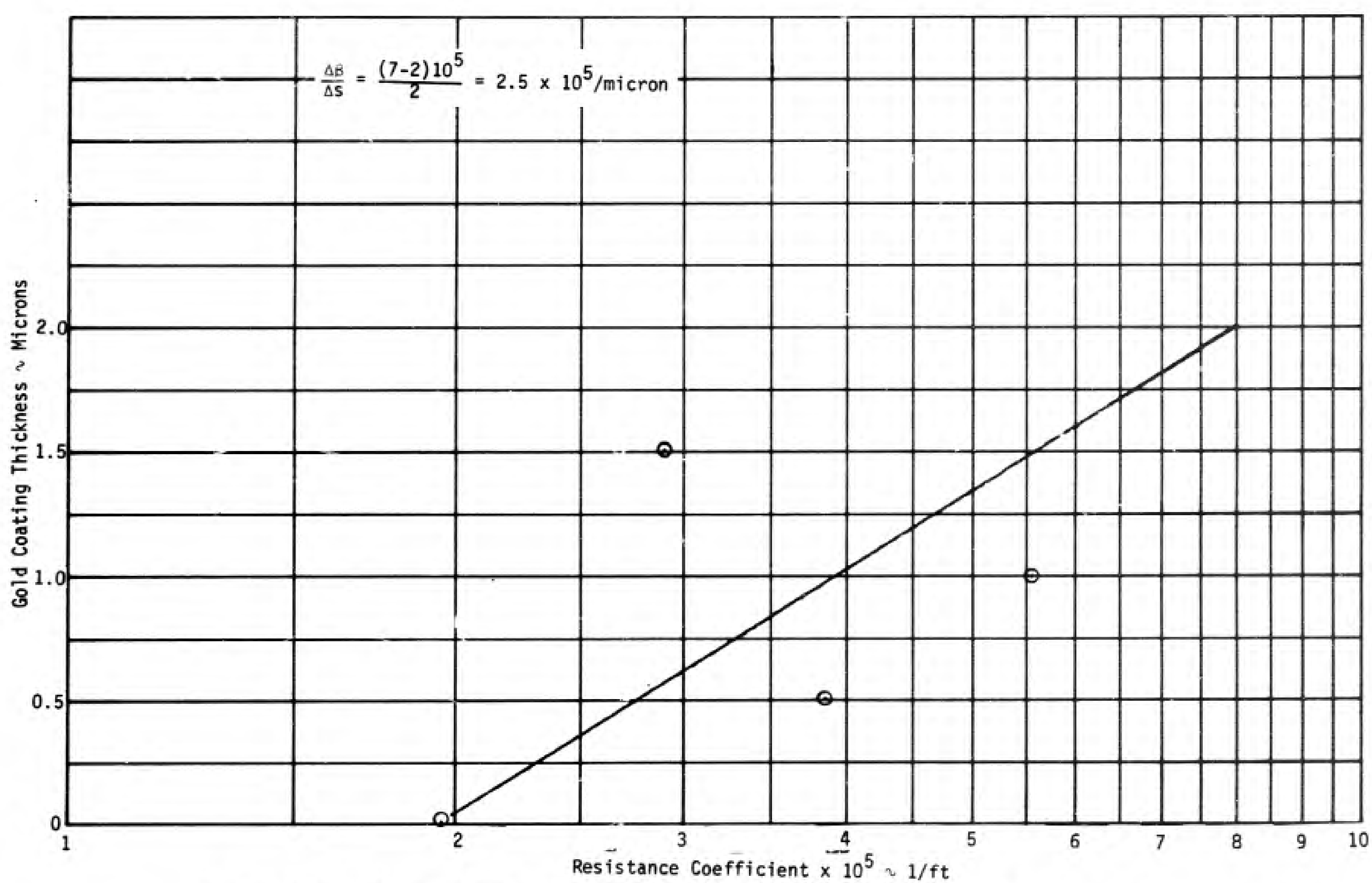

Figure 3-17. Effect of Gold Coating on Resistance Coefficient of Astromet Porous Tungsten

The porous tungsten material flow characteristics, for all the porous materials tested, can be represented by a plot of the reciprocal of the permeability as a function of inertial resistance coefficient. Although there is some scatter, the data is consistent. Figures 3-18 and 3-19 shows the effect of the volume percentage of tungsten on the inertial resistance coefficient. These two curves indicate a median value of expected flow characteristics properties of porous tungsten material once the percent tungsten by volume is known.

The data and the correlations presented in this part of the report can be used to select those materials whose flow characteristics best meet the requirements of the advanced interceptor mission.

3.2.1 Heat Transfer Coefficient Tests

The operating temperature of a CONAP nose tip or air vane leading edge is controlled by the flight environment, the ammonia flow rate, and the heat transfer rate between the porous tungsten and the ammonia coolant. In the ideal case of thermodynamic equilibrium, the heat transfer rate between the coolant and matrix is sufficiently high so that the local coolant temperature is equal to the local matrix temperature. In reality this does not occur. The rate of heat transfer is finite and is controlled by the internal heat transfer coefficient (h'). This results in a coolant temperature that is lower than the matrix temperature at any given point in the matrix. The efficiency of the CONAP concept depends on the amount of heat taken from the matrix by a given mass of coolant. In this study, laboratory experiments were devised to obtain the data necessary to calculate the internal heat transfer coefficient, in order to determine the effectiveness of the CONAP concept. A test fixture was built whereby an ammonia gas stream was passed through an inductively heated porous tungsten plug. Coolant flow rates ranged from 0.5 to 8 lb/ft^2-s and the tungsten plug was maintained at temperatures ranging from 2000°R to 5000°R in these experiments. The selection of these test conditions was based on estimates of required coolant flow rates and matrix temperature conditions on the nose tip of an advanced interceptor. Measurements taken in the heat transfer experiment included inlet and exit coolant temperature, matrix temperature, coolant flow rate, and upstream pressure. These measured data were then factored into a computer code (Appendix C) which computed the internal heat transfer coefficient. A detailed discussion of the test description, test procedure, test fixture and instrumentation is given in Appendix A. Test specimens were as described in Table 3-I.

The heat transfer coefficient data for the porous matrix concepts and the discrete hole concepts are presented separately. Because of the physical differences in these two cases, the data in each had to be correlated accordingly. Heat transfer from a tungsten matrix, which has discrete holes, to a coolant gas passing through, can be described by Newton's cooling law for a solid body convecting heat to a gas. Heat transfer from a porous tungsten matrix to a coolant gas passing through, is a volumetric phenonemon similar to heat source. Thus the surface heat transfer phenomena of the discrete hole matrix is correlated in a different manner from the volumetric heat transfer phenomena taking place in a porous matrix.

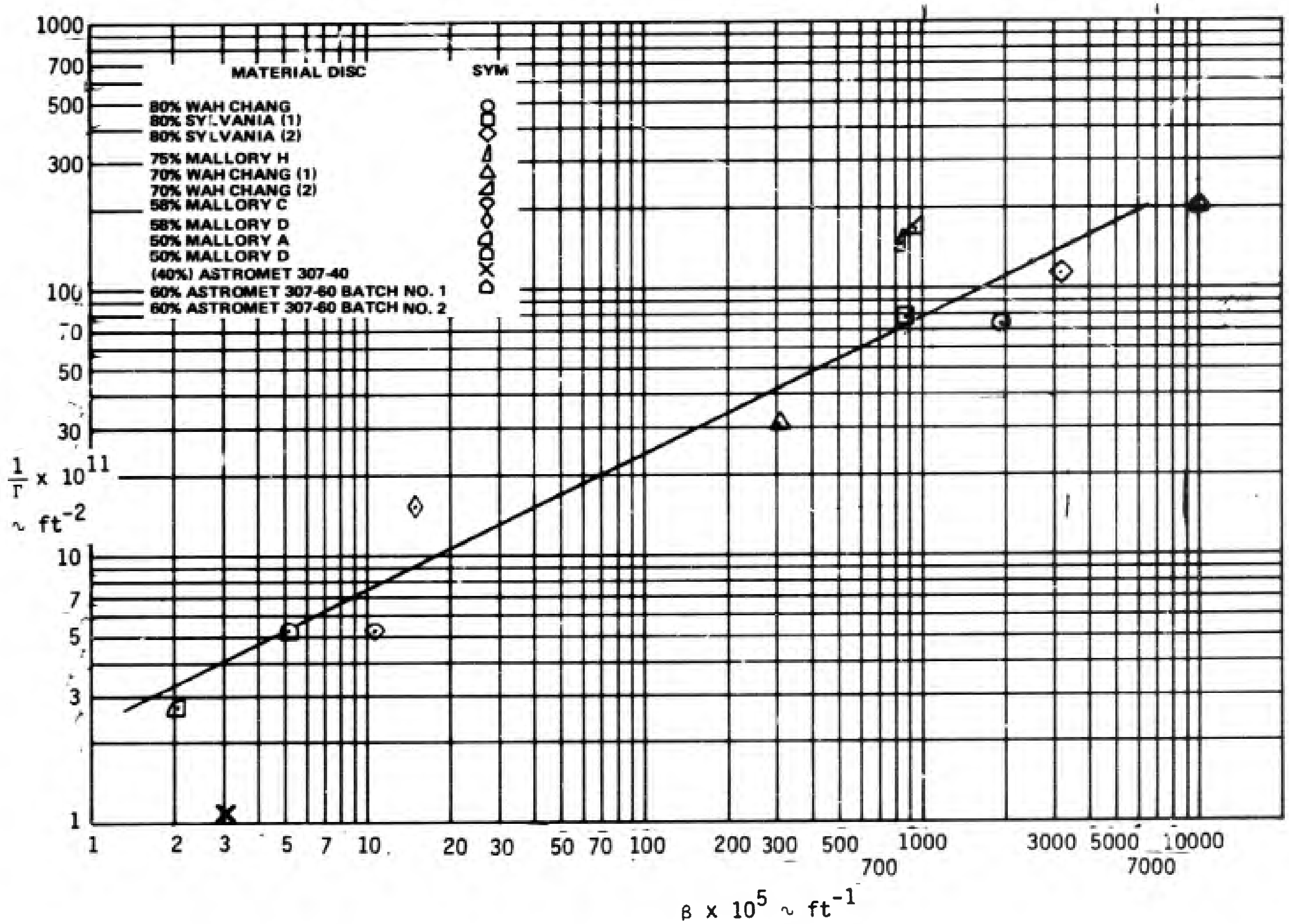

Figure 3-18. Sintered Tungsten Flow Correlation

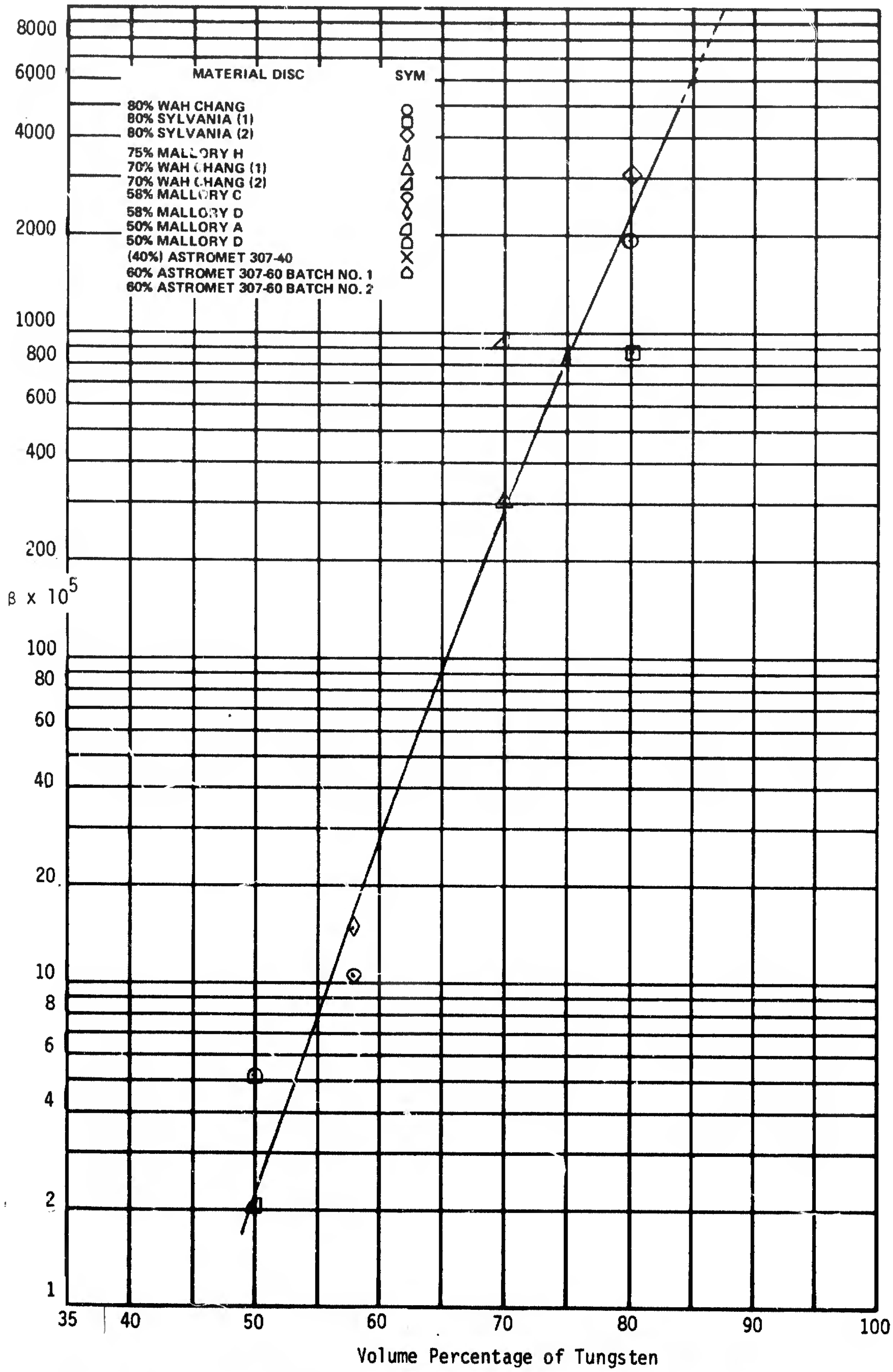

Figure 3-19. Effect of Volume Percentage on Resistance Coefficient

For the case of the porous materials, the heat transfer coefficient that was computed from the experimental data was correlated into a dimensionless format. The data were put into the form of Equation (1).

$$\frac{h'L}{\overset{\circ}{m}\ C_{p_c}} = A\,\frac{L\overset{\circ}{m}\ C_{p_c}}{k_m} + B\left(\frac{L\overset{\circ}{m}\ C_{p_c}}{k_m}\right)^2 \qquad (1)$$

where:

h' = heat transfer coefficient (Btu/ft^3-°R-s)
L = matrix thickness (feet)
$\overset{\circ}{m}$ = coolant flow rate (lb/ft^2-s)
C_{p_c} = coolant specific heat (Btu/lb-°R)
k_m = matrix thermal conductivity (Btu/ft-s-°R)
A,B = curve fit coefficients

For each specimen, the data were plotted as a function of

$$\frac{h'L}{C_{p_c}\overset{\circ}{m}} \text{ versus } \frac{L\overset{\circ}{m}\ C_{p_c}}{k_m} \qquad (2)$$

and a least squares curve fit was made to obtain the coefficients in Equation (1). The data are shown in Figure 3-20 through 3-28 and Table 3-VII. Figures 3-20, 3-21, and 3-22 show the data and the curve fit for the straight porous materials. The data for the porous specimens augmented with blind holes are shown in Figures 3-23 through 3-26. And finally, the data for the porous specimen with vapor deposited tungsten coatings are shown in Figures 3-27 and 3-28. The curve fit coefficients, A and B, as shown in Equation (1), corresponding to each separated specimen are tabulated in Table 3-VII.

Table 3-VIII tabulates values of $h'L/C_{pc}\ \overset{\circ}{m}$ as a function of $Lm\ C_{pc}/k_m$, as shown in Equation (2), for each of the curves shown in Figures 3-20 through 3-28. Table 3-VIII shows the range of heat transfer coefficient results among the specimen tested. From the lowest to the highest value of heat transfer coefficient, the variation is no more than a factor of three and for most cases it is much less. The specimen which had the lowest heat transfer coefficient at all values of $L\overset{\circ}{m}\ C_p/k_m$ was the porous tungsten Wah Chang specimen augmented with one blind hole. The Mallory A specimen had the highest heat transfer coefficient. Table 3-VIII also shows that as the number of blind holes are increased in a porous tungsten specimen, the heat transfer coefficient increases. In fact at the higher values of $L\overset{\circ}{m}\ C_{pc}/km$, which correspond to flow rates ranging from 4 to 8 lb/ft^2-s, the heat transfer coefficients for the nine blind hole and 25 blind hole cases were comparable and in some cases higher than some of the straight porous tungsten samples.

TABLE 3-VII

Heat Transfer Coefficient Correlations

Material Manufacturer	Specimen Identification	Percent Tungsten By Volume	Blind Hole Configuration	Tungsten Vapor Deposition Thickness	Coefficients* A	Coefficients* B	Reference Figure Number
Mallory	A	50			0.282	0.0172	3-20
Mallory	C	58			0.173	0.0119	3-21
Wah Chang	–	70			0.262	0.0063	3-22
Wah Chang	–	70	1 0.15 deep x 0.020 inch dia		0.091	0.0057	3-23
Wah Chang	–	70	9 0.15 deep x 0.020 inch dia		0.051	0.029	3-24
Wah Chang	–	80	25 0.06 deep x 0.020 inch dia		0.065	0.037	3-25
Wah Chang	–	80	25 0.09 deep x 0.020 inch dia		0.071	0.038	3-26
Mallory	A	50		1 micron	0.308	0.0	3-27
Mallory	F	65		5 microns	0.096	0.014	3-28

*These coefficients fit into the following equation.

$$\frac{h'L}{\dot{m}C_{P_c}} = A\left(\frac{L\dot{m}\,C_{P_c}}{k_m}\right) + B\left(\frac{L\dot{m}\,C_{P_c}}{k_m}\right)^2$$

TABLE 3-VIII

Comparison of the Heat Transfer Coefficients of the Materials Tested
$(h'L/C_{P_c}\,\dot{m})$

$\frac{L\dot{m}\,C_{P_c}}{k_m}$	Mallory A Porous	Mallory C Porous	Wah Chang 70 Porous	Wah Chang 70 1 Blind Hole	Wah Chang 70 9 Blind Holes	Wah Chang 80 25 0.06 Inch Blind Holes	Wah Chang 80 25 0.09 Inch Blind Holes	Mallory A, 1μ Coating	Mallory F, 5μ Coating
2	0.65	0.39	0.5	0.22	0.21	0.31	0.3	0.6	0.25
4	1.4	0.89	0.94	0.46	0.65	0.9	0.87	1.25	0.62
6	2.3	1.45	1.36	0.73	1.35	1.8	1.8	1.85	1.05
8	3.37	2.15	1.7	1.1	2.25	3.0 Extrapolated	3.0	2.46	1.65

TABLE 3-IX

Comparison of Test Conditions Under Which Heat Transfer Coefficient Data Was Taken

Parameter	Present Study	Grootenhuis Reference	Schneider et al	Marco and Han
Matrix material	Porous tungsten	Stainless steel	Stainless steel	Steel wool
Matrix temperature range	1000°R – 5000°R	500°R – 700°R	700°R	600°R
Coolant	Gaseous ammonia M = 17	Air M = 29	Water M = 18	Air M = 29
Mass flow range	0.5 – 8.0 lbs/ft^2-s	7 – 16 lbs/ft^2-s	1 – 8 lbs/ft^2-s	0.1 – 0.6 lbs/ft^2-s
Heat transfer coefficient range	2 – 2500 Btu/ft^3-°R-s	600 – 1200 Btu/ft^3-°R-s	550 – 1750 Btu/ft^3-s-°R	0.2 – 3.5 Btu/ft^3-s-°R

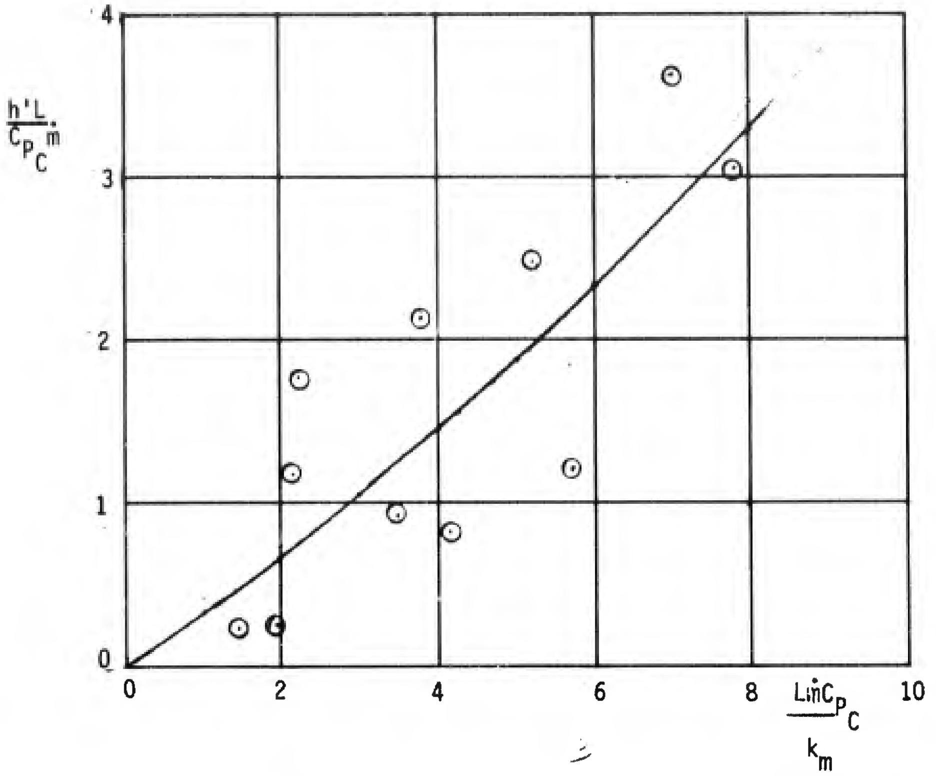

Figure 3-20. Heat Transfer Coefficient for Mallory C Sintered Tungsten (50 Percent Dense)

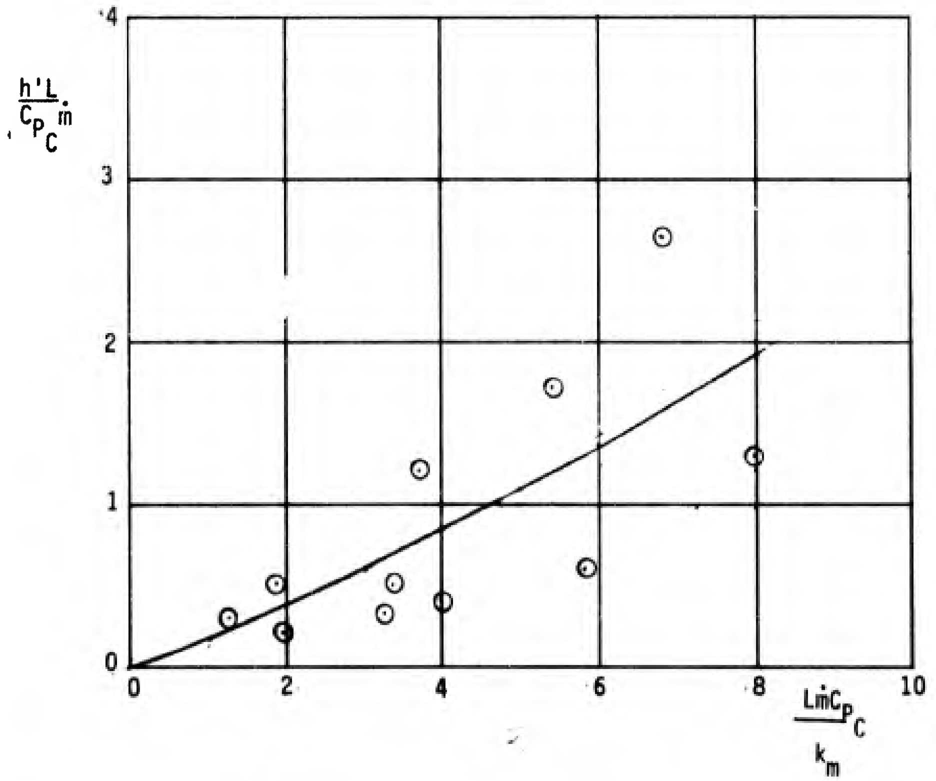

Figure 3-21. Heat Transfer Coefficient for Mallory A Sintered Tungsten (58 Percent Dense)

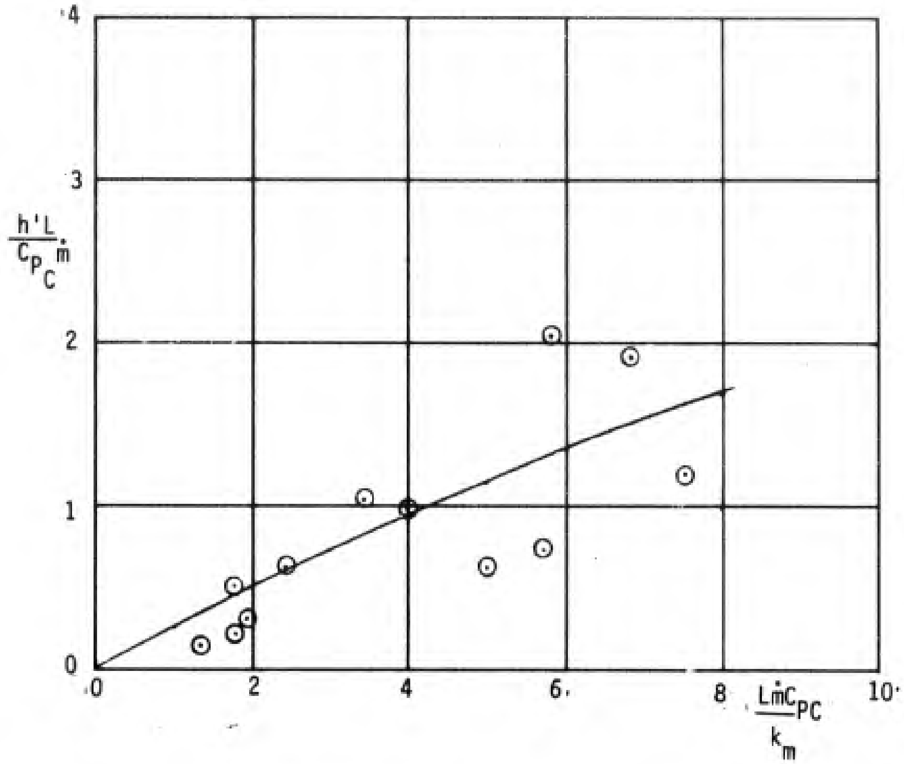

Figure 3-22. Heat Transfer Coefficient for Wah Chang Sintered Tungsten (70 Percent Dense)

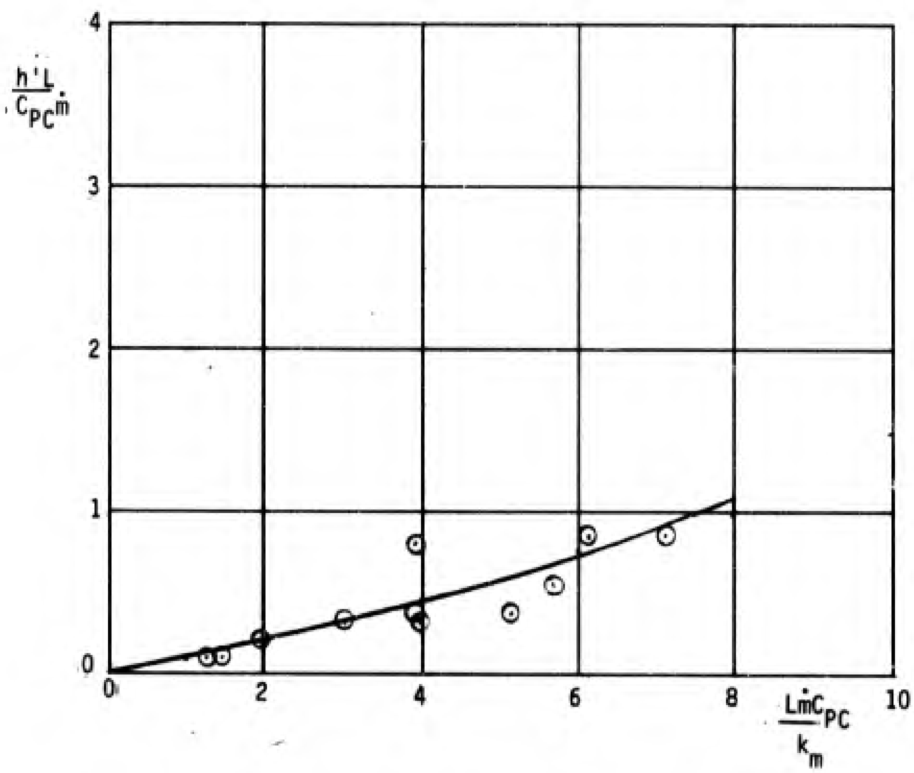

Figure 3-23. Heat Transfer Coefficient for One-Blind-Hole Wah Chang (70 Percent Dense)

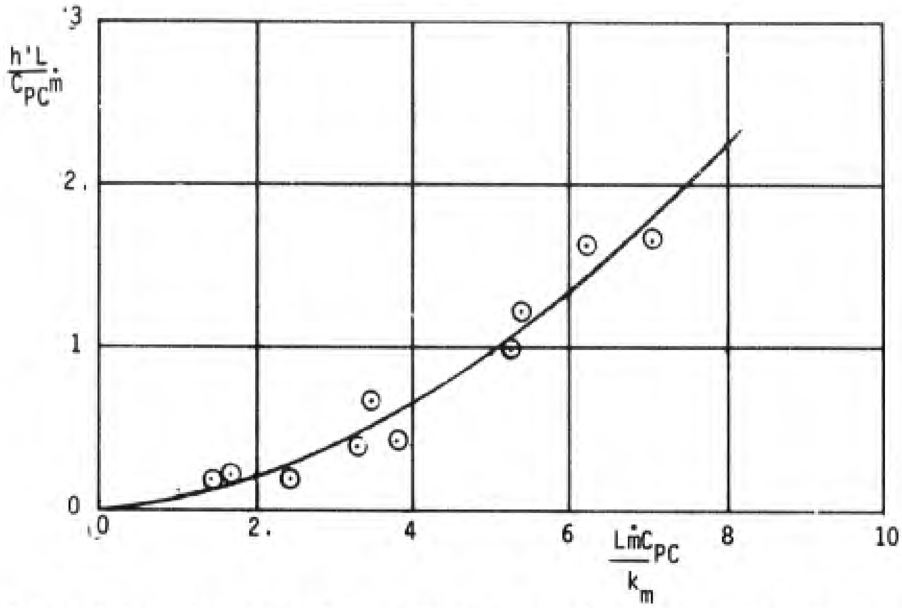

Figure 3-24. Heat Transfer Coefficient for Nine-Blind-Holes Wah Chang (70 Percent Dense)

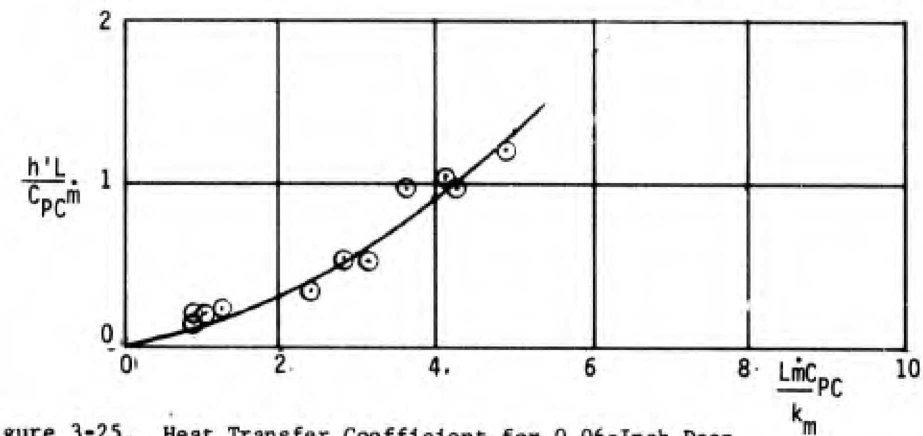

Figure 3-25. Heat Transfer Coefficient for 0.06-Inch Deep Blind Hole Wah Chang (80 Percent Dense)

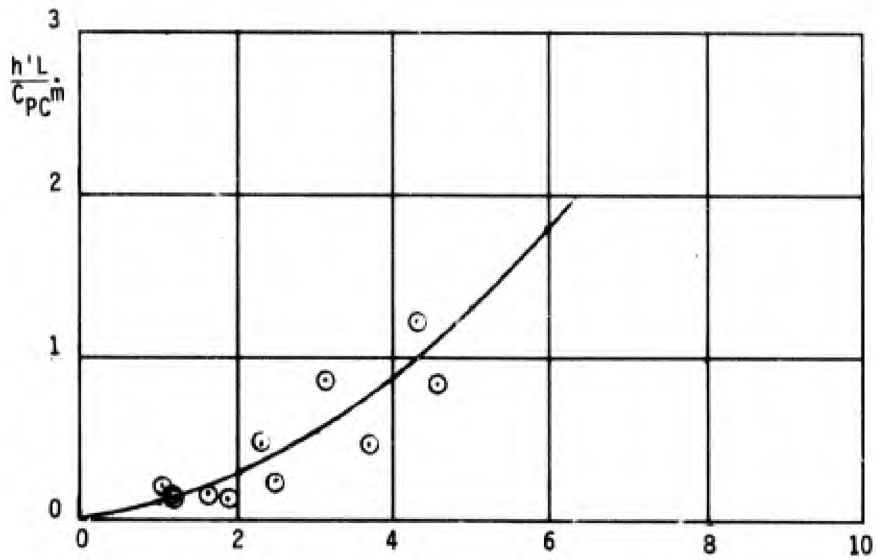

Figure 3-26. Heat Transfer Coefficient for 0.09 inch Deep Blind Holes Wah Chang (80 Percent Dense)

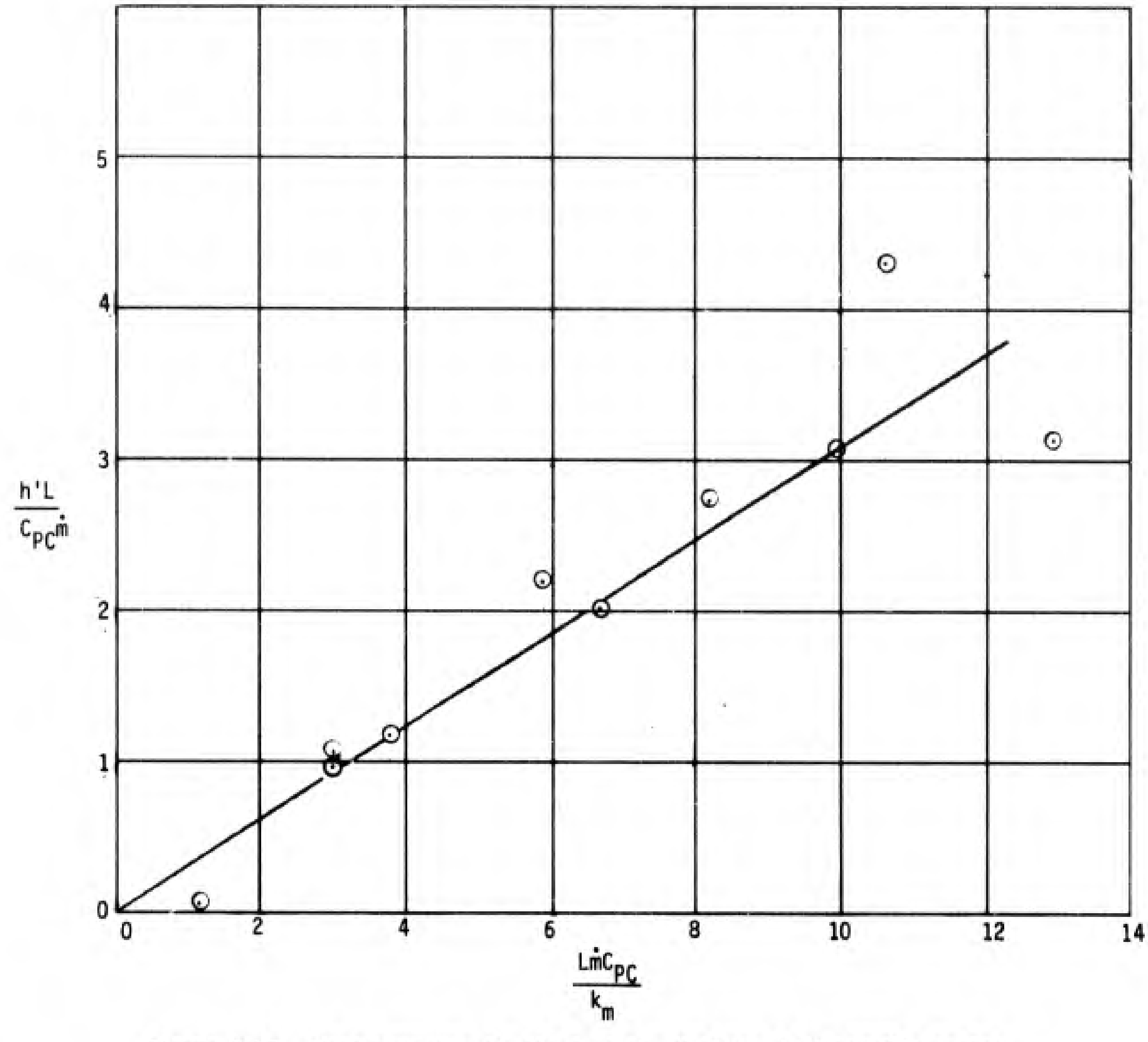

Figure 3-27. Heat Transfer Coefficient For Mallory A Sintered Tungsten With a One Micron Thick Tungsten Coating

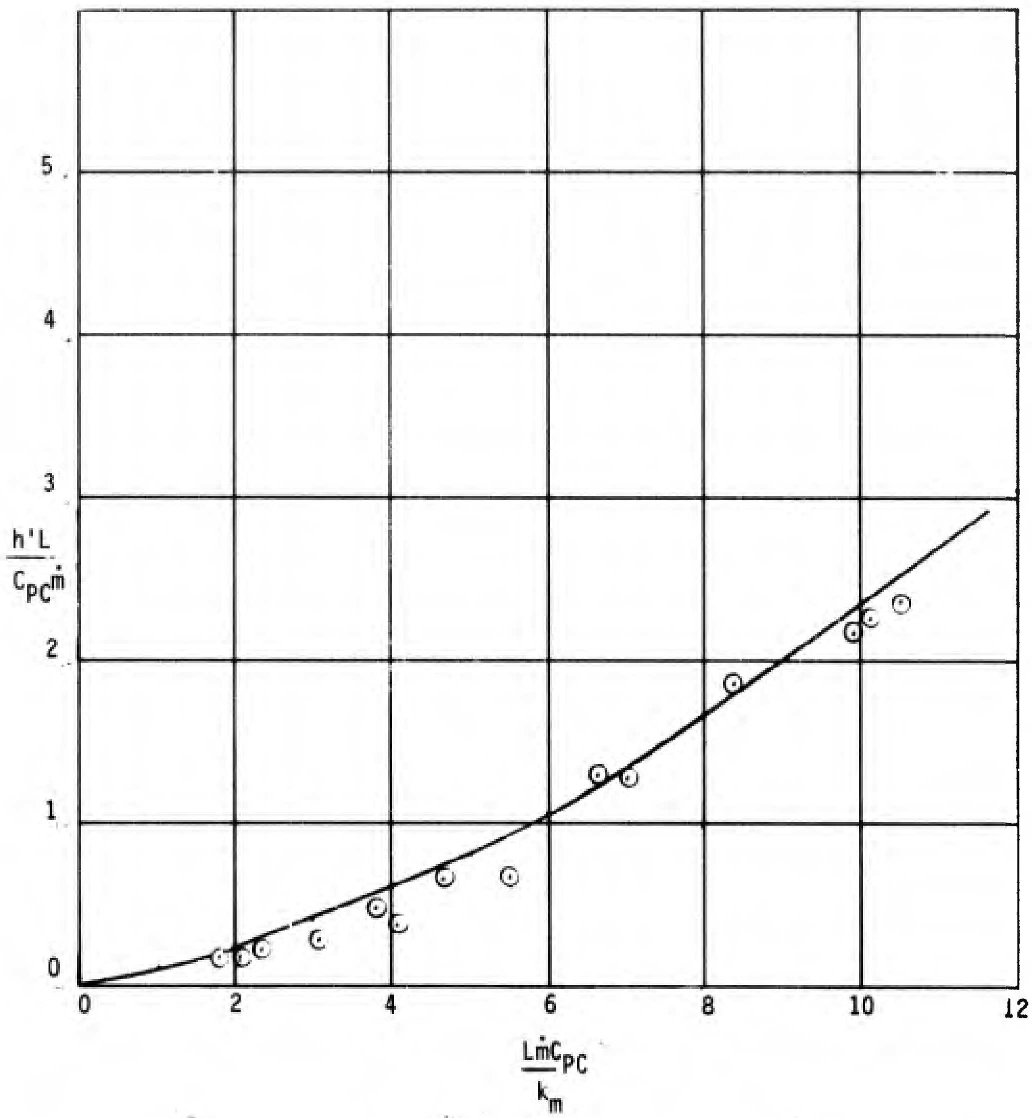

Figure 3-28. Heat Transfer Coefficient For Mallory F Sintered Tungsten With Five Microns Thick Coating

A comparison of the data presented here and data obtained from literature is shown in Table 3-IX and Figure 3-29. The current data was taken at conditions that were vastly different from the other data. The data taken from literature do verify, however, that the trend of the current data is correct. Figure 3-29 shows that the current data is in good agreement with that of Marco and Han, Reference 8, with the latter being at the low end of the current data. The current data however, is lower than Schneider, Reference 9, who used water as a coolant in a stainless steel matrix. This is to be expected since liquids have higher heat transfer coefficients than gases. Thus the Schneider data, the Marco and Han data, and the current data are consistant. The data of Grootenhaus, Reference 10, who used hot air that was cooled by flowing through a stainless steel matrix, agrees with Schneider's data, which is physically not consistent.

The discrete hole heat transfer data are compared to Nunner's equation (Reference 11), for heat transfer in smooth pipes. This equation,

$$\frac{Nu_d}{R_{e_d}\ Pr} = \frac{0.0396\ (R_{e_d})^{-1/4}}{1 + A(R_{e_d})^{-1/8}\ [Pr\ (f/f_0) - 1]} \qquad (3)$$

where:

$$A = 1.5\ P_r^{-1/6}$$

shows excellent agreement with the data when the Prandtl number is corrected for ammonia gas as shown in Figure 3-30. The data itself have been correlated as a function of Reynolds number. The correlation equation used is shown in Equation (4).

$$Nu_d = A\ R_{e_d} + B\ R_{e_d}^{\ 2} + C\ R_{e_d}^{\ 3} \qquad (4)$$

where:

Nu_d = Nusselt number based on the discrete hole diameter

R_{e_d} = Reynolds number based on the discrete hole diameter

A,B,C = correlation coefficients

Table 3-X gives the correlation coefficients that fit into this equation for the cases tested.

3.3 Schlieren System Test

A Schlieren system was used to ''view'' the flow emerging from several of the configurational concepts that have been tested for flow characteristics and heat transfer coefficient. The Schlieren system, described in

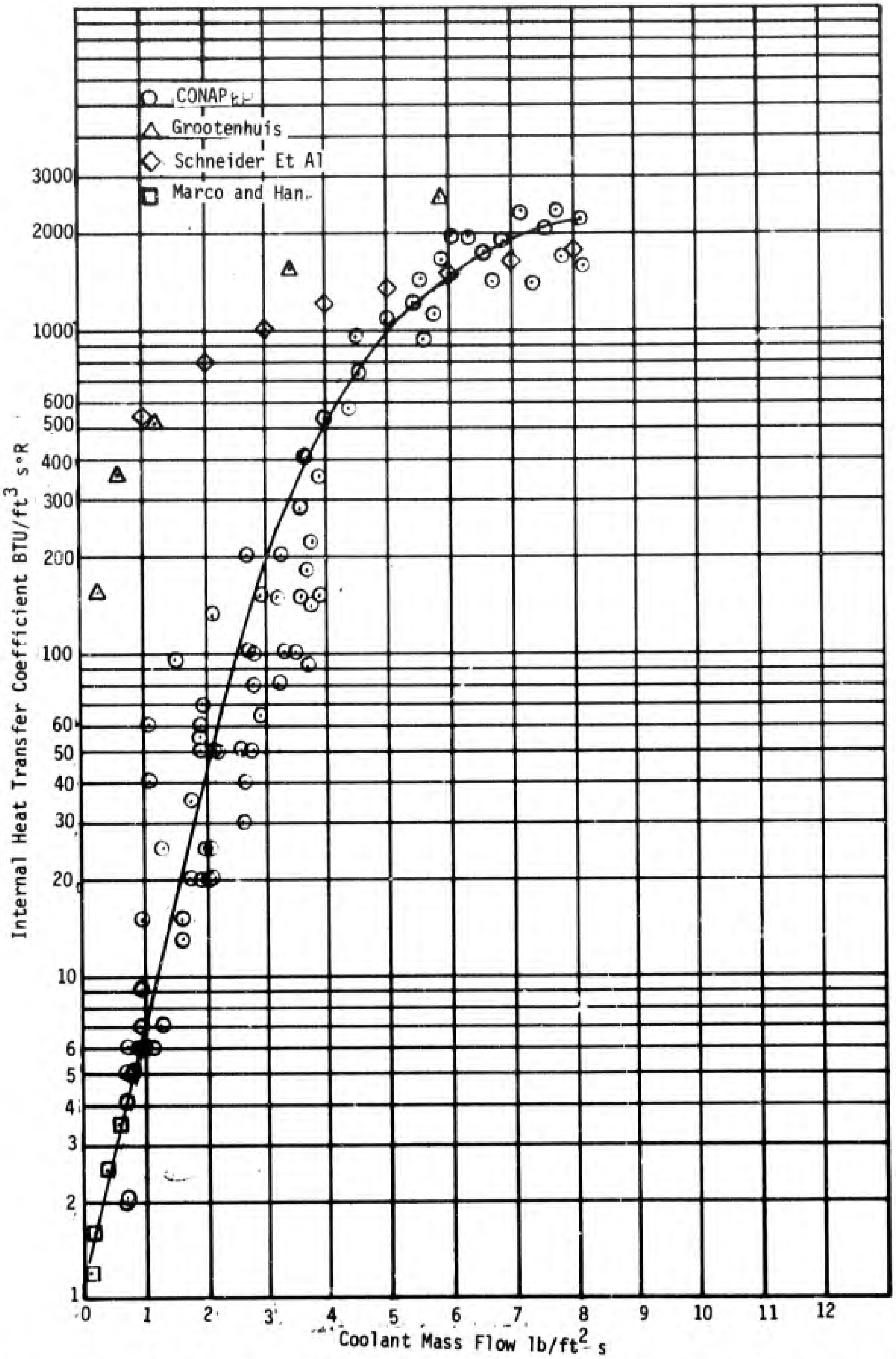

Figure 3-29. Comparison of CONAP Internal Heat Transfer Coefficient with Available Data

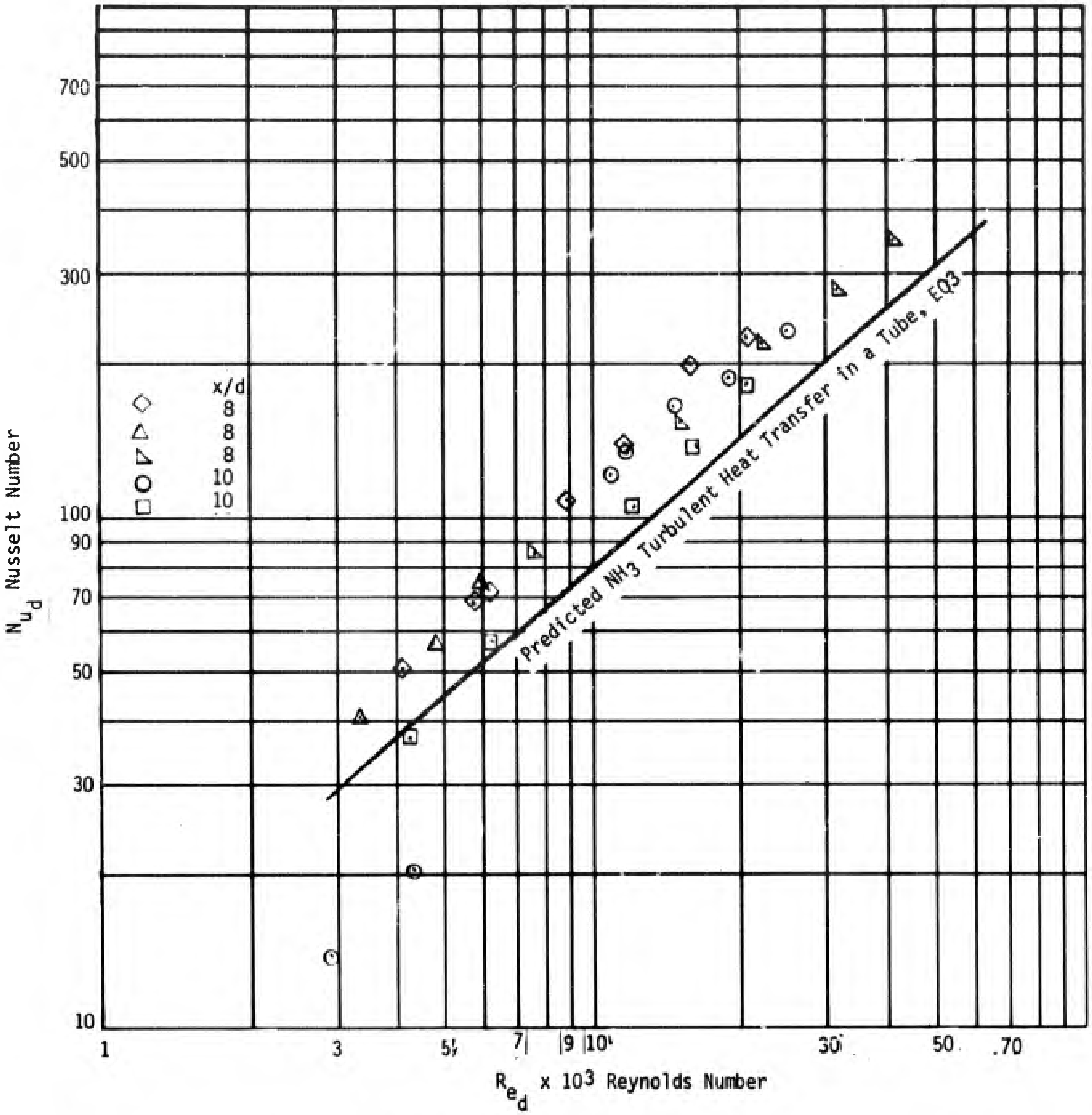

Figure 3-30. Discrete Hole Film Heat Transfer Coefficient for NH_3 Vapor (80 Percent Wah Chang)

more detail in Appendix B, is a system whereby density gradients in the flow field are distinguishable and can be viewed on a screen or recorded on film. In order for significant density gradients at room temperature to exist in subsonic flow, gases with a wide variation of molecular weight must be used. Thus, helium gas was used as the coolant in the tungsten matrix. The helium gas exited the matrix into air at room temperature and 1 atm pressure.

TABLE 3-X

Correlation Coefficients for the Heat Transfer to Ammonia Gas Passing Through A Hot Discrete Hole Tungsten Matrix

Material	Discrete Hole Configuration	Correlation Coefficients*		
		A	B	C
80 percent Wah Chang	5 through holes 0.025 inch dia	0.8137×10^{-2}	0.2945×10^{-6}	-0.1025×10^{-10}
80 percent Wah Chang	5 through holes 0.031 inch dia	0.99×10^{-2}	0.5239×10^{-6}	-0.2315×10^{-10}
80 percent Wah Chang	1 through hole 0.030 inch dia	1.031×10^{-2}	-0.4769×10^{-6}	0.3079×10^{-12}

*Correlation coefficients for Equation 4.

$$Nu_d = A R_{e_d} + B R_{e_d}^{2} + C R_{e_d}^{3}$$

The density of helium is roughly one-seventh of air at the same pressure and temperature, thereby giving a density gradient large enough for the Schleiren system to distinguish flow patterns. The computed helium mass flow rates are much lower than ammonia-nitrogen flow rates expected to be used in a flight case because of the great density difference.

All of the materials to be viewed in the Schlieren were bonded to the holder with epoxy around the periphery of the specimen. In this procedure emphasis was placed on the prevention of leaks between the holder and the edges of the specimen. Blank specimen were used to assure the bonding process had in fact, sealed the sides to prevent leaks under all upstream pressure conditions.

Photos were taken of helium through an open pipe, shown in Figure 3-31, and photos were taken of helium flow through a discrete hole as shown in Figures 3-32 and 3-33. These runs were used as an ''index'' for the other cases in this experiment in the sense that they represent limiting cases of the porous material on one hand and the blind hole concept on the other. Note that in Figure 3-33 which shows the flow through a matrix with 5 through holes there is obvious coolant starvation in the areas next to and between the discrete holes. Although this is not an unexpected result it will serve as a contrast when compared to the porous tungsten matrix augmented with blind holes.

OPEN PIPE
f = 5.6
Speed = 1/400 sec.
$\dot{m} = 0.3 \times 10^{-4}$ lb/sec.

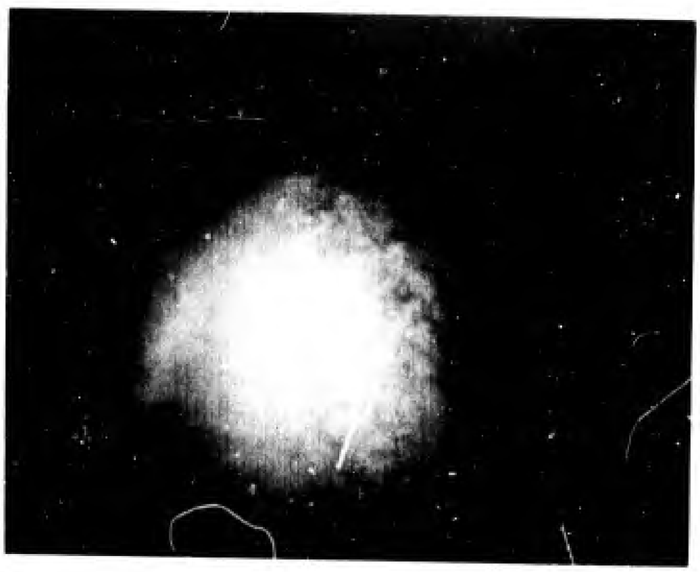

OPEN PIPE
f = 5.6
Speed = 1/400 sec.
$\dot{m} = 2.4 \times 10^{-4}$ lb/sec.

Figure 3-31. Schlieren Photograph, Open Pipe

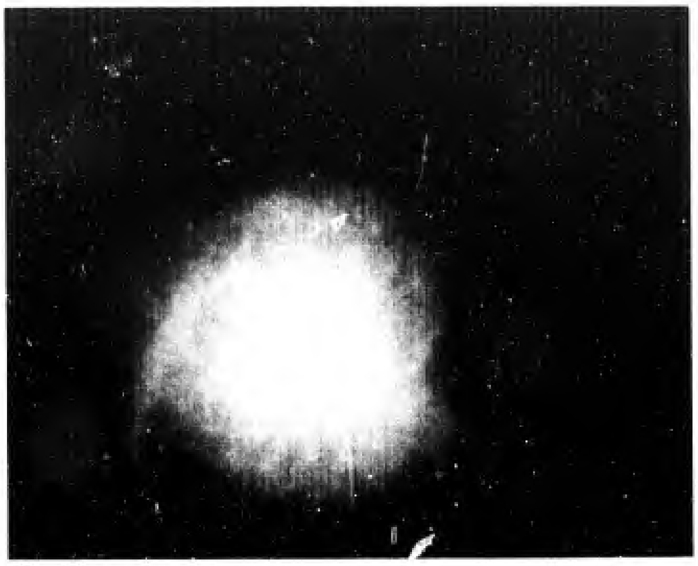

80 Percent
Wah Chang
1 through hole
f = 5.6
Speed = 1/400 sec.
$\dot{m} = 0.5 \times 10^{-4}$ lb/sec.

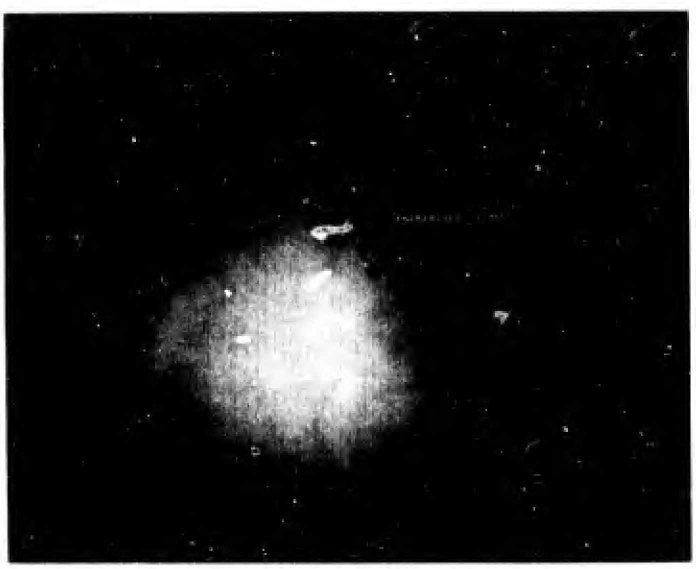

80 percent
Wah Chang
1 through hole
f = 5.6
Speed = 1/400 sec.
$\dot{m} = 2.4 \times 10^{-3}$ lb/sec.

Figure 3-32. Schlieren Photograph, 80 Percent Wah Chang, 1 through Hole

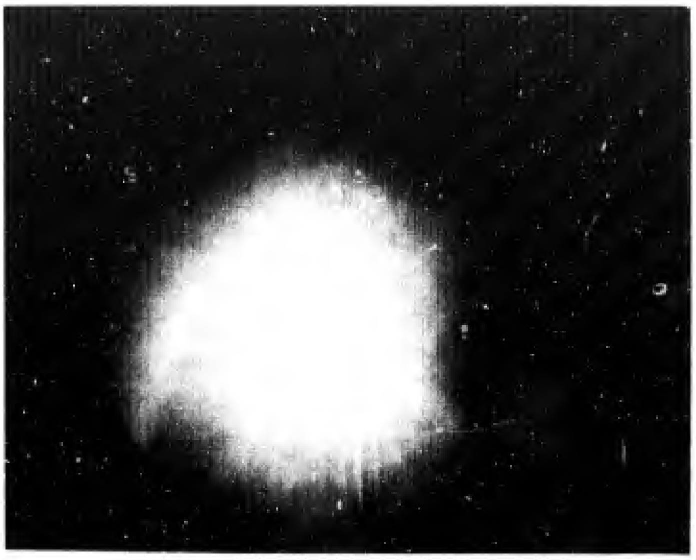

80 percent
Wah Chang
5 thru holes
f = 5.6
Speed = 1/400 sec.
$\dot{m} = 0.3 \times 10^{-4}$ lb/sec.

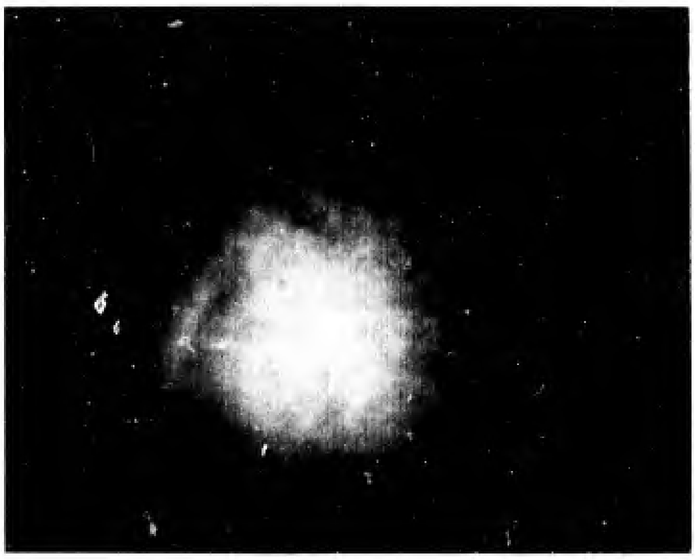

80-20 w-Cu
Wah Chang
5 thru noles
f = 5.6
Speed = 1/400 sec.
$\dot{m} = 1.2 \times 10^{-4}$ lb/sec.

Figure 3-33. Schlieren Photograph, 80 Percent Wah Chang, 5 through Holes

The flow fields emerging from the Astro Met materials are shown in Figures 3-34 through 3-37. Astro Met 307-40, which is 40 percent by volume tungsten and Astro Met 307-60 batch No. 1, which is 60 percent by volume tungsten, not only have the same flow characteristics but also seem to have downstream flow fields that are similar. It appears that these two materials have ''discrete holes'' amidst their interconnected porosity. This is borne out by the scanning electron microscope photographs which show large void areas which probably account for the flow behavior. Flow through the Astro Met 307-60 batch No. 1 material with gold coating on the downstream side seems to decrease the ''discrete hole'' effect of the earlier photos. The Astro Met 307-60 batch No. 2 material appears to be more uniform than the batch No. 2 material in the sense that the emerging flow, shown in Figure 3-35, does not have ''discrete hole'' effect to the same magnitude as the 307-60 batch No. 1 material. This is not unexpected since a comparison of Figures 3-23 and 3-25 shows that there are fewer large holes in the Astro Met 307-60 batch No. 2 material.

Figure 4-38 shows the flow emerging from the Mallory C material. Although this material is only 58 percent tungsten by volume, the flow is more uniform than the Astro Met materials. Scanning electron microscope photographs show that the material does not contain a significant amount of large pores. Figure 3-39 shows the flow emerging from the 70 percent Wah Chang material. The uniform flow field emerging from this material can be expected since the 50X, 250X and 1000X photographs in Chapter 2 show a very uniform material.

Figures 3-40, 3-41, and 3-42 show the flow emerging from the 80 percent Wah Chang material augmented with 25 blind holes, the 70 percent Wah Chang material augmented with 9 blind holes, and the 70 percent Wah Chang material augmented with 5 blind holes. In all cases the blind holes were on the downstream (exit) side of the specimen. These figures show that there is no flow starvation in those areas where there are no holes. This is an obvious conclusion when these photos are compared with the discrete flow case shown in Figures 3-31, 3-32, and 3-33 which clearly show the ''no flow condition'' between the discrete holes. The fact that blind holes increase the local flows without starving other local areas can be used to great advantage in the final design of a nose tip or air vane leading edge.

A porous nose tip augmented with blind holes at the stagnation point and the sonic point was made from 80 percent Wah Chang material. Helium flow emerging from this nose tip is shown in Figure 3-43. These photographs show that there is flow emerging between the blind holes and from the sidewall.

Astro Met 307-40(3)
f = 5.6
Speed = 1/400 s
$\dot{m} = 0.3 \times 10^{-4}$ lb/sec.

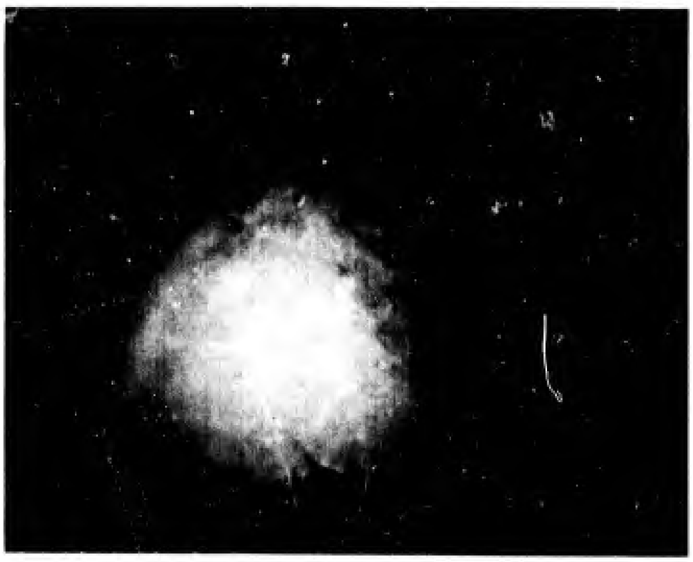

Astro Met 307-40(3)
f = 5.6
Speed = 1/400 s
$\dot{m} = 2.4 \times 10^{-4}$ lb/sec

Figure 3-34. Schlieren Photograph, Astro Met 307-40

Astro Met 307-60(2)
f = 5.6
Speed = 1/400 s
$\dot{m}$ = 0.4 x 10^{-4} lb/sec.

Astro Met 307-60(2)
f = 5.6
Speed = 1/400 s
$\dot{m}$ = 0.5 x 10^{-4} lb/sec

Figure 3-35. Schlieren Photograph, Astro Met 307-60(2)

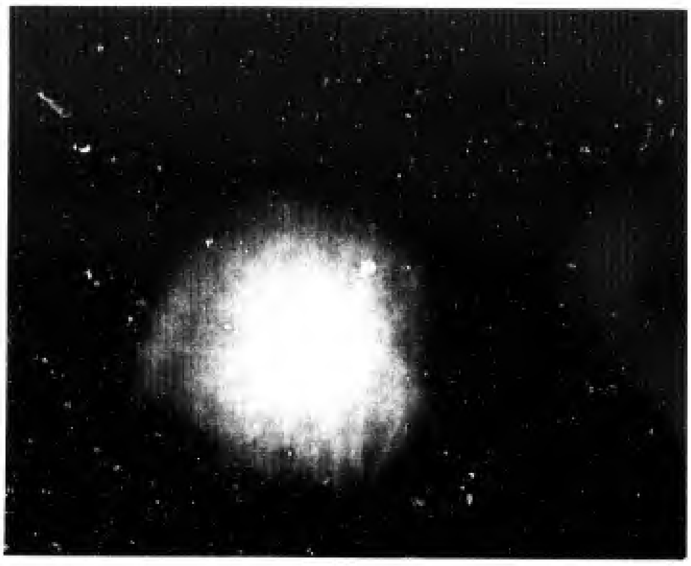

Astro Met 307-60(6)
Batch No. 1
Gold Coated
f = 5.6
Speed = 1/400 s
Coating Downstream
$\dot{m} = 0.3 \times 10^{-4}$ lb/sec.

Astro Met 307-60(6)
Gold Coated
f = 5.6
Speed = 1/400 s
Coating Downstream
$\dot{m} = 2.4 \times 10^{-4}$ lb/sec.

Figure 3-36. Schlieren Photograph, Astro Met 307-60, Gold Coated

Astro Met 307-60(1)
Batch No. 2
f = 5.6
Speed = 1/400 s
$\dot{m} = 2.4 \times 10^{-4}$ lb/sec.

Astro Met 307-60(1)
Batch No. 2
f = 5.6
Speed = 1/400 s
$\dot{m} = 0.3 \times 10^{-4}$ lb/sec

Figure 3-37. Schlieren Photograph, Astro Met 307-60(1)

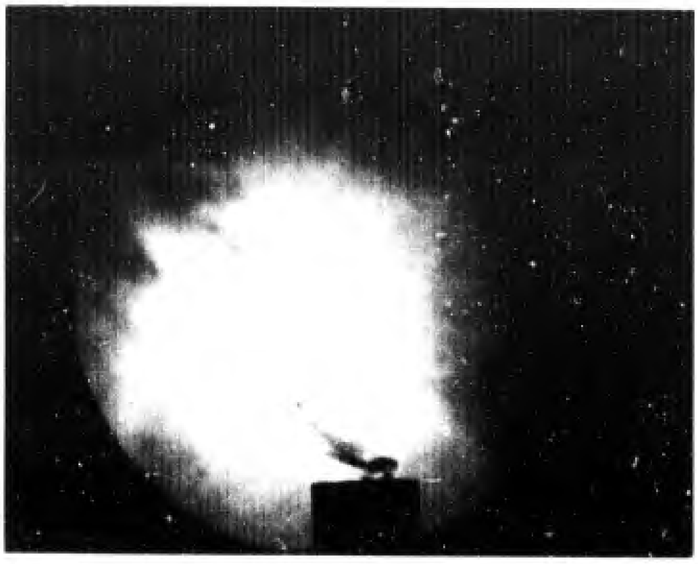

Mallory C 58%
f = 5.6
Speed = 1/400 s
$\dot{m} = 0.3 \times 10^{-4}$ lb/sec.

Mallory C
f = 5.6
Speed = 1/400 s
$\dot{m} = 2.1 \times 10^{-4}$ lb/sec.

Figure 3-38. Schlieren Photograph, Mallory C

70 percent Wah Chang
f = 5.6
Speed = 1/400 s
$\dot{m} = 0.3 \times 10^{-4}$ lb/sec.

Figure 3-39. Schlieren Photograph, 70 Percent Wah Chang

80 percent Wah Chang
f = 5.6
Speed = 1/400 s.
$\dot{m}$ = 0.3 x 10^{-4} lb/sec.
25 Blind Holes

80 percent Wah Chang
f = 5.6
Speed = 1/400 s
$\dot{m}$ = 0.9 x 10^{-4} lb/sec.
25 Blind Holes

Figure 3-40. Schlieren Photograph, 80 Percent Wah Chang, 25 Blind Holes

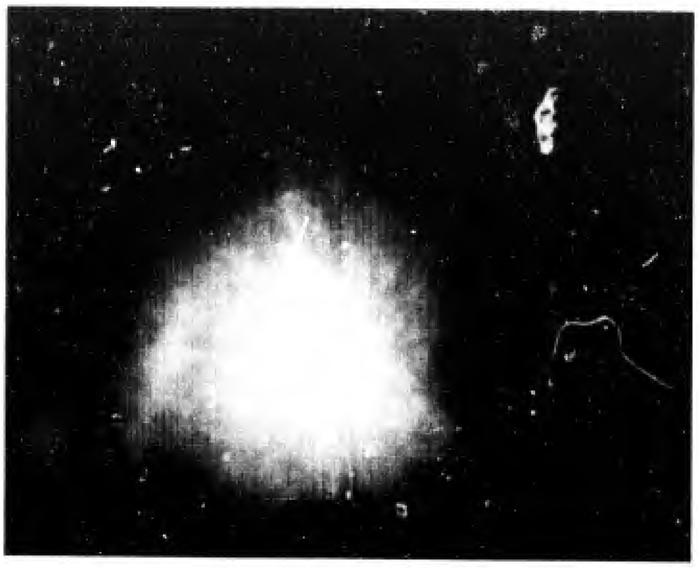

70 percent Wah Chang
f = 5.6
Speed = 1/400 s
$\dot{m} = 0.3 \times 10^{-4}$ lb/sec.
9 Blind Holes

70 percent Wah Chang
f = 5.6
Speed = 1/400 s
$\dot{m} = 1.1 \times 10^{-4}$ lb/sec.
9 Blind Holes

Figure 3-41. Schlieren Photograph, 70 Percent Wah Chang, 9 Blind Holes

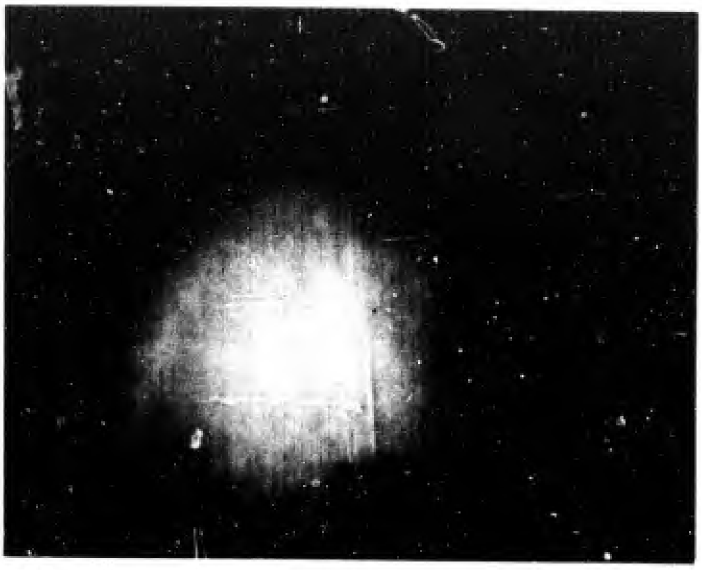

70 percent Wah Chang
f = 5.6
Speed = 1/400 s
$\dot{m} = 0.3 \times 10^{-4}$ lb/sec.
5 Blind Holes

70 percent Wah Chang
f = 5.6
Speed = 1/400 s
$\dot{m} = 1.2 \times 10^{-4}$ lb/sec.
5 Blind Holes

Figure 3-42. Schlieren Photograph, 70 Percent Wah Chang, 5 Blind Holes

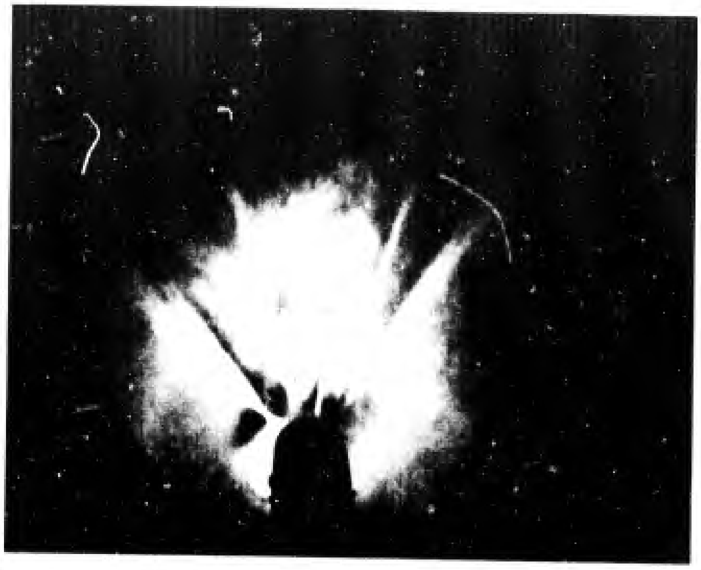

NOSE CAP
$\dot{m} = 1.4 \times 10^{-4}$ lb/sec.

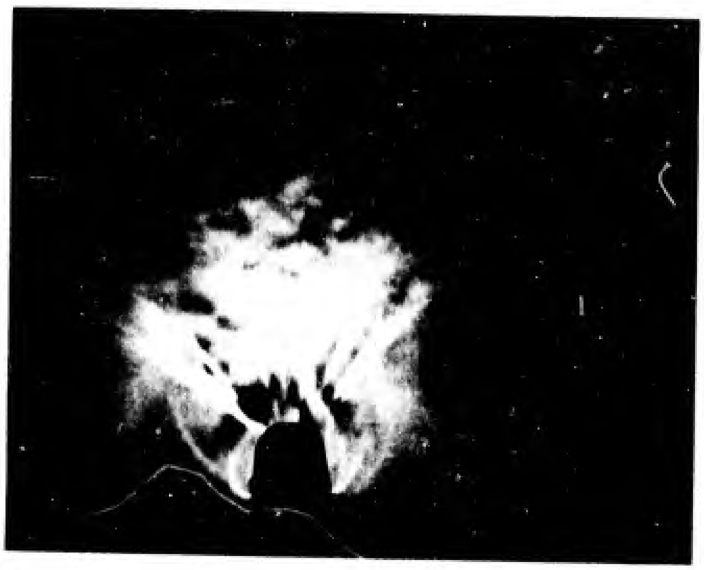

NOSE CAP
$\dot{m} = 2.4 \times 10^{-4}$ lb/sec.

Figure 3-43. Schlieren Photograph, Nose Cap

4. DESIGN APPLICATIONS AND CONCLUSIONS

The basic purpose of this study was to evaluate transpiration cooled materials and concepts for optimum efficiency in a flight environment as they are applied to a nose tip and an air vane leading edge. The results of the laboratory testing have been applied to a design of a nose tip that could be used for an advanced interceptor flight environment. This analysis has shown that the CONAP concept offers a weight savings over a water system. In addition the attempt to minimize the mass flow variation between ideal coolant requirements and actual mass flow resulted in the definition of the best materials and design concept. The Wah Chang and Sylvania porous tungsten (80 percent by volume) materials were selected. These materials, modified by blind holes at the sonic point and vapor deposition on the sidewall, were selected for the design which minimized the flow rate variation.

Several conclusions can be made as a direct result of the data taken. At the coolant mass flow rates expected (5 lb/ft^2-s) for a typical advanced interceptor environment, the internal heat transfer coefficient is on the order of 1000 Btu/ft^3-s-°R. The impact of this result can be seen in Figure 4-1 where the weight of a CONAP system as a function of heat transfer coefficient is compared to that of a water system. For this case the CONAP concept is 50 percent lighter than the water system. Figure 4-1 also shows that the impact of the blind holes on system weights due to the reduction of internal heat transfer coefficient is not great.

The flow characteristics data show that the porous matrices augmented with blind holes can increase the coolant mass flow rate in a local area. The Schlieren photographs of a surrogate coolant showed that blind holes do not starve other surface areas for coolant. The combination of flow characteristics data and heat transfer coefficient data shows that the process of surface vapor deposition decreases coolant mass flow in a local area without affecting the heat transfer coefficient. These modifications to a porous tungsten material can be used to tailor the coolant mass flow distribution through the porous matrix to better meet the mass flow requirement distribution of a nose tip or air vane leading edge. The blind hole technique can be used in the sonic point region of a nose tip or stagnation line region of an air vane leading edge to increase the local mass flow. The vapor deposition technique can be used on the sidewall on both parts to decrease the local mass flow.

With the results that have been experimentally obtained it is now possible to define the best of the available tungsten materials that can be used in flight. A one dimensional analysis was conducted using the results of the flow characteristic and heat transfer coefficient tests to determine the most nearly optimum material and concept. A typical analysis was conducted in the following manner. First, a material with a given permeability and inertial resistance coefficient was selected. This material was then augmented with blind holes where high flow rates were required, and tungsten

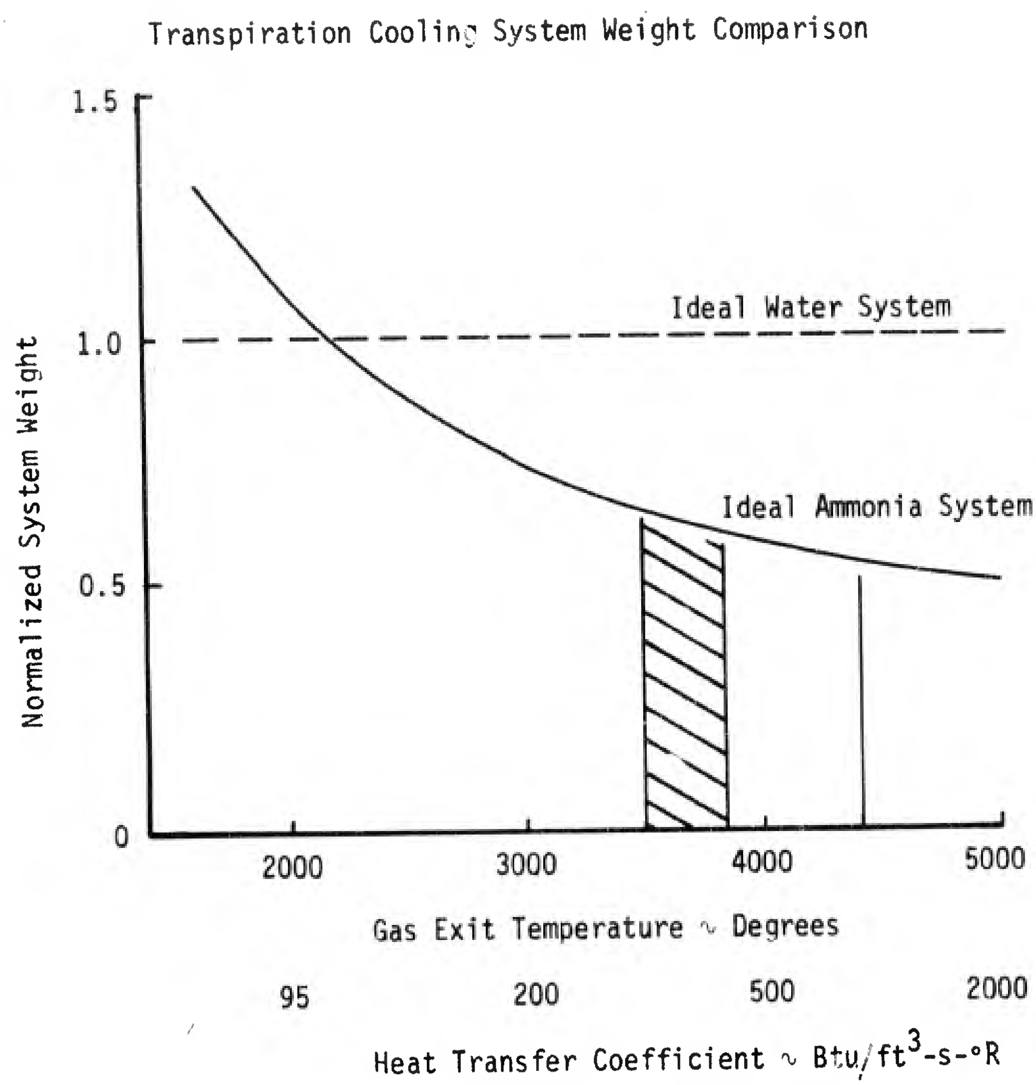

Figure 4-1. System Weight Comparison

vapor was deposited in areas where the flow was greater than desired. A one-dimensional coupled heat transfer and momentum analysis was then conducted to obtain the resultant flow rates and surface temperatures. These flow rates at local areas then were plotted as a function of the non-dimensional distance from the stagnation point. In addition these flow rates can be compared to the ideal flow rate requirements which are a function of the heat transfer to the surface. Figure 4-2 shows the flow rate variation between the ideal coolant flow requirements and the actual coolant flow that will be delivered. Table 4-I summarizes these results. Cases 1, 2, and 3 consider modifications (blind holes and vapor deposition) to those materials that can be readily purchased and processed. Of these the most efficient system is case 3, since the flow rate variation is the lowest. Figure 4-3 shows this conceptual design that was used in the analysis. This design represents the minimum variation comparing actual with desired flow rates that could be theoretically calculated from the available test data for available materials.

Figure 4-4 shows the flow characteristic comparison of all of the porous tungsten materials tested. The figure plots the reciprocal of the permeability versus the inertial resistance coefficient. In this manner, the materials that readily allow flow through them appear in the lower left hand corner of the graph, at low values of the reciprocal of the permeability and low values of the inertial resistance coefficient (β). The materials which are more restrictive to the flow of gases through them appear in the upper right hand corner of the graph. This figure shows how different material flow characteristics can affect efficiency. It can be seen that low efficiency can result with a material that allows too much mass flux for a given pressure drop because the sidewall flow rates will be much greater than required. On the other hand, a material which allows too little flow for a given pressure drop is very efficient but requires very high chamber pressures (>6000 psi) and very thin wall thicknesses (less than 0.1 inch) to deliver the flow. Thus the optimum flow characteristic region for materials is in between these other regions and is shown in Figure 4-4. Two materials tested have flow characteristics which fall into this optimum region; they are the 80 percent Wah Chang and the 80 percent Sylvania materials.

The results of this program show that the CONAP concept does offer potential weight savings over a conventional water system. The next phase of this development would logically be the exposure of the CONAP concept in a plasma arc environment over a range of pressures and enthalpies that are representative of currently anticipated advanced interceptor flight regimes. In the current program a one-dimensional experimental and analytical approach was used to evaluate and select the most nearly optimum materials and concepts. Testing of these materials and concepts in the plasma arc would verify current conclusions as they apply to three dimensional configurations. It is anticipated that the three dimensional model configuratoons should include a discrete hole refractory metal alloy model, a porous tungsten model, a porous tungsten model augmented with blind holes at the sonic point and a porous tungsten model augmented with blind holes at the sonic point and modified with vapor deposition of tungsten material on the sidewall. The plasma arc data obtained for these models would quantitatively yield the mass flow variation between ideal requirements and actual mass flow. This determines the mass flow safety factor requirements for each case. Cross-flow effects, the CONAP concept performance under low and high pressure environments and the general structural integrity of the model are also parameters that can readily be examined in plasma arc testing.

TABLE 4-I

Material Performance Summary
(ATI trajectory at 2.8 seconds)

Case	1			2			3			4			5		
Material	58 Percent Mallory ''C''			70 Percent Wah Chang			80 Percent Wah Chang			85 Percent Dense			ρ > 85 Percent		
Location on nose tip	Stag.	Sonic	Sidewall	Stag.	Sonic	Sidewall	Stag.	Sonic	Sidewall	Stag.	Sonic	Sidewall	Stag.	Sonic	Sidewall
Modifications	None	20 micron coating		20 microns coating	None	20 microns coating	None	0.19 inch deep blind holes	20 microns coating	None	0.06 inches deep blind holes	20 microns coating	None		
Local mass flow lb/ft^2 sec	2	10	12	3	7	7	2	7.5	4	2	8	3	2	8	0.3
Wall temperature °R	5200	5000	560	3000	5300	560	5100	4700	560	5000	5000	560	5000		
Coolant upstream pressure ~lb/in.^{2}	2640			2900			3300			4700			6000		
Local downstream pressure ~lb/in.^{2}	2620	1440	64	2620	1440	64	2620	1440	64	2620	1440	64	2620	1440	64
Local wall thickness ~in.	0.25	0.35	0.45	0.30	0.35	0.45	0.25	0.35	0.45	0.25	0.09	0.45	0.02	0.005	0.45

Comments

Case 1 and 2 Material too porous, sidewall over blowing excessive.
Case 3 Material available and performance better than cases 1 and 2.
Case 4 Sonic wall thickness is too small.
Case 5 Supply pressure requirements too high and wall thickness too small at stagnation and sonic points.

Note that blind holes and plating do not have significant effect on flow in cases 4 and 5.

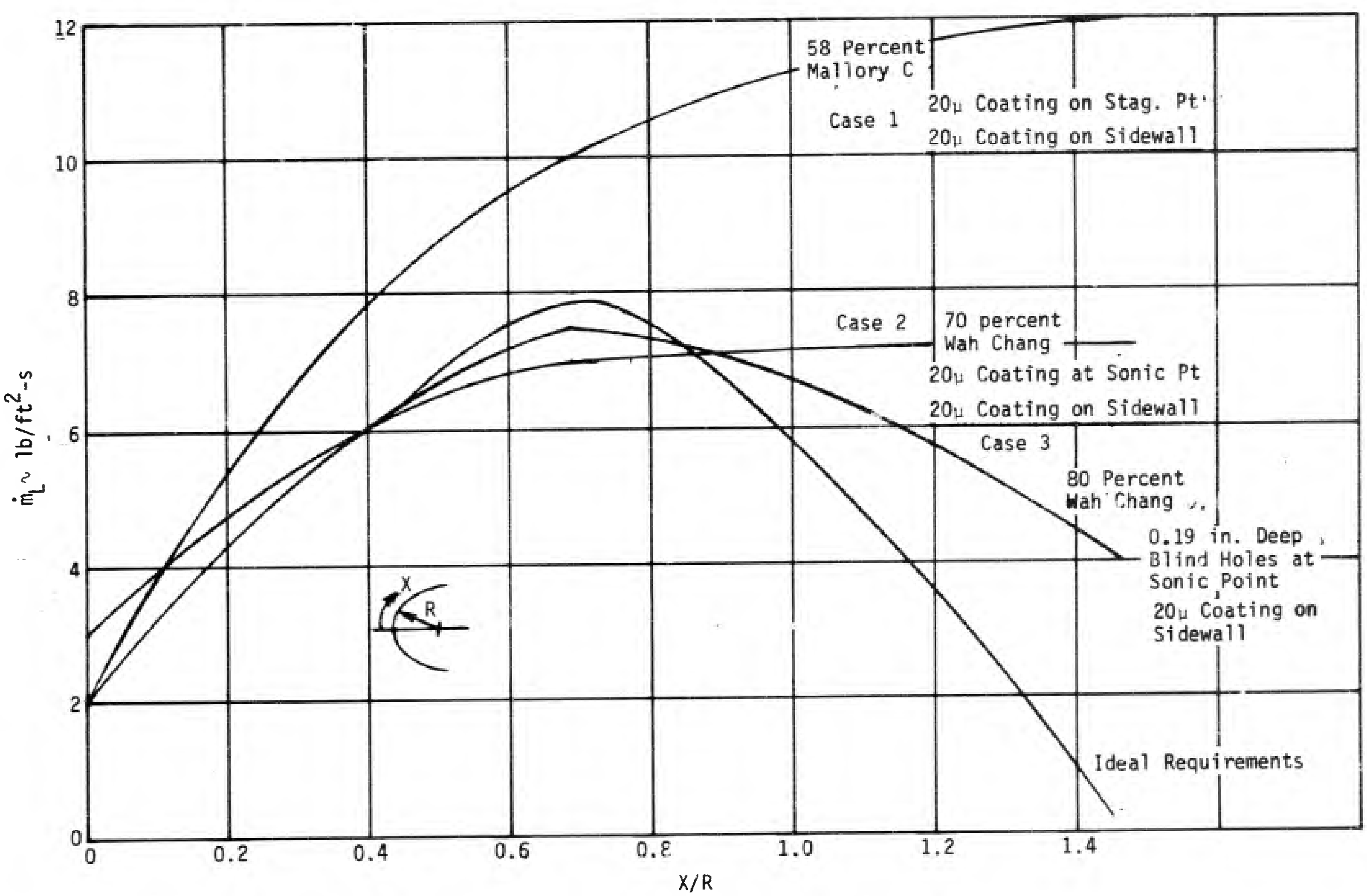

Figure 4-2. Local Ammonia Flow for Three Modified Porous Tungsten Nose Tips at Max ATI Heating

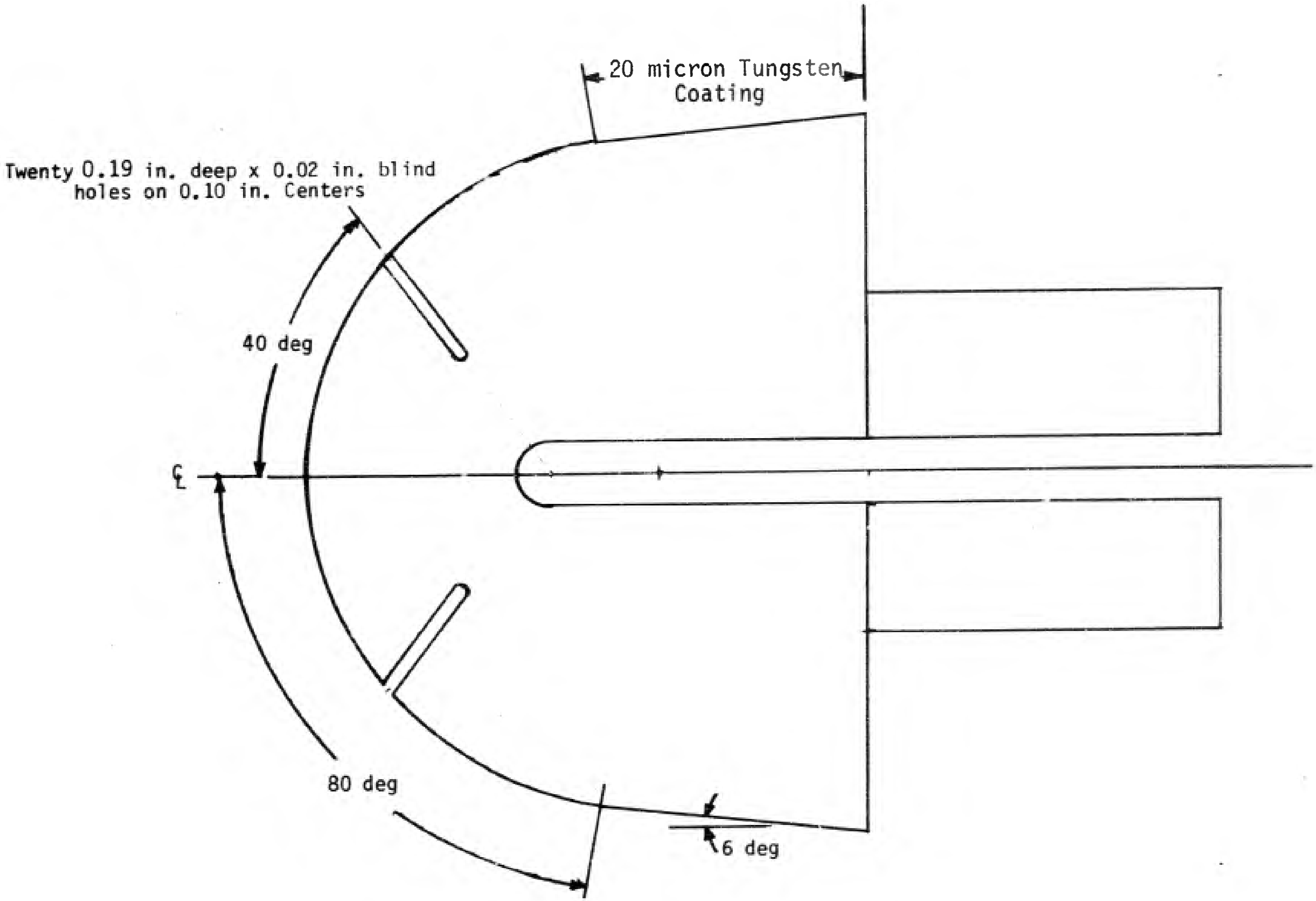

Figure 4-3. Nose Tip Design Used in Analysis

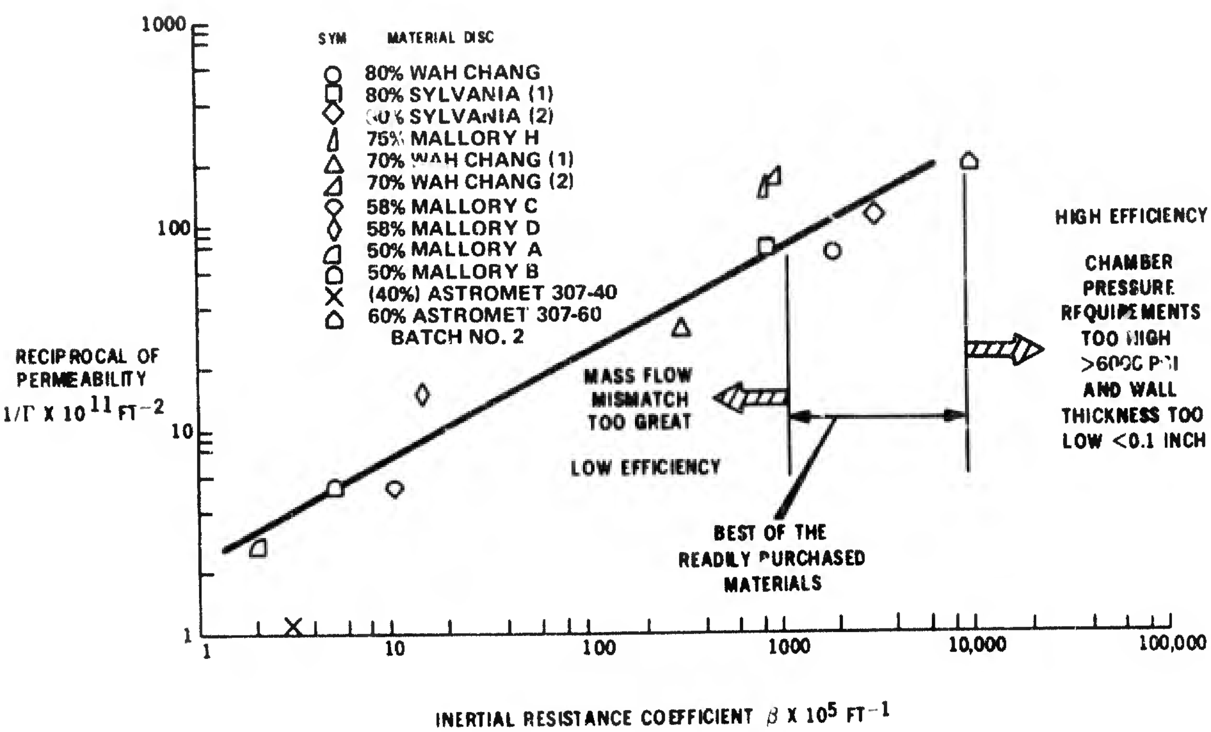

Figure 4-4. Flow Characteristic Correlation for Several Porous Tungsten Materials

APPENDIX A

FLOW CHARACTERISTICS TESTS

A.1 Flow Characteristics Tests

At the high coolant flow rates of interest in this study, a modification of Darcy's law is necessary to predict pressure drop through the porous tungsten specimen.

Darcy's law states that

$$\frac{dP}{dX} = \frac{\dot{m}\mu}{\Gamma\rho} \tag{1}$$

where:

$\frac{dP}{dX}$ = pressure drop across the thickness

$\dot{m}$ = mass flow rate
μ = viscosity
ρ = density.

For high flow rates another term must be added to Equation (1) to account for turbulence in the flow. This relation is shown in Equation (2).

$$\frac{dP}{dX} = \frac{\dot{m}\mu}{\Gamma\rho} + \beta\rho\left(\frac{\dot{m}}{\rho}\right)^2 \tag{2}$$

where:

Γ = the permeability
β = the inertial resistance coefficient of the particular specimen.

Determination of both Γ and β must be made by empirical techniques.

Assuming the test coolant to be a gas, we may substitute the perfect gas relation for ρ

$$\frac{dP}{dX} = \frac{\dot{m}\mu}{\Gamma}\left(\frac{ZRT}{P}\right) + \beta\dot{m}^2\left(\frac{ZRT}{P}\right) \tag{3}$$

Since the porous tungsten specimen will not be heated during the evaluation of Γ and β, T and μ are constants. Integrating (3) and solving for the pressure across the specimen

$$\frac{P^2 - P_o^{\,2}}{2} = \dot{m}ZRTX\left(\frac{\mu}{\Gamma}\right) + \dot{m}ZRTX\ \ \beta\dot{m} \tag{4}$$

Rewriting (5-4), there follows

$$\frac{P^2 - P_o^2}{2\mu\dot{m}ZRTX} = \left(\frac{1}{\Gamma}\right) + \left(\frac{\beta\dot{m}}{\mu}\right) \tag{5}$$

Since all values shown in Equation (5) may be measured at each test point, with the exception of Γ and β, we may plot $(P^2 - P_o^2)/2\ \dot{m}ZRTX\mu$ (ordinate) versus $\dot{m}/\mu$ (abscissa). Next a straight line may be fitted to the available data points. The straight line intercept at the ordinate axis is equal to $1/\Gamma$; β is the slope of the straight line.

A similar method is employed to determine Γ and β if a liquid test coolant is used. In this case, however, the parameters can be simplified and a $\rho(P-P_o)/\mu\dot{m}X$ is the ordinate and $\dot{m}/\mu$ is the abscissa.

A Fortran IV computer program was written to determine Γ and β employing these relations. The Fortran IV listing is shown in Appendix D.

To simultaneously measure the quantities required to obtain Γ and β for flow through several specimens, a test fixture was built. A schematic diagram of the test fixture is shown in Figure A-1. The test fixture is designed so that the back pressure on each of the six porous tungsten specimens may be controlled by means of needle valves 1 through 6. Since the upstream pressure on all six specimens is equal, each pressure drop may be set. An additional circuit is also available on each of the six specimens so that individual flow rates and discharge pressures may be measured. For example, if the coolant flow rate and specimen discharge pressure through circuit 4 is to be measured, gate valves 4A and 4C are opened and 4B is closed. This will force the coolant to pass through the metering venturi upstream of needle valve 4. During fabrication of the test fixture, care was taken to equalize the two circuits' flow pressure drops. The flow metering venturi is designed so that most of the pressure drop at the throat is recovered in its diffuser section.

The test fixture fabricated for these tests is shown in Figures A-2 and A-3. To measure the required test parameters it was necessary to include as part of the apparatus a mass flow measuring device and pressure measuring equipment. The following paragraphs briefly describe the techniques employed for measuring mass flow through the porous tungsten plugs.

The N_2 supply was filtered down to 0.3 micron to prevent clogging of the pores in the tungsten specimens. Supply pressure levels were based on predictions of expected hot wall pressure drops across 0.25 and 0.50 inch porous walls with flow characteristics exhibited by the specimens received, and a downstream pressure of 6 atm. The resulting range of pressures varied from 400 to 800 psig and three upstream pressures were selected for testing: 400, 600, and 800 psig. Since flow tests were to be performed with a cold gas, a lower pressure drop results due to viscosity effects.

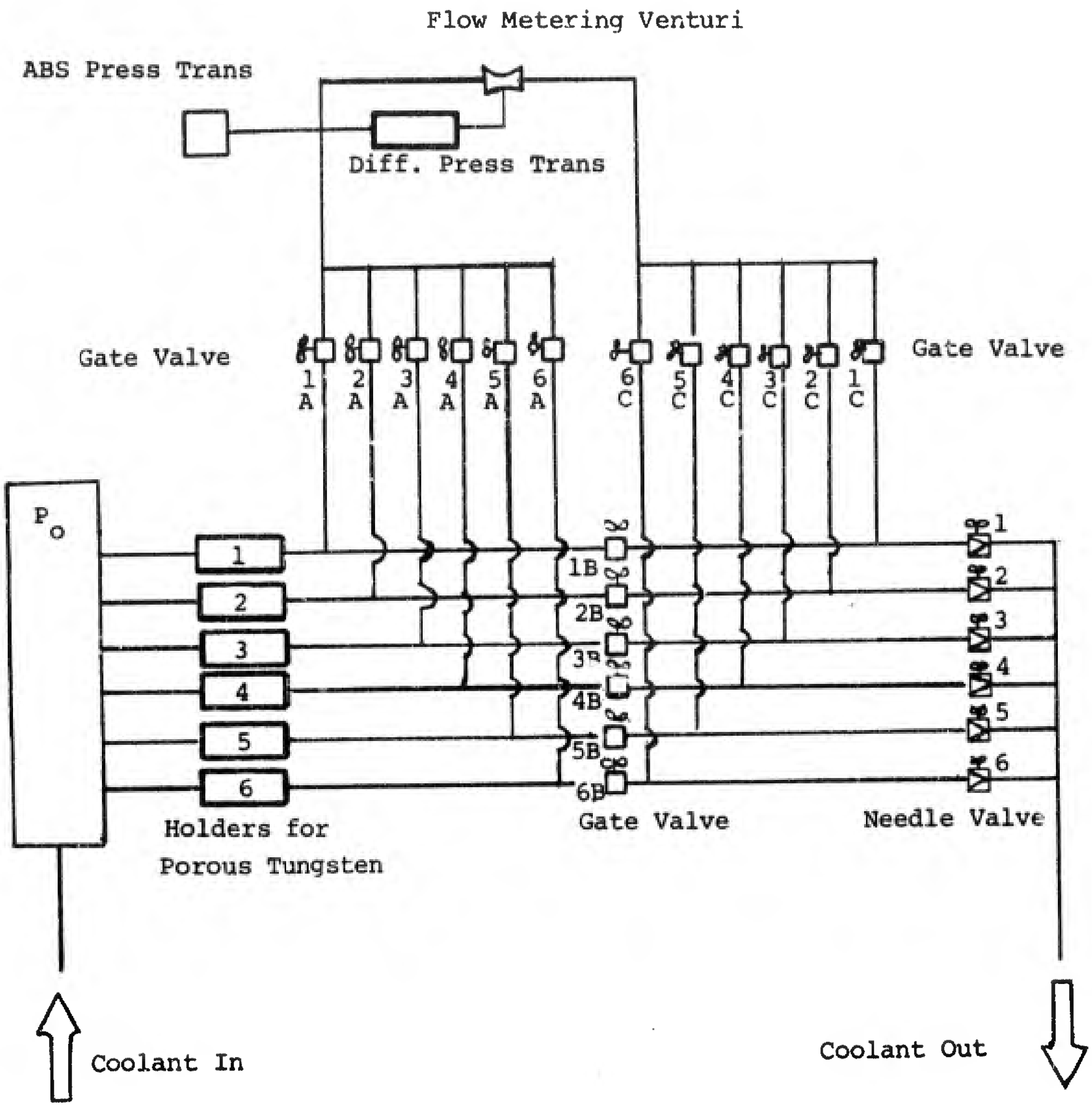

Figure A-1. Flow Characteristics Test Fixture

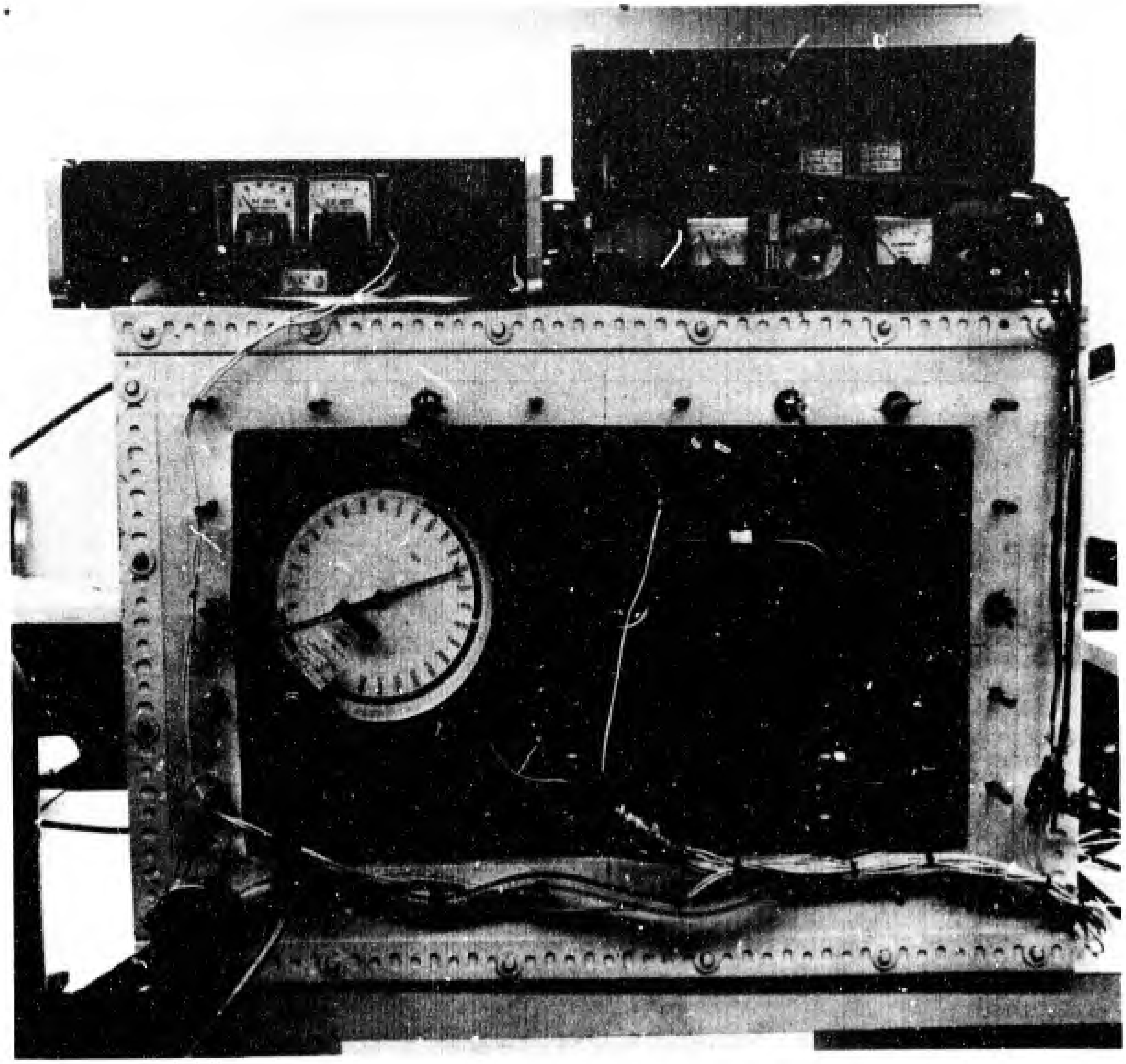

Figure A-2. Flow Characteristics Test Fixture and Instrumentation

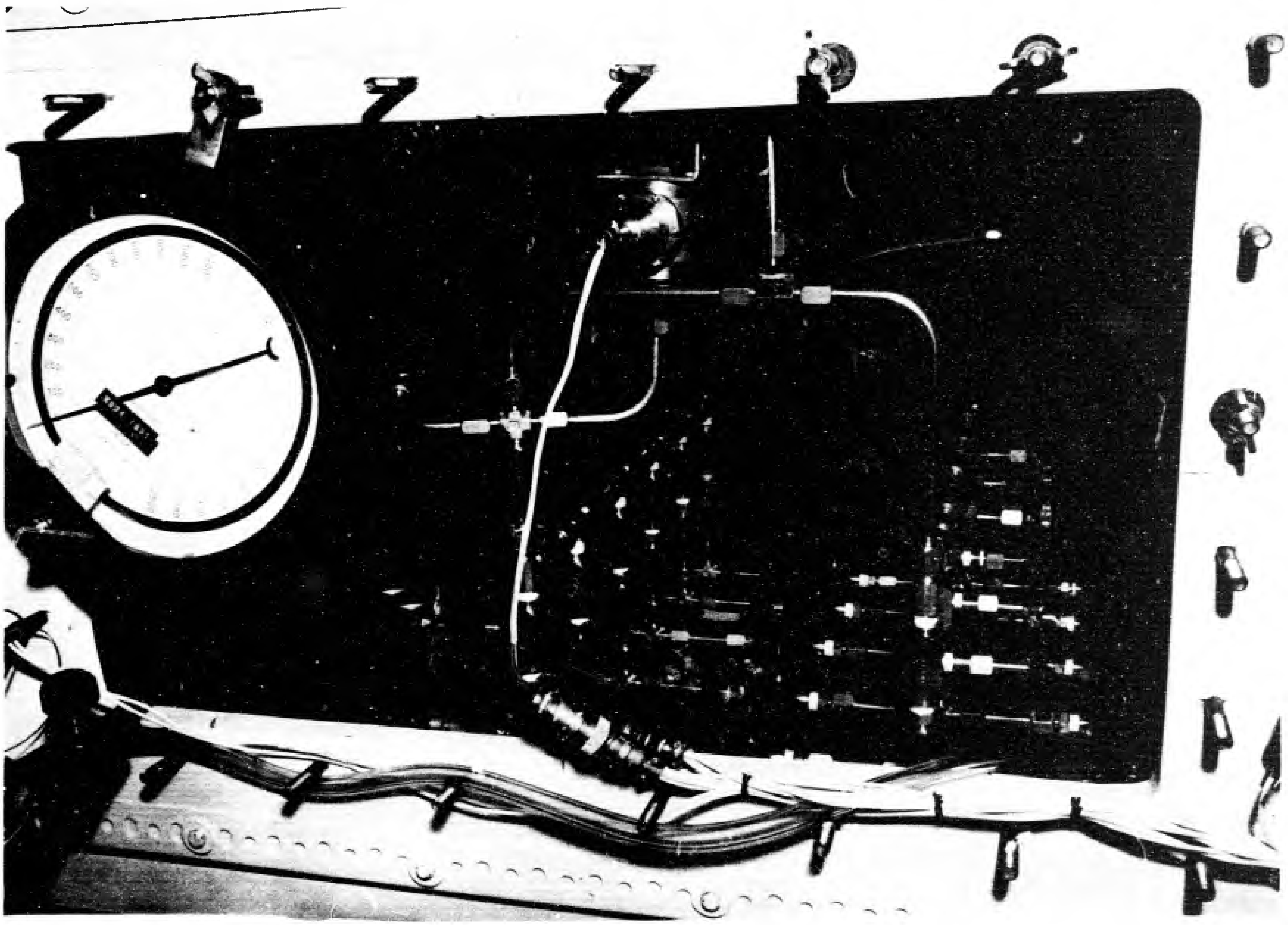

Figure A-5. Flow Characteristics Test Fixture

The schematic shown in Figure A-1 should be referenced for the identity of the various valves discussed in the detailed test procedure below.

The cold flow test procedure is as follows:

1. Install a porous tungsten specimen of the type shown in Figure A-1 of each of the six holders.
2. Set supply manifold pressure to 400 psig;
3. Slowly open valves 1A then 1C;
4. Open needle valve 1 until pressure downstream of the porous plug is 360 psig;
5. Open valve 1B and close 1A and 1C;
6. Open valve 6A then 6C;
7. Open needle valve 6 to the fully opened position;
8. Based on the downstream pressure reading in circuit 6, compute desired downstream pressure for circuits 2, 3, 4, and 5 by determining a uniform pressure spread for each of the four circuits;
9. Open valve 6B and close 6A and 6C;
10. Open valve 2A then 2C;
11. Adjust needle valve 2 until the desired downstream pressure computed in step 7 is achieved;
12. Open valve 2B and close 2A and 2C;
13. Repeat steps 10 through 12 for each of the remaining circuits 3, 4, and 5.

During each test, some readjustment of manifold pressure was required to maintain the desired pressure of 400 psig. Once the downstream pressure was achieved on each of the six circuits, the data was recorded. This procedure was repeated for the 600 psig and 800 psig manifold pressure levels. The same procedure was used for the variable thickness and permeability tests.

To ensure that gas leakage by the specimens did not occur in the holders, a solid specimen was installed in each holder and the system pressure upstream of the disc increased to approximately 1500 psi. The nitrogen supply was then shut off from the test apparatus and leakage deduced from the pressure bleed down. Holder modifications were made until there was no decay in the pressure level.

To determine the characteristics of the porous tungsten specimens it was necessary to determine mass flow rate, pressure drop across the specimens, flow area, nitrogen temperature, and specimen thickness. These data were determined as described below.

Porous tungsten upstream pressure was determined employing the Heise gage shown in Figure A-2. Downstream pressure was measured by a 0 to 1000 psi pressure transducer in conjunction with a digital millivolt meter shown in Figure A-3. The transducer output was also recorded on a millivolt recorder. Transducer calibration curves are shown in Figure A-4 and A-5.

Nitrogen mass flow rate was determined by either of two calibrated venturies. For purposes of these tests each of the venturies was calibrated using nitrogen and employing flow meters of known accuracy. Differential pressure across the venturies was measured with either of two differential pressure transducers depending on the flow rate expected.

Calibration curves for these transducers are shown in Figure A-6 and A-7. Mass flow was computed by determining theoretical flow as a function of Mach number, calculating ideal Reynolds number based on the throat diameter of the venturi, finding flow coefficient (C_F) for the specific venturi from Figure A-8, and finally calculating flow as the product of C_F and the theoretical mass flow. Note that the value of C_F for the large venturi in Figure A-8 is greater than one. This behavior is caused by the slightly elliptical cross section of the throat on this venturi. Since the throat diameter is determined by measurement with a pen gage, the resultant area computed is less than the true area. This results in a low theoretical flow rate thereby making the C_F correction greater than one.

A.2 Heat Transfer Coefficient Tests

The internal heat transfer coefficient tests were conducted using ammonia as the coolant. The overall test schematic diagram is shown in Figure A-9. Coolant is supplied from the coolant supply system to the test fixture. Upon passing through the hot porous plug the coolant vents into the fume hood where it mixes with a purge supply of nitrogen. From the fume hood the gaseous mixture is passed through a water tank where the ammonia is absorbed by the water and flushed.

A schematic of the test fixture in which the hot porous plug is heated and through which the coolant passes is shown in Figure A-10. Coolant was supplied through a flexible hose, passed through a quartz phenolic tube, and into the boron nitride specimen holder. The boron nitride specimen holder is capable of withstanding the 5000°R tungsten temperature and at the same time is not electrically coupled to the RF heater.

The boron nitride specimen holder is attached to the quartz phenolic inlet tube by means of threaded quartz phenolic retainer rings. The system has an ''O'' ring and grafoil washers to prevent leakage. Figure A-11 shows the detailed drawings of the test fixture hardware. Figure A-12 shows the actual hardware as assembled and in an exploded view. Figure A-13 shows the

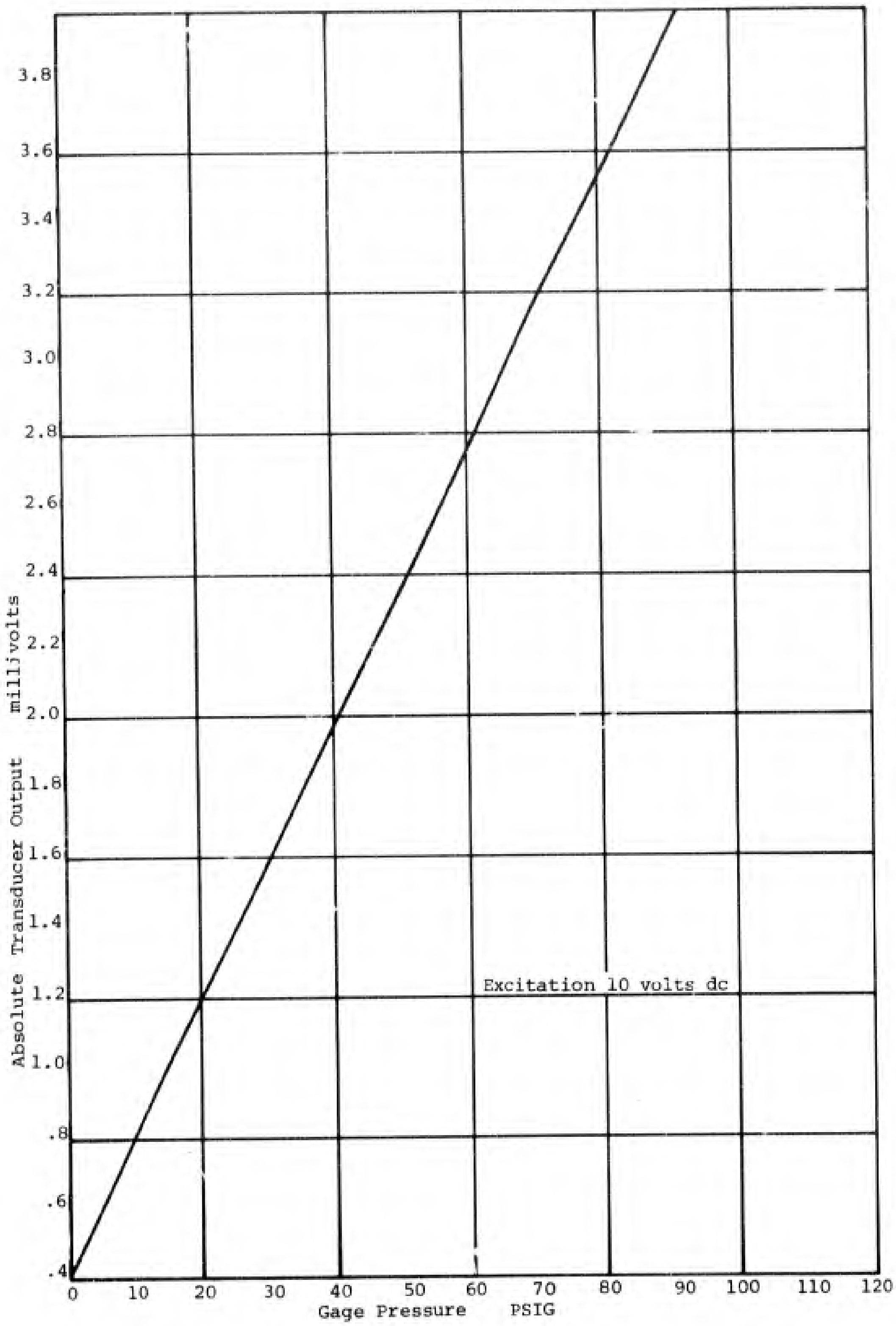

Figure A-4. Downstream Pressure Transducer Calibration Curve

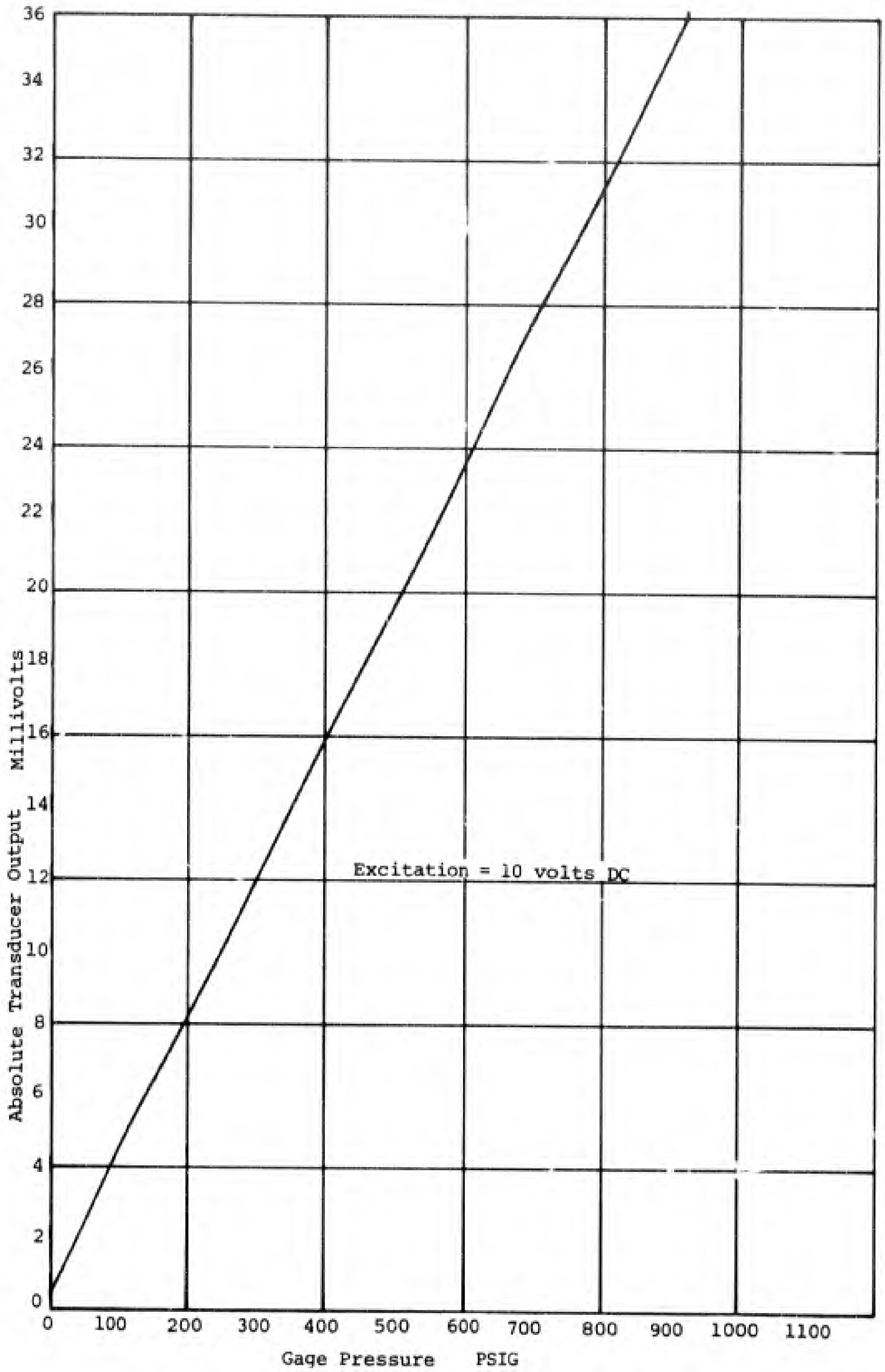

Figure A-5. Downstream Pressure Transducer Calibration Curve

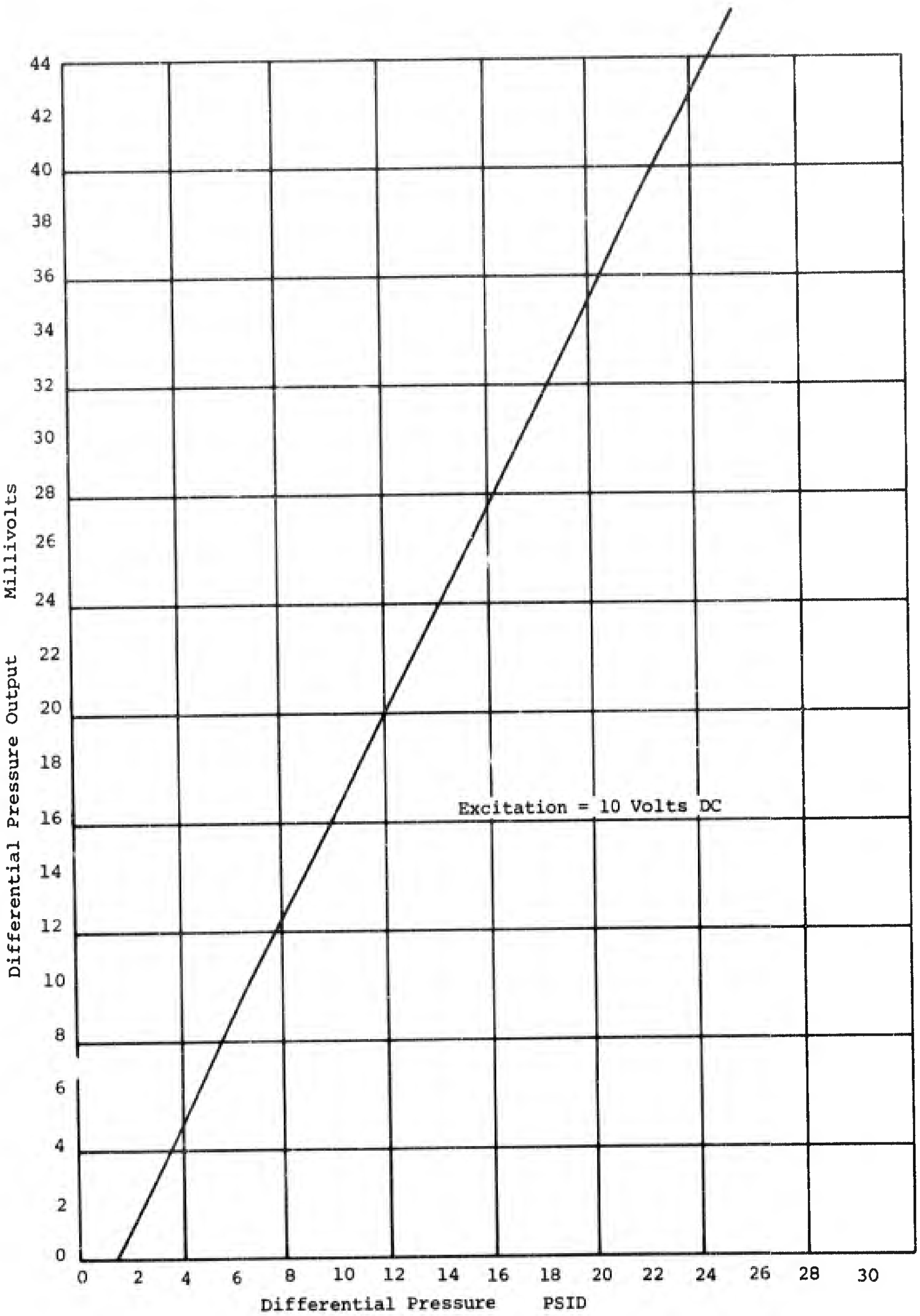

Figure A-6. Differential Pressure Transducer Calibration

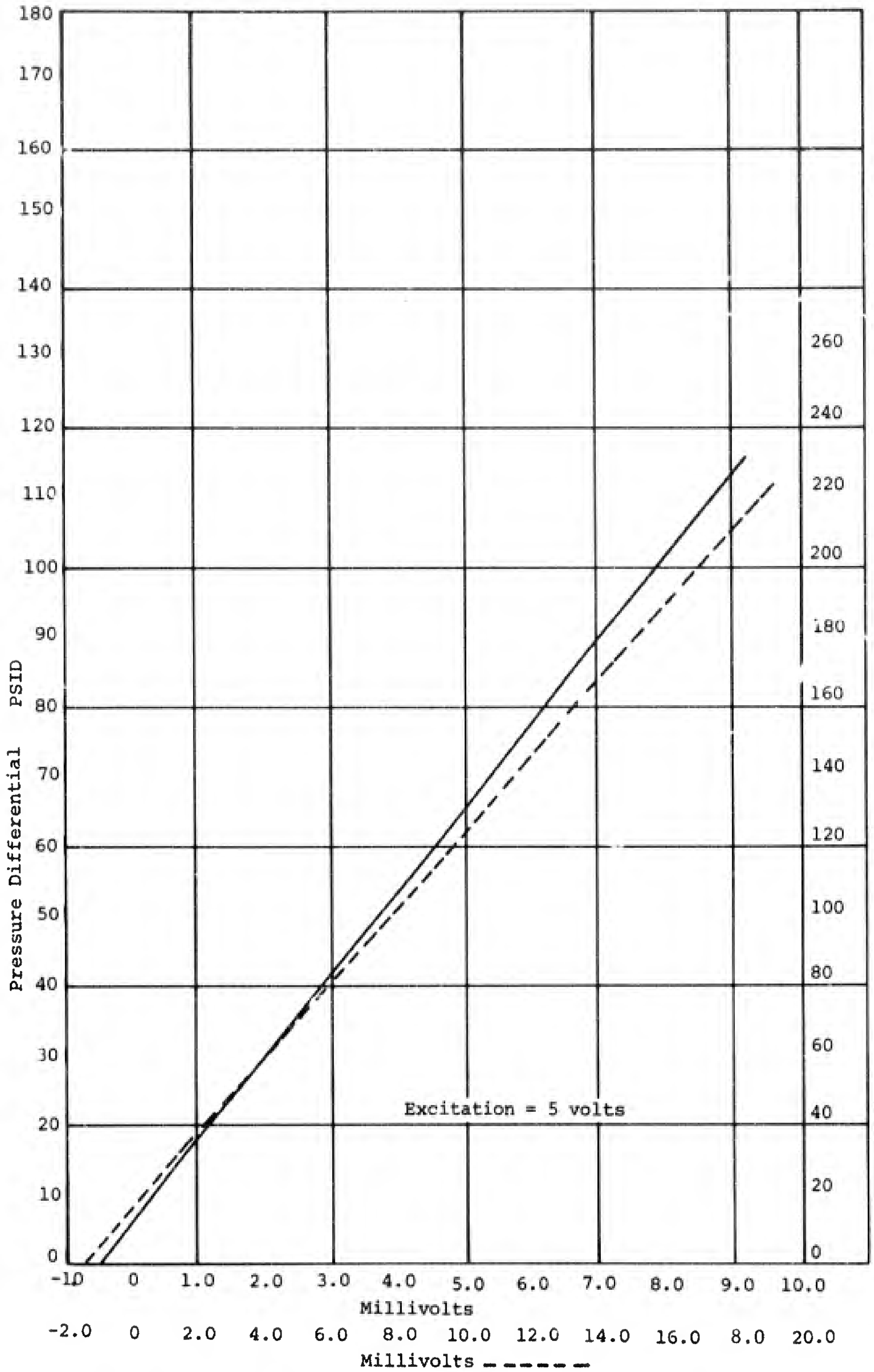

Figure A-7. Differential Pressure Transducer Calibration (High Range)

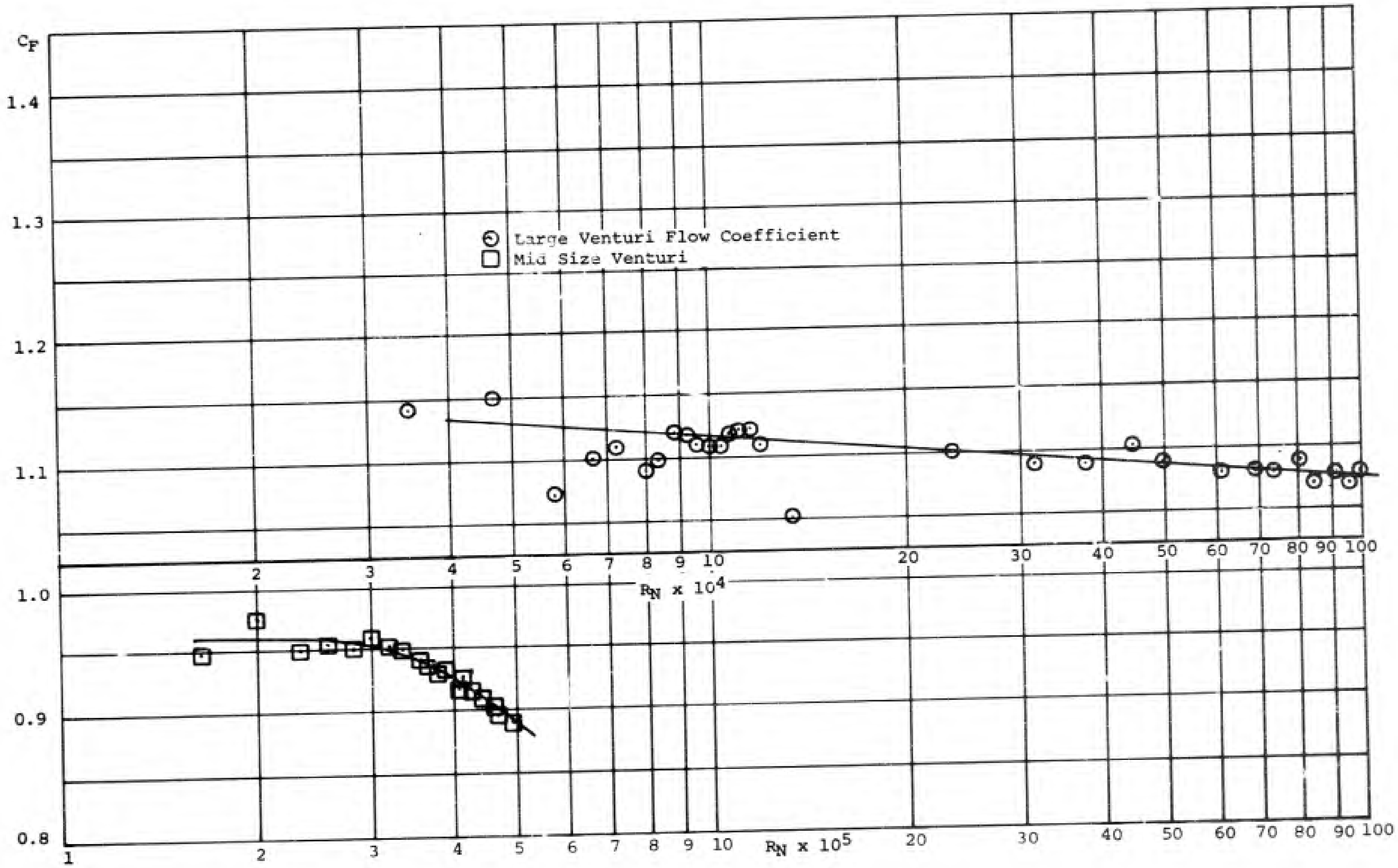

Figure A-8. Venturi Flow Coefficient Curves

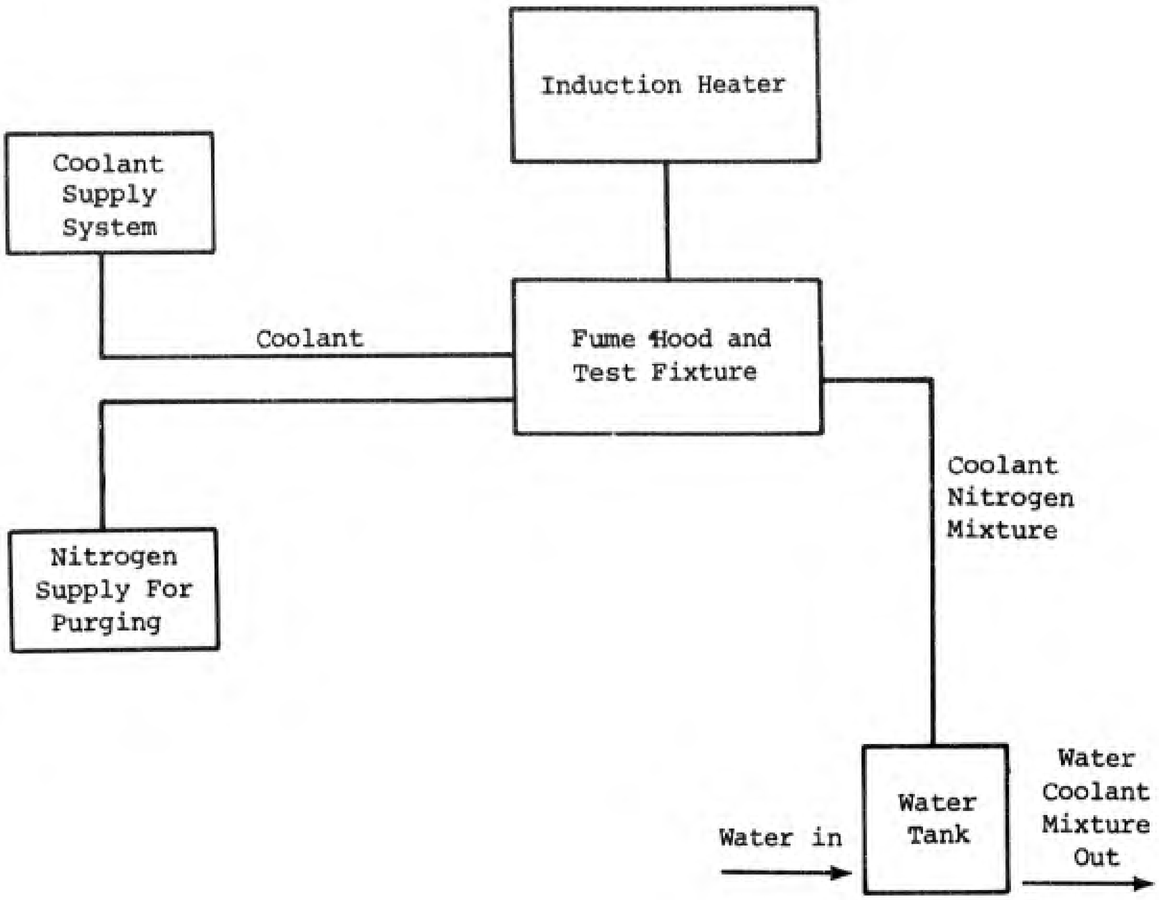

Figure A-9. Heat Transfer Coefficient Test Schematic Diagram

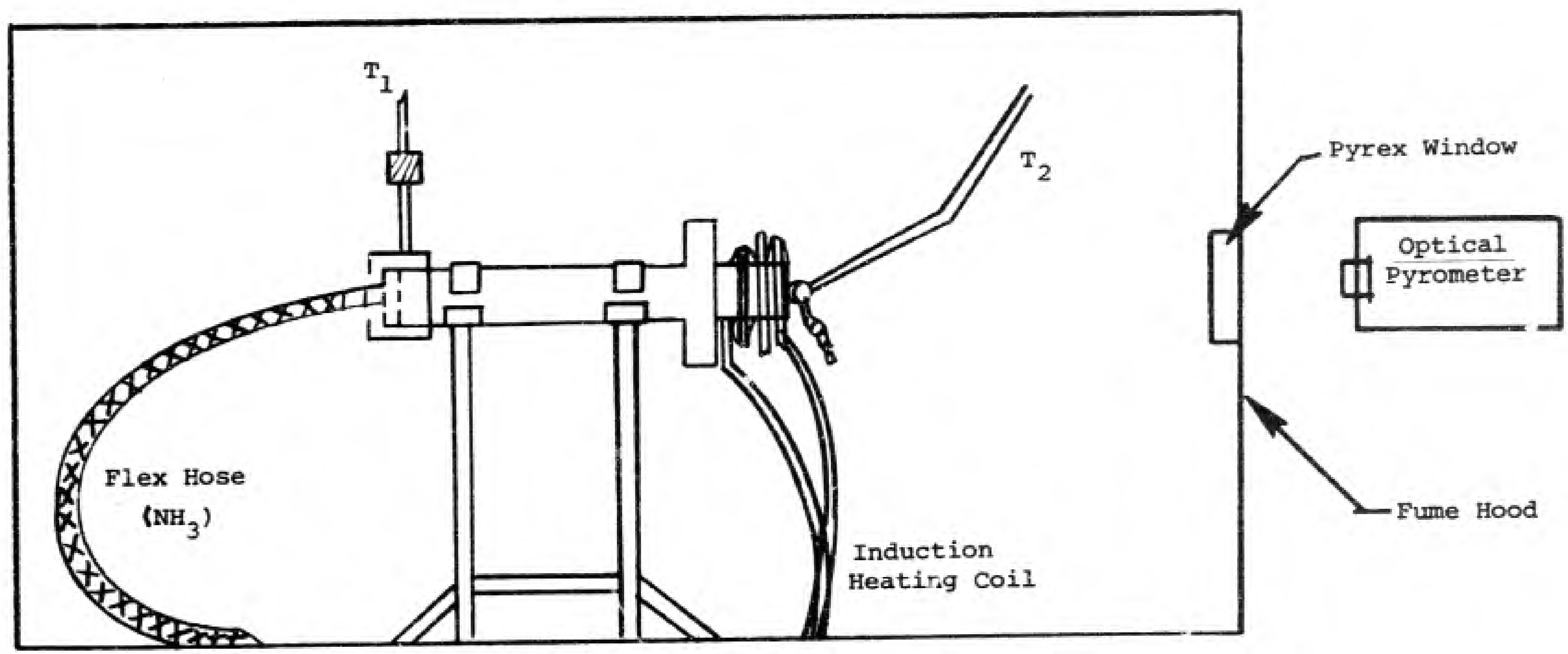

Figure A-10. Heat Transfer Coefficient Test Schematic

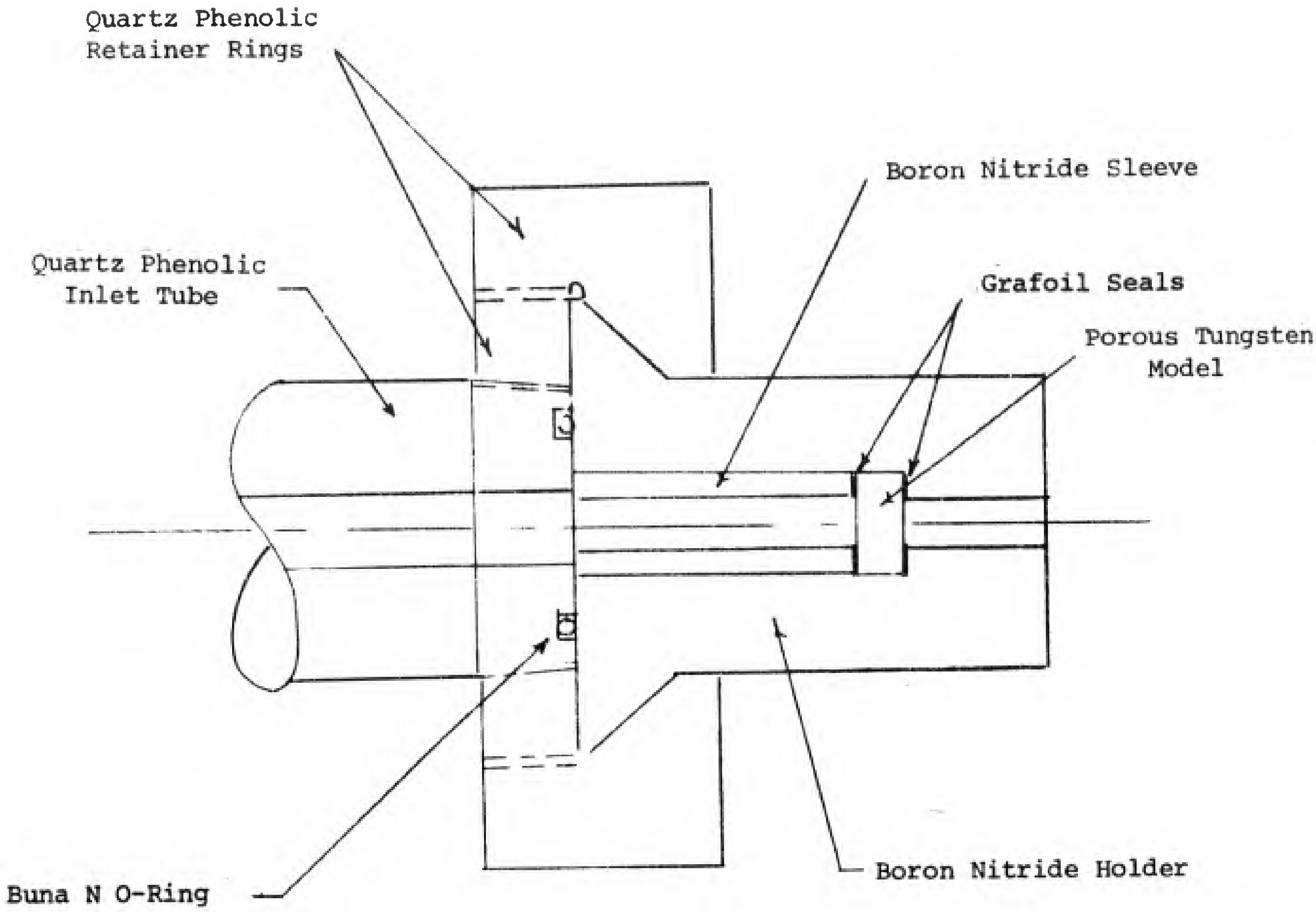

Figure A-11A. Heat Transfer Coefficient Test Fixture Assembly Drawing

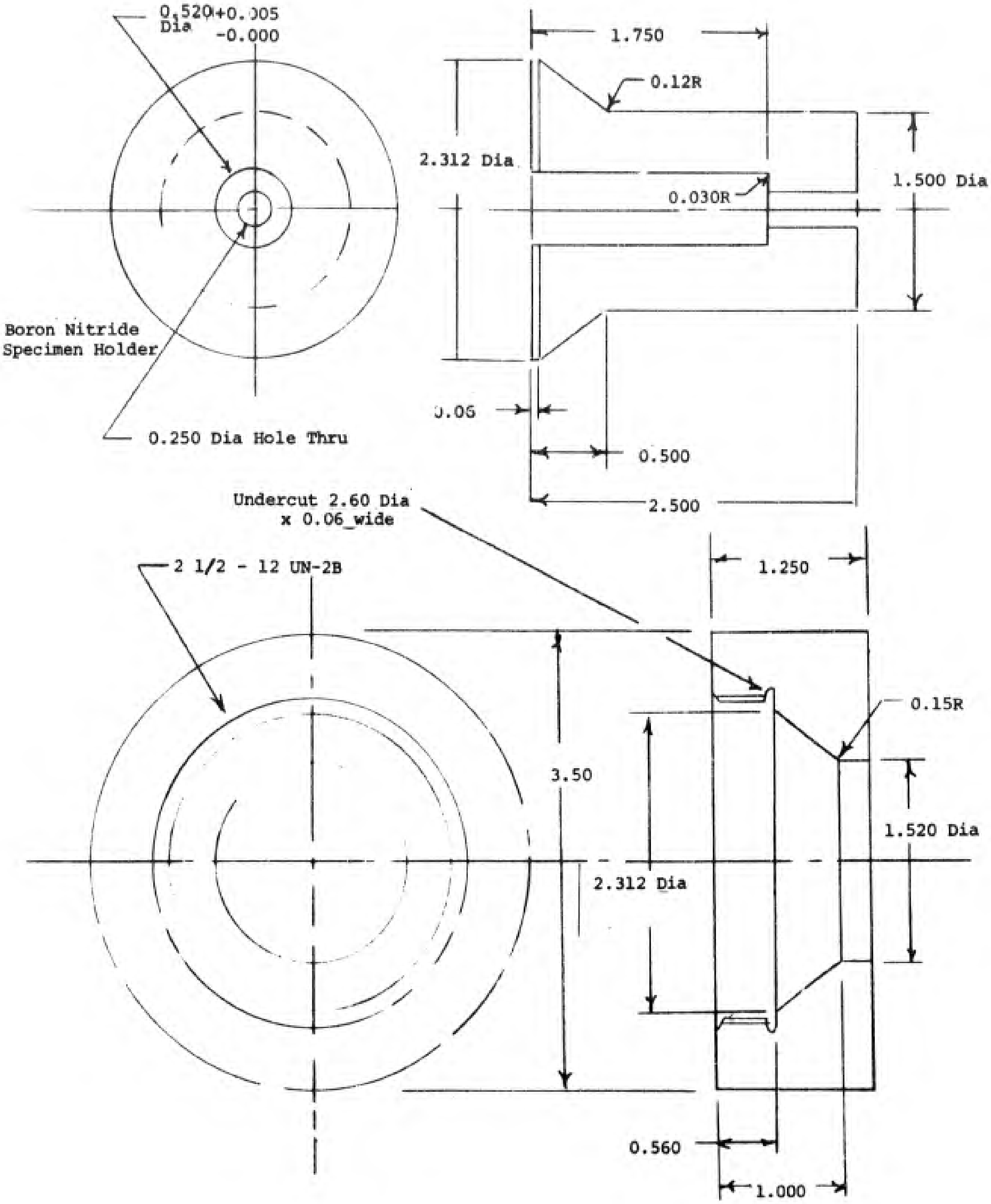

Figure A-11B. Quartz Phenolic Retainer Ring

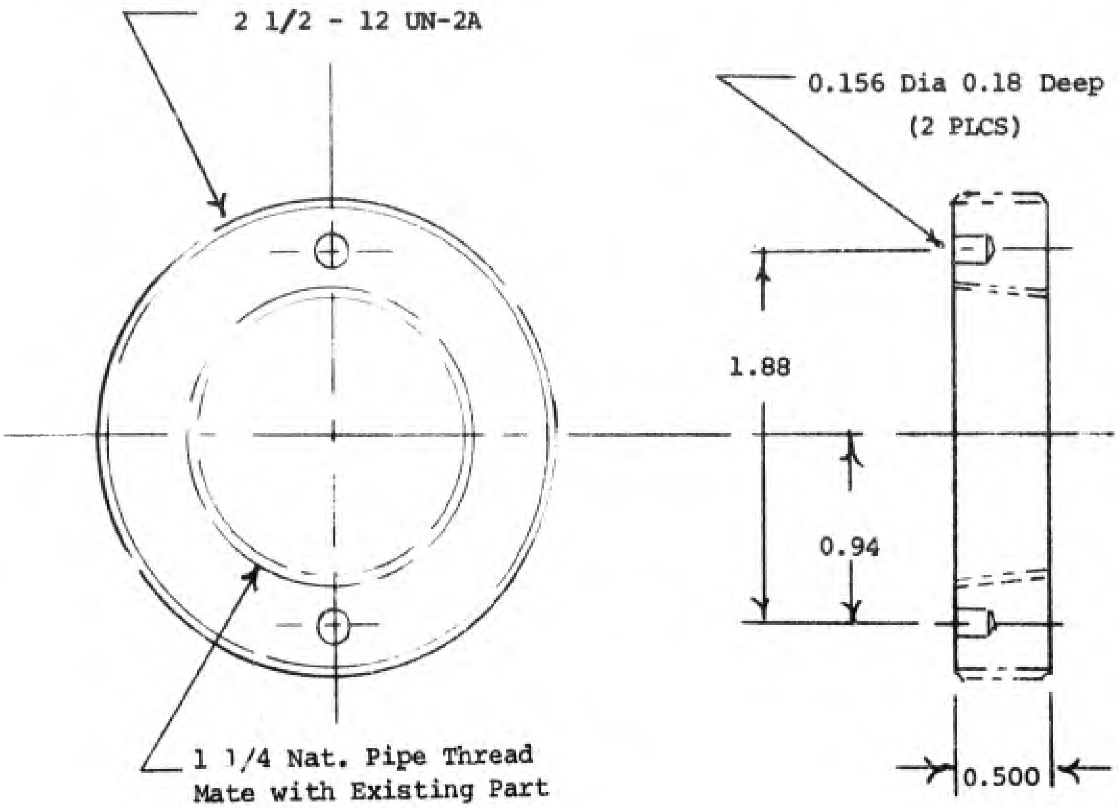

Quartz Phenolic Retainer Ring

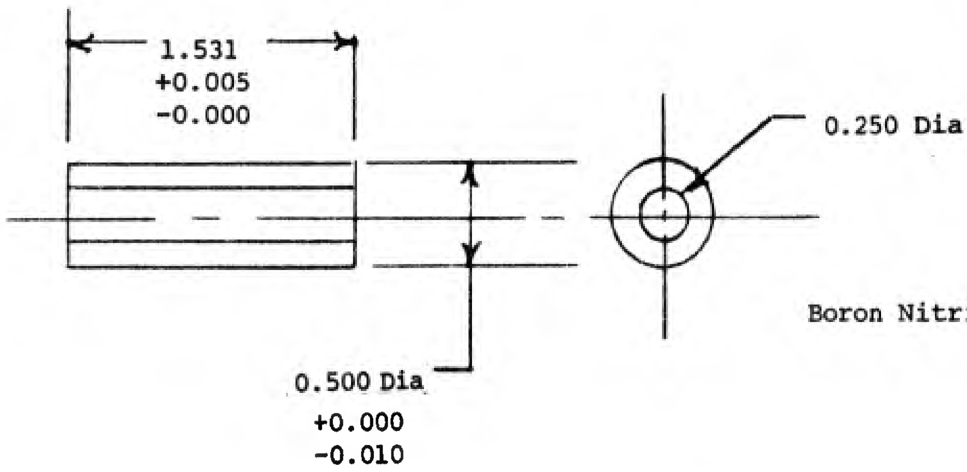

Boron Nitride Sleeve

Figure A-11C. Boron Nitride Spacer

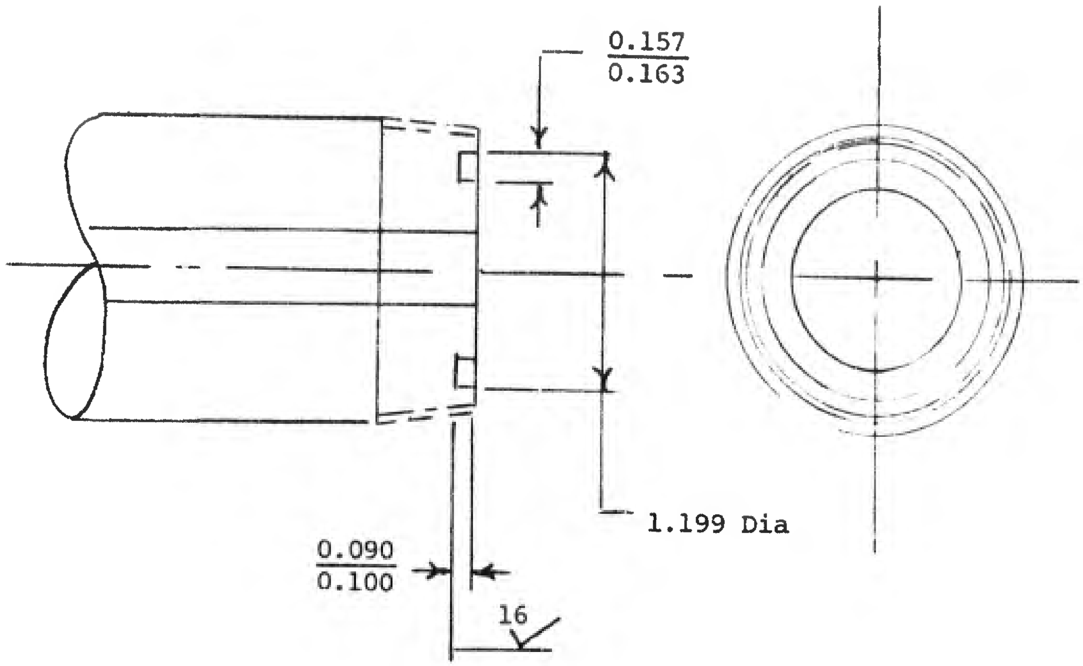

Machine Groove for -213 O-Ring

Figure A-11D. Quartz Phenolic Inlet Tube

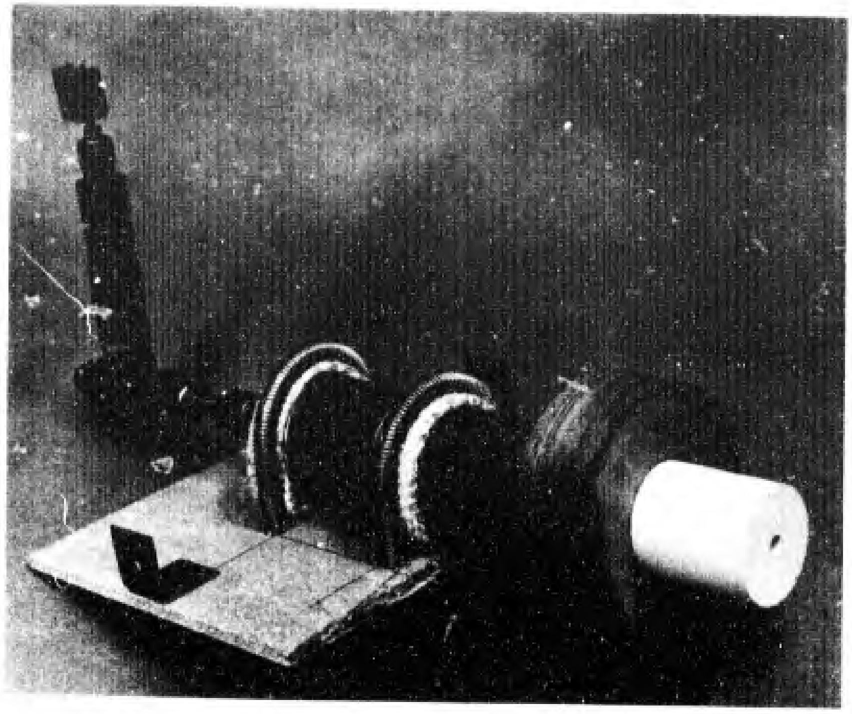

Figure A-12A. Heat Transfer Coefficient Test Assembly (Assembled View)

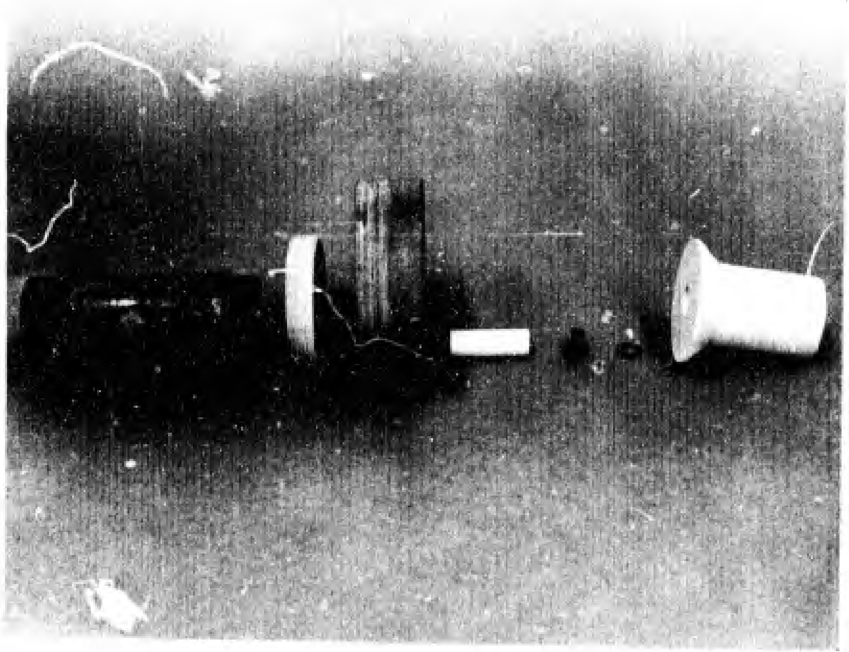

Figure A-12B. Heat Transfer Coefficient Test Assembly (Exploded View)

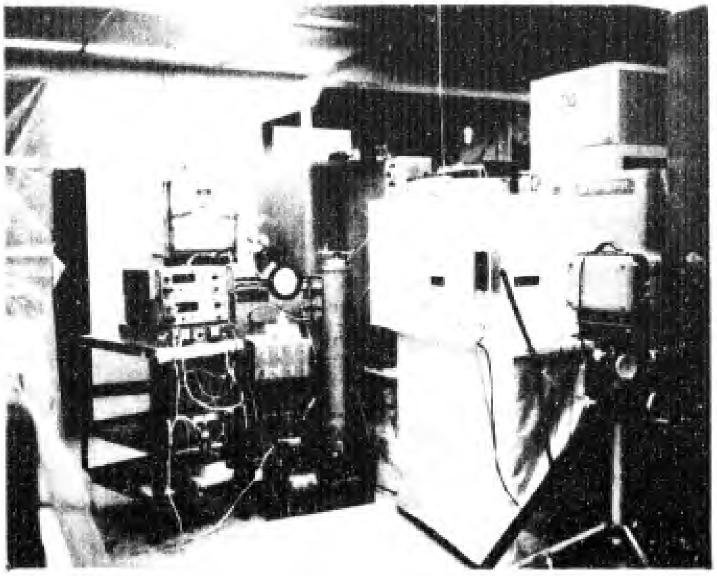

Figure A-13A. Laboratory Placement of the Components of the Heat Transfer Coefficient Tests

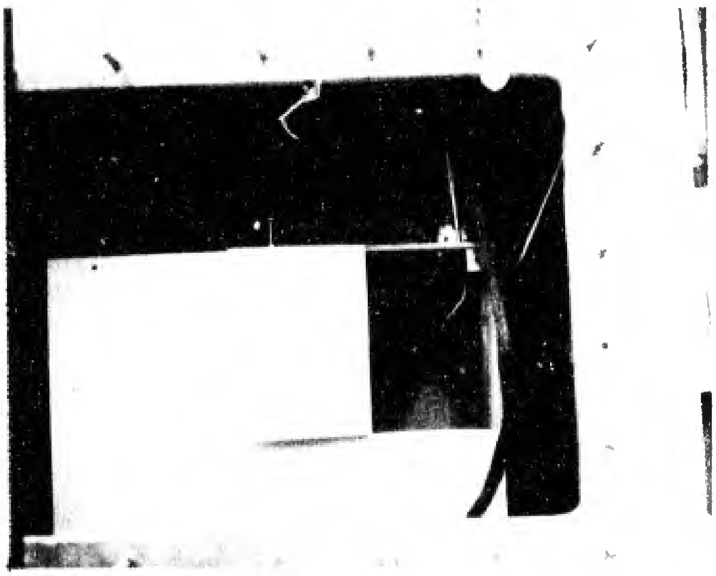

Figure A-13B. Heat Transfer Coefficient Test Assembly Housing

laboratory placement of the components of the heat transfer coefficient tests. These components include the induction heater, optical pyrometer, coolant supply system, and the millivolt and chart recorders. Figure A-13B shows the placement of the heat transfer coefficient test assembly inside the heater coils. The assembly was housed in a transite box which is inside the fume hood. Also seen in Figure A-13B is the thermocouple mechanism used to insert the thermocouple into the exit of the boron nitride holder.

Thermocouples were employed to measure coolant inlet and exit temperatures. An optical pyrometer, as shown in Figure A-10, was used to measure tungsten temperature at the exit. Coolant A-10 flow rate and inlet pressure level were determined employing the calibrated venturi and the pressure transducers that are part of the coolant expulsion system. Three flow measuring venturies were used for flow measurement. Tabel A-I indicates the various venturies and differential pressure levels expected during the tests. Once the test data discussed above has been obtained, the internal heat transfer rate between the coolant can be determined employing the analytical technique explained in Appendix C. The porous tungsten's permeability (Γ) and inertial resistance coefficient (β) determine the upstream pressure necessary to force the desired coolant flow through the porous tungsten. This analytical technique has been modified slightly so that cold flow pressure drop and alternatively Γ and β may be determined if pressure drop is known.

TABLE A-I

Flow Venturi Selection

Coolant Flow Rate (lb/ft^2-s)	0.5	1	2	5	8
Venturi req for NH_3	Small	Small	Small	Med	Med
Differential pressure (psid)	0.2	0.5	26	18	40
Venturi req for N_2	Small	Med	Med	Large	Large
Differential pressure (psid)	13	7	22	1	2

In order that an accurate assessment of the value of the internal heat transfer coefficient, h', could be made, emphasis was placed on the prevention of coolant leakage past the holder-specimen interface. To assess the leakage past the grafoil seals placed on each side of the specimen, both cold flow and hot flow tests were run. A solid tantalum disk was fabricated and used in the tests. The test procedure consisted of assembling the holder using the solid tantalum disk and pressurizing the system and holder upstream of the disk to approximately 1000 psia. A gate valve just upstream of the holder was closed and a pressure gage attached at the holder was monitored. No decrease in pressure was observed during the 15 minute test duration. Next, the RF generator was energized and the tantalum disk heated to approximately 5000°F and the pressure inside the holder was again observed for approximately 15 minutes. No pressure drop resulted.

In order to measure coolant discharge temperature, a traversing, radiation-shielded thermocouple was fabricated and installed. This thermocouple was platinum, platinum – 13 percent rhodium, capable of measuring temperatures to 3100°F. The influence of both the RF field used for specimen heating and the porous specimen radiation effects on the thermocouple's measurement of coolant discharge temperature were examined.

Since the thermocouple itself is metal, it can couple to the RF field and be heated inductively. In addition, the high field voltage could also influence the thermocouple measurements. These effects were eliminated by designing the specimen holder so that the thermocouple was outside the field of the inductive coil. Two tests were conducted to determine if thermocouple coupling had been eliminated. These are described below:

1. The test facility was assembled without a porous specimen in the holder. The traversing thermocouple was located in its position for measurement of gas discharge temperature. The inductive heater was turned on and the work coil actuated to the maximum current (450 amps). Since no coolant was being heated, all increase in thermocouple temperature would be due to RF field effects on the thermocouple itself. No increase in temperature was measured.

2. A second test was conducted to evaluate accuracy of the traversing thermocouple. During several hot flow tests the coolant discharge thermocouple was left in position and the RF field switched off. No sudden change in coolant discharge temperature occurred. If there had been coupling between the RF field and thermocouple, a sudden decrease in indicated coolant temperature would have resulted.

The influence of specimen radiation on traversing thermocouple measurement was also evaluated. The following tests were run:

1. A special holder was designed with a 90 degree bend in the coolant exit duct. A second thermocouple was installed in the holder downstream of the 90 degree bend so that it could not be affected by specimen radiation. A hot flow test was run and the two coolant temperature measurements compared. No difference between the two was apparent.

2. A second test consisted of traversing the thermocouple into position behind a solid specimen that was being heated inductively. Since there was no coolant flow, all temperature rise sensed by the thermocouple would be by radiation. No temperature increase was measured.

Tungsten surface temperature was measured by means of a Leeds and Northrup automatic optical pyrometer, which operates by a continuous automatic matching of the radiation intensity of the target with a standard variable output lamp. Measurement of the voltage to this standard lamp provides a direct indication of the brightness of the target and the resulting brightness temperature. The calibration tables employed for converting the millivolt input to the standard lamp to brightness temperature were supplied by Leeds and Northrup.

In order to convert brightness temperature to true temperature it was necessary to consider the normal spectral emittance of the target material at 0.65 micron. These data were obtained from Reference 12 and employed in the following relation to convert brightness temperature to thermodynamic temperature.

$$\frac{1}{T_S} = \frac{1}{T_B} + \frac{\lambda}{C_2} \ln \varepsilon_\lambda$$

where:

T_S = thermodynamic temperature of the surface

T_B = brightness temperature of the surface

λ = wavelength of the optical pyrometer

C_2 = second radiation constant (2.5896×10^4 °Rμ)

ε_λ = emittance of surface at λ.

The automatic optical pyrometer views the porous tungsten test specimens through a pyrex window. Brightness temperature was corrected for the effect of this window based on Figure 108 from Reference 13.

During operation the test chamber was filled with N_2 or a mixture of N_2 and NH_3. References 14, 15, and 16 indicated that there is no effect of the N_2 or NH_3 vapors on the optical temperature measurement of tungsten.

APPENDIX B

FACILITIES

APPENDIX B

B.1 30 kW Induction Heater

Westinghouse Industrial Radio Frequency Generators are specifically designed for industrial induction heating applications. They conform to NEMA Standards for induction and dielectric equipment, AIEE Proposed Standard and Test Code for Induction and Dielectric Heating, applicable portions of the National Electric Code, and with current JIC Standards as interpreted by I.H.E.A., and to meet the maximum radiation requirements of Part 18 of FCC Rules and Regulations. The generator, designed to operate from a nominal 240 or 480 volt, 3-phase system, has the following characteristics:

RATED OUTPUT		
Power (into NEMA Load)	30 kW	30 kW
Frequency	450 kHz	4.0 MHz
Amperes	168 Amps	350 Amps
Voltage (Max)	4900 Volts	9000 Volts
INPUT (AT RATED OUTPUT)		
kVA	66 kVA	
Frequency	60 Cycles	
Phase	3 Phase	
Volts	220/440	
Power factor	0.95	
OPERATING CONDITIONS		
Ambient temperature	104°F (40°C)	
Cooling water pressure (min)	30 psi diff	
Flow	17 Gpm at 30 psi diff	
Inlet temperature (max)	90°F	
Inlet pressure (max)	90 psi	
Purity - (Spec IES 1000)	IES 1000	
Recommended auxiliary fuses		
For 440 volt operation	10A	
For 220 volt operation	20A	
Recommended control circuit fuse	15A	

B.2 Coolant Supply System

A coolant supply system compatible with both nitrogen and anhydrous ammonia is shown schematically in Figure B-1. Figure B-2 shows the supply system. This system consists of a high-pressure accumulator employing a free piston to pressurize the liquid ammonia, a solenoid shut-off valve, a two-stage filtering system, and adjustable needle valve, and a flow-measuring venturi. During the nitrogen tests, the accumulator can be bypassed and the high-pressure nitrogen supplied directly upstream of the solenoid shut-off valve. Prior to a test, the metering valve downstream of the final filter is preset to produce the desired coolant flow under room-temperature conditions. Expected changes in coolant viscosity and density during the hot tests are accounted for in calculation of desired coolant flow setting at room temperature. The flow-metering valve is located as close as possible to the model holder to minimize coolant flow response time.

B.3 Vacuum Furnace

A vacuum furnace was employed to boil off the copper from the porous tungsten specimens. This furnace (shown in Figure B-3) consists of a water cooled stainless steel tank with a viewing port and a gas tight gland through which a water cooled RF coil is passed. A high capacity diffusion vacuum pump is also attached through a series of valves and a liquid nitrogen cold trap to the stainless steel tank. A 5 kW RF generator is connected to the RF coil and provides the heat to boil off the copper. Boiling off the copper in the presence of a vacuum is necessary both to prevent tungsten oxidation and to achieve copper boiling at relatively low temperatures (copper boils at 2200°F at a pressure of 2.5 x 10^{-3} mm of Hg). This facility was capable of achieving both these conditions.

B.4 Schlieren System

The Schlieren system employed for this study (Figure B-4) was manufactured by Baird Atomic Inc. It consists of a xenon light source that is collected into a parallel beam and passed over the CONAP test specimen. The parallel beam is then focused and used to develop an image on either a viewing screen or camera film. In the portion of the test section where the density is varying due to helium injection the parallel light rays will be bent and consequently not pass through e focal point. A knife edge is inserted at the focal point to eliminate rays that have been deflected from parallel. The elimination of these rays from the image results in a variation of illumination which is proportional to the density gradients across the helium.

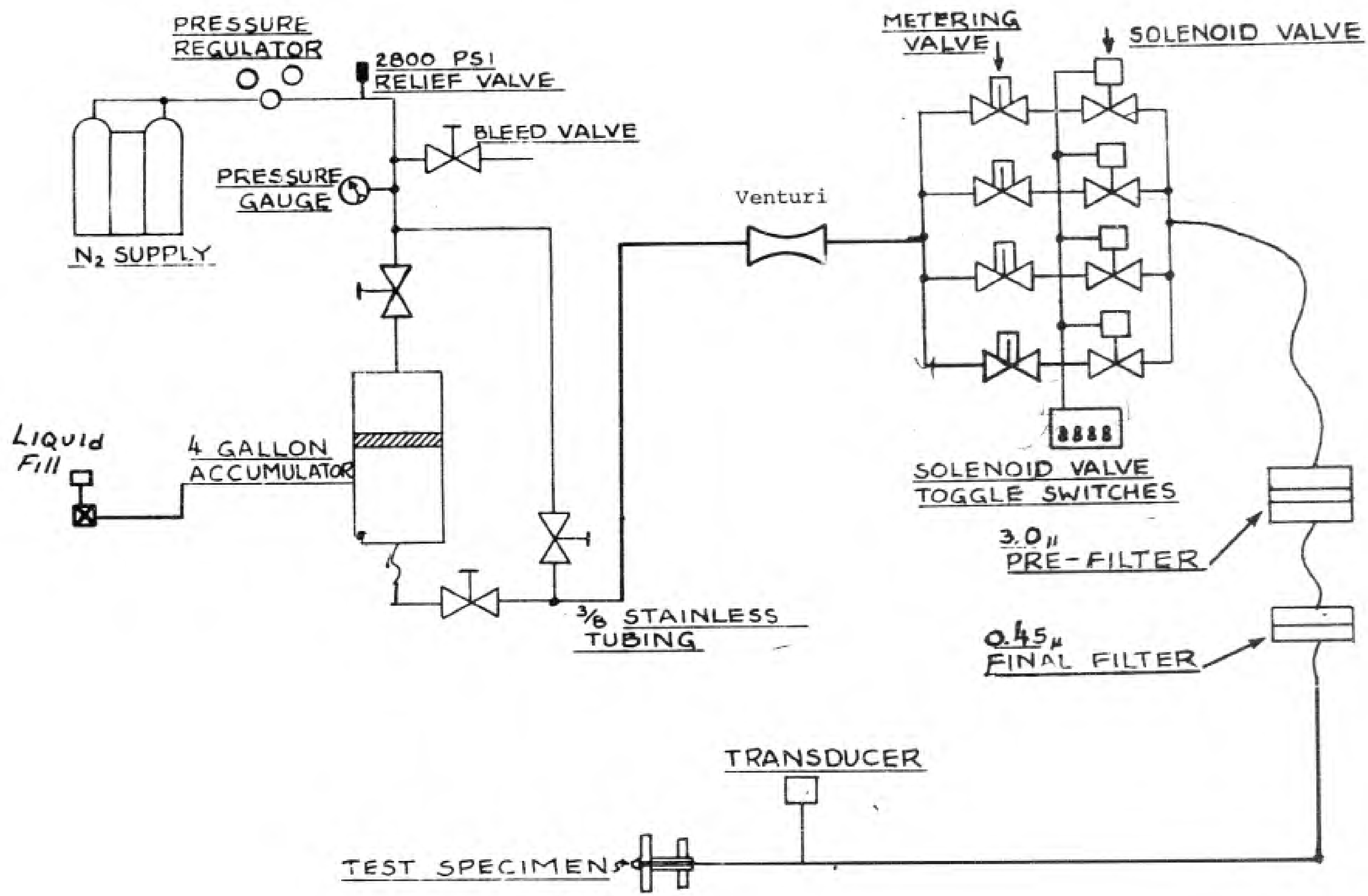

Figure B-1. Flow Direction Test Fixture

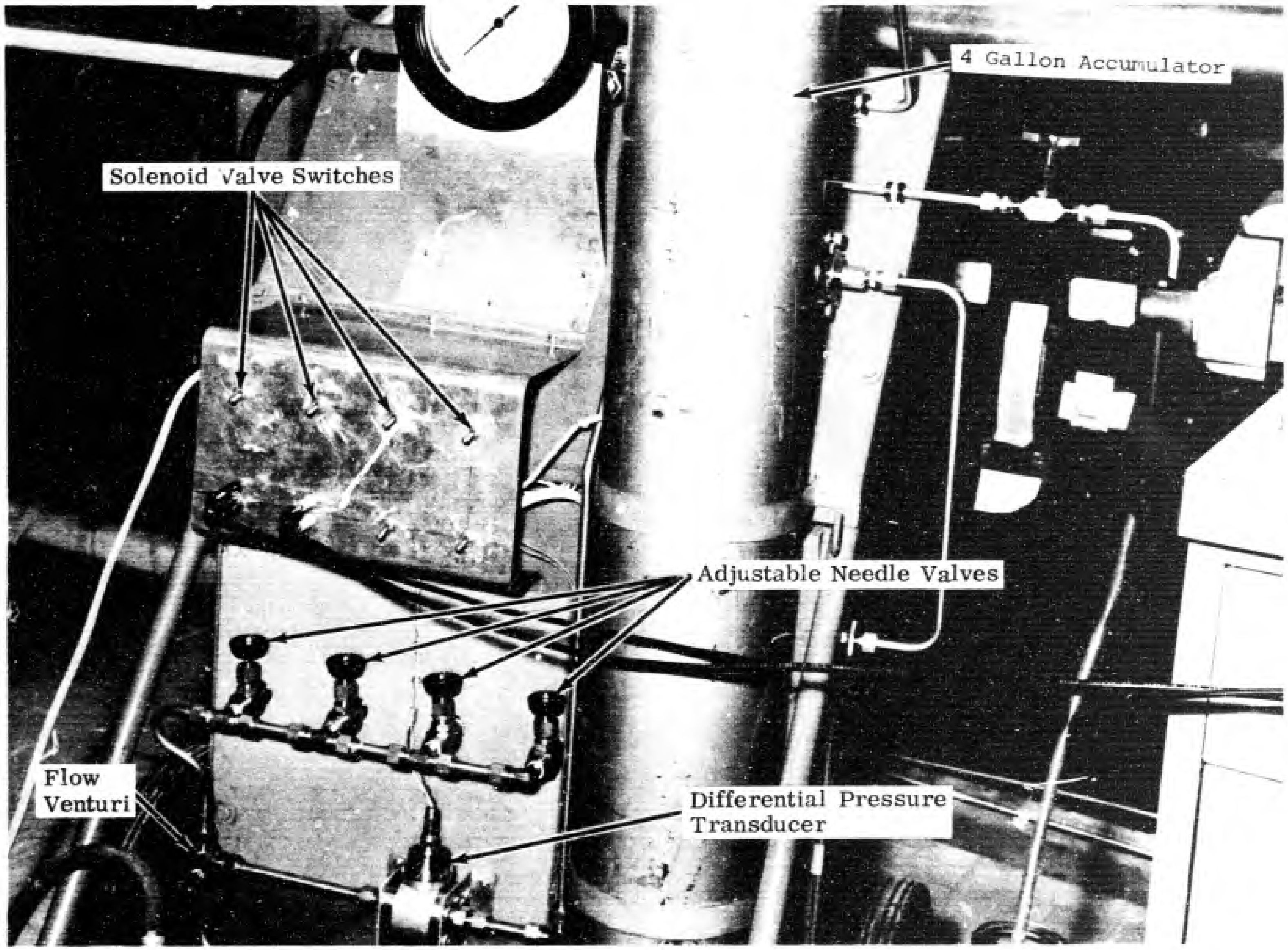

Figure B-2. Coolant Supply System

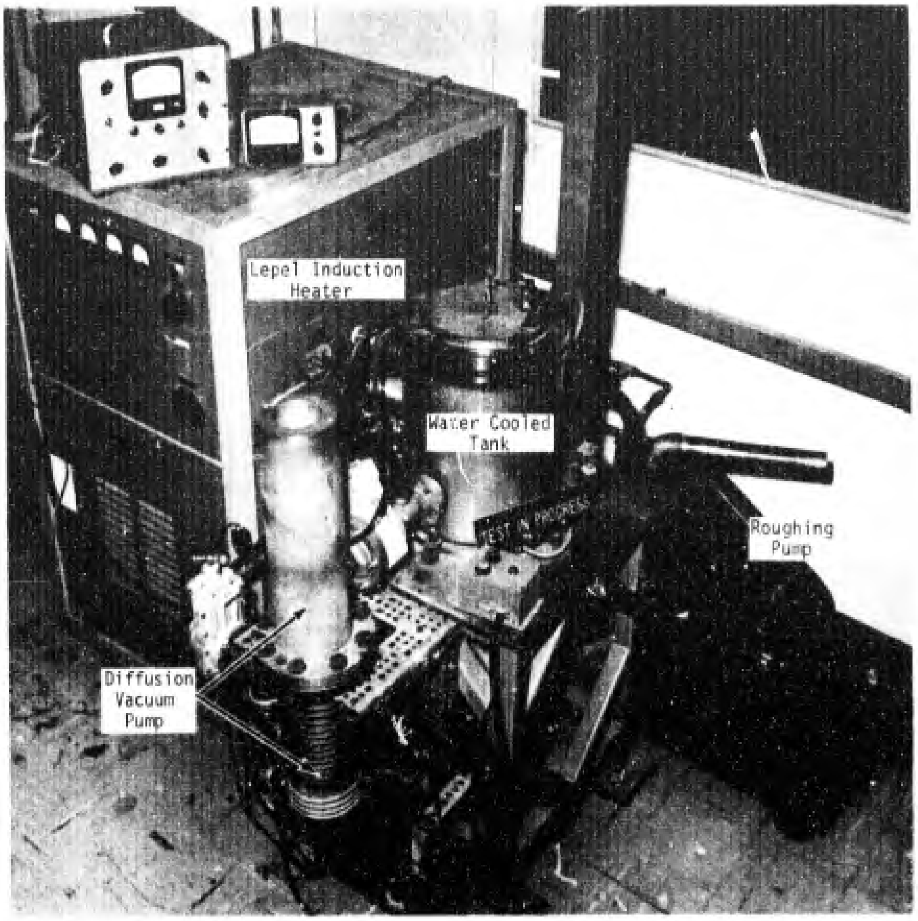

Figure B-3. Vacuum Evaporation Equipment for
Removal of Copper from Tungsten

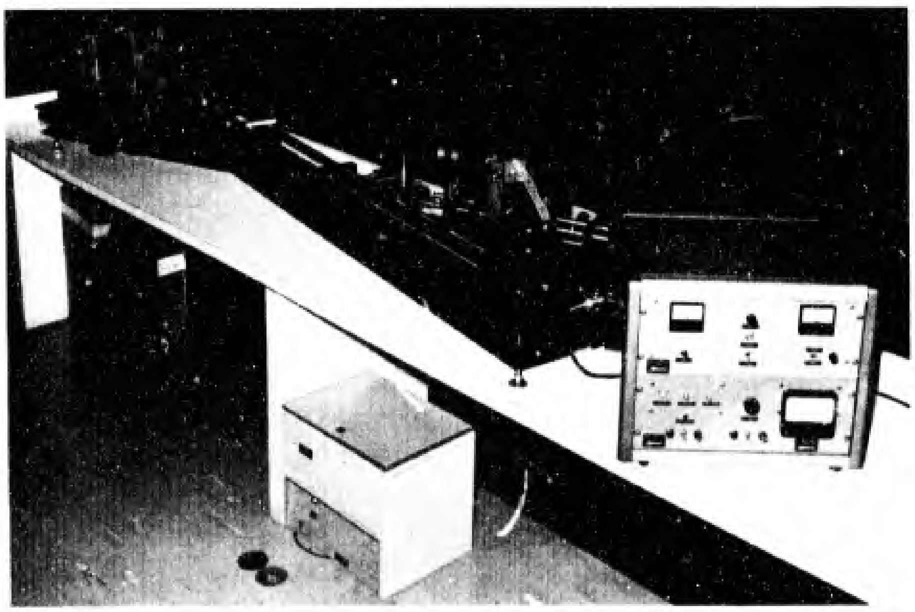

Figure B-4. Schlieren System

APPENDIX C

HEAT TRANSFER BETWEEN A POROUS MEDIUM, WHICH IS UNDER A UNIFORM HEATING MODE, AND A COOLING FLUID

APPENDIX C

Heat transfer between an elemental volume in the porous tungsten may be written as in (1)

$$q = k_m \frac{dT_m}{dx} + Q'x. \tag{1}$$

where

q = heat transfer between elemental volumes
k_m = thermal conductivity of matrix
T_m = matrix temperature
Q' = internal heat generation

Differentiating (1) with respect to x and assuming that the thermoconductivity (k_m) as well as the internal heat generated are constant throughout the porous matrix yields

$$\frac{dq}{dx} = k_m \frac{d^2T_m}{dx^2} + Q'. \tag{2}$$

Heat may also be exchanged between the porous tungsten and the transpiration coolant by convection as shown in Equation (3)

$$q = h'(T_m - T_c)x. \tag{3}$$

where

h' = heat transfer coefficient (volumetric)
T_c = coolant temperature

Differentiating with respect to x and assuming that the internal heat transfer coefficient h' is constant with respect to x and that $h'(T_m-T_c) > h'x \frac{d}{dx}(T_m-T_c)$ yields

$$dq = h'(T_m - T_c). \tag{4}$$

Since the coolant temperature within the porous tungsten is expected to be above the critical temperature for NH3 (271°F) and N_2 (-233°F), the heat of vaporization was neglected and all heat absorbed as shown in (5)

$$q = \dot{m}\, C_{p_c} (T_c - T_i). \tag{5}$$

where

C_{p_c} = coolant specific heat
T_i = initial temperature

Assuming that the coolant specific heat remains constant (5) may be differentiated to yield

$$dq = \dot{m}\, C_{p_c} \frac{dT_c}{dx}. \qquad (6)$$

Setting (4) equal to (6) and differentiating results in

$$h' \frac{dT_m}{dx} - h' \frac{dT_c}{dx} = \dot{m}\, C_{p_c} \frac{d^2 T_c}{dx^2}.$$

Differentiating again results in (7)

$$h' \frac{d^2 T_m}{dx^2} - h' \frac{d^2 T_c}{dx^2} = \dot{m}\, C_{p_c} \frac{d^3 T_c}{dx^3}. \qquad (7)$$

To solve for either the coolant or matrix temperature, one or the other must be eliminated from (7). Since in the steady state all heat introducted into an element must be removed by the coolant, equation (2) may be set equal to (6)

$$km \frac{d^2 T_m}{dx^2} + Q' = \dot{m}\, Cpc \frac{dT_c}{dx}.$$

Substituting into (7) and grouping terms yields

$$\frac{d^3 T_c}{dx^3} + \frac{h'}{\dot{m} C_{p_c}} \left[\frac{d^2 T_c}{dx^2}\right] - \frac{h'}{k_m} \left[\frac{dT_c}{dx}\right] - \frac{h'Q'}{\dot{m} C_{p_c}\, k_m} = 0. \qquad (8)$$

Redefining coefficients in (8) as shown below

$$A = \frac{h'}{\dot{m} C_{p_c}} \qquad B = \frac{-h'}{k_m} \qquad C = \frac{h'Q'}{\dot{m} C_{p_c}\, k_m}.$$

The solution of Equation (8) with the simplified coefficients shown above is

$$Tc = C_1 + C_2 \exp x\left(\frac{-A + \sqrt{A^2 - 4B}}{2}\right) + C_3 \exp x\left(\frac{-A - \sqrt{A^2 - 4B}}{2}\right) + \frac{C}{B} x. \qquad (9)$$

To solve (9), the three constants C_1, C_2, and C_3 must be evaluated. The evaluation of these three boundary conditions are based on the following three assumptions:

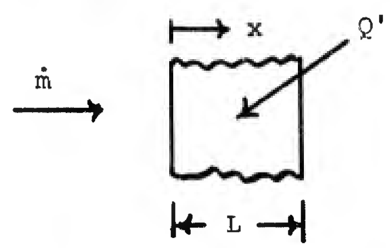

1) At the porous matrix backside the coolant temperature is equal to the coolant supply temperature or at X=0, Tc=Ti.

2) At the porous matrix backside the heat conducted in the coolant is equal to the heat conducted ir the matrix or

$$\text{at } x = 0;\; k_m \frac{dT_m}{dx} = k_c \frac{dT_c}{dx}.$$

3) The third constant may be evaluated based on the assumption that all heat generated by the RF generator in the porous matrix is reflected by the increase in coolant temperature

$$\text{at } x = L;\ T_c = \frac{Q'L}{\dot{m} C_{pc}} + T_i .$$

The above three boundary conditions result in three equations which must be solved simultaneously. The numerical results are then substituted into Equation (9) and the coolant temperature Tc, computed in terms of h', L, $\dot{m}$, Cpc, k_m, k_c, T_i, and Q'.

Next the matrix temperature Tm may be computed as a function of Tc and x. Setting (4) equal to (6) and solving for Tm

$$Tm = \frac{\dot{m}\, C_{p_c}}{h'} \frac{dT_c}{dx} + T_c . \tag{10}$$

Solving for $\frac{dT_c}{dx}$ by differentiating (9) yields

$$\frac{dT_c}{dx} = C_2 \left(\frac{-A+\sqrt{A^2-4B}}{2}\right) \exp x \left(\frac{-A+\sqrt{A^2-4B}}{2}\right)$$

$$+C_3 \left(\frac{-A-\sqrt{A^2-4B}}{2}\right) \exp x \left(\frac{-A-\sqrt{A^2-4B}}{2}\right) + \frac{C}{B} . \tag{11}$$

Matrix temperature Tm may now be numerically determined by substituting (11) into (10) and solving.

The pressure distribution in the coolant is based on the modified Darcy's law

$$\frac{dP}{dx} = -\left[\frac{\dot{m}\mu}{\Gamma\rho} + \beta\rho \left(\frac{\dot{m}}{\rho}\right)^2\right] . \tag{12}$$

Where Γ is the permeability and β is the viscous resistance coefficient. Substituting the gaseous equation of state for $\rho = \frac{P}{ZRT}$ into (12) and integrating yields

$$P_o^2 - P^2 = \frac{2}{\Gamma} \dot{m}\, RLZ \int_o^\eta \mu\, Td\eta + 2\beta\dot{m}^2\, RLZ \int_o^\eta Td\eta \tag{13}$$

where $\eta = \frac{x}{L}$.

The gas viscosity μ is a variable as a function of local coolant temperature. This variation may be approximated by (14)

$$\frac{\mu}{\mu_*} = \left(\frac{Tc}{T_{c*}}\right)^N \tag{14}$$

Where μ^* and Tc^* and the exponential N are constants. These constants are shown below for N_2 and NH_3.

Coolant	Nitrogen	Ammonia
T^* (°R)	560	540
μ^* (lb/ft sec)	1.13×10^{-5}	$.979 \times 10^{-5}$
N	.70	.52

Substituting (14) into (13), the local coolant pressure may be determined. Note that the integrals $\int_o^\eta T \, d\eta$ and $\int_o^\eta T_c^{N+1} \, d\eta$ were solved numerically in this analysis employing finite difference techniques.

APPENDIX D

A FORTRAN IV LISTING FOR THE DETERMINATION OF PARAMETERS IN THE MODIFIED DARCY EQUATION

```
      DOUBLE PRECISION XIN,Y,CO
      REAL M,N,LAM
      DIMENSION P(20),PO(20),M(20),C1(20),C2(20),XIN(20),Y(20),CO(11)
      DIMENSION A1(20),TC1(20)
    1 WRITE(6,6000)
 6000 FORMAT(1H ,47HCOLD FLOW CHARACTERISTICS OF SINTERED MATERIALS/)
      WRITE(6,6001)
 6001 FORMAT(1H ,42HINPUT 0 IF PRESSURE DROP IS TO BE COMPUTED/1H ,56HIN
     1PUT 1 IF DISK PERMEABILITY AND BATA ARE TO BE COMPUTED/)
      READ(5,*)  A
      WRITE(6,6002)
 6002 FORMAT(1H )
      IF(A)100,100,200
  100 WRITE(6,6003)
 6003 FORMAT(1H ,51HINPUT 0 IF COOLANT IS LIQUID OR 1 IF COOLANT IS GAS/
     1)
      READ(5,*)  B
      WRITE(6,6004)
 6004 FORMAT(1H )
      IF(B)101,101,150
  101 WRITE(6,6005)
 6005 FORMAT(1H ,59HINPUT: PERMEABILITY FT2   ,DENSITY LB/FT3 ,
     1 LB/SEC/1H ,45HFLUID VISCOSITY LB/FT-SEC , DISK THICKNESS IN/1H ,4
     26HINERTIAL RESISTANCE COEFF 1/FT ,FLOW AREA IN 2/)
      READ(5,*)  LAM,RHOL,VISCL,X,BATA,A
      A=A/144.
      X=X/12.
  700 WRITE(6,6040)
 6040 FORMAT(1H ,23HINPUT: MASS FLOW LB/SEC/)
      READ(5,*)  W
      W=W/A
      DP=((W*VISCL*X)/(LAM*RHOL*32.174))+(((W**2.)*BATA*X)/(RHOL*32.174)
     1)
      GO TO 500
  150 WRITE(6,6006)
 6006 FORMAT(1H ,58HINPUT: PERMEABILITY FT2 ,          LB/SEC ,COMPRESSI
     1BILITY/1H ,42HGAS CONSTANT FT-LB/LB R ,GAS TEMPERATURE R/1H ,49HDI
     2SK THICKNESS IN ,INERTIAL RESISTANCE COEFF 1/FT/1H ,61HREF TEMP R
     3,REF VISC LB/FT-SEC ,VISC EXPONENT ,FLOW AREA IN 2/)
      READ(5,*)  LAM,Z,R,TC,X,BATA,TR,VISCR,N,A
      A=A/144.
      X=X/12.
  705 WRITE(6,6041)
 6041 FORMAT(1H ,23HINPUT: MASS FLOW LB/SEC/)
      READ(5,*)  W
      W=W/A
      A2=((2.*W*R*X*Z*VISCR)/(LAM*32.174))*((TC**(N+1.))/((TR**N)))
      B1=((2.*BATA*R*X*Z*TC*(W**2.))/32.174)
      DP2=A2+B1
      GO TO 550
  200 WRITE(6,6007)
 6007 FORMAT(1H ,51HINPUT 0 IF COOLANT IS LIQUID OR 1 IF COOLANT IS GAS/
     1)
      READ(5,*)  B
      WRITE(6,6008)
```

```
 6008 FORMAT(1H )
      IF(B)201,201,250
  201 WRITE(6,6009)
 6009 FORMAT(1H ,56HINPUT: LIQUID DENSITY LB/FT3 ,LIQUID VISCOSITY LB/FT
     1-SEC/1H ,21HSPECIMEN THICKNESS IN/)
      READ(5,*)  RHOL,VISCL,X
      X=X/12.
  205 WRITE(6,6010)
 6010 FORMAT(1H ,22HINPUT: NO OF DATA SETS/)
      READ(5,*)  NNU
      WRITE(6,6011)
 6011 FORMAT(1H )
      WRITE(6,6012)
 6012 FORMAT(1H ,55HINPUT: UPSTREAM PRESSURE PSIA ,DOWNSTREAM PRESSURE P
     1SIA/1H ,13HFLOW AREA IN2/1H ,47HCOOLANT FLOW RATE LB/SEC (M IN ASC
     2ENDING ORDER/)
      READ(5,*)  (P(J),J=1,NNU),(PO(J),J=1,NNU),(A1(J),J=1,NNU),(M(J),J=
     11,NNU)
      WRITE(6,6013)
 6013 FORMAT(1H )
      DO 210 J=1,NNU
      A1(J)=A1(J)/144.
      P(J)=P(J)*144.
      PO(J)=PO(J)*144.
      M(J)=M(J)/A1(J)
      C1(J)=((P(J)-PO(J))*(32.179*RHOL))/(VISCL*X*M(J))
      C2(J)=M(J)/VISCL
  210 CONTINUE
      NDATA=NNU
      ND=1.
      DO 215 J=1,NNU
      XIN(J)=C2(J)
      Y(J)=C1(J)
  215 CONTINUE
      CALL POLLSQ (NDATA,XIN,Y,ND,RMS,CO)
      WRITE(6,6014)RMS
 6014 FORMAT(1H ,4HRMS=1X,E10.3/)
      WRITE(6,6015)CO(1),CO(2)
 6015 FORMAT(1H ,6HCO(1)=,1X,E10.3/1H ,6HCO(2)=,1X,E10.3/)
      GO TO 600
  250 WRITE(6,6016)
 6016 FORMAT(1H ,46HINPUT.COMPRESSIBILITY ,GAS CONSTANT FT-LB/LB-R/1H ,3
     16H                  ,DISK THICKNESS IN/1H ,66HREFERENCE TEMP R ,RE
     2F VISC LB/FT-SEC ,VISC EXPONENT ,                  /)
      READ(5,*)  Z,R,X,TR,VISCR,N
      WRITE(6,6019)
 6019 FORMAT(1H )
      X=X/12.
  255 WRITE(6,6017)
 6017 FORMAT(1H ,22HINPUT: NO OF DATA SETS/)
      READ(5,*)  NNU
      WRITE(6,6018)
 6018 FORMAT(1H )
      WRITE(6,6020)
 6020 FORMAT(1H ,55HINPUT: UPSTREAM PRESSURE PSIA ,DOWNSTREAM PRESSURE P
     1SIA/1H ,32HGAS TEMPERATURE R ,FLOW AREA IN2/1H ,47HCOOLANT FLOW RA
     2TE LB/SEC (M IN ASCENDING ORDER)/)
      READ(5,*)  (P(J),J=1,NNU),(PO(J),J=1,NNU),(TC1(J),J=1,NNU),(A1(J),
```

```
     1J=1,NNU),(M(J),J=1,NNU)
      WRITE(6,6021)
 6021 FORMAT(1H )
      DO 260 J=1,NNU
      A1(J)=A1(J)/144.
      P(J)=P(J)*144.
      PO(J)=PO(J)*144.
      M(J)=M(J)/A1(J)
      C1(J)=((32.174*(P(J)**2.-PO(J)**2.)))/((2.*VISCR*M(J)*Z*R*TC1(J)*X
     1*((TC1(J)/TR)**N)))
      C2(J)=M(J)/(VISCR/((TC1(J)/TR)**N))
  260 CONTINUE
      NDATA=NNU
      ND=1.
      DO 265 J=1,NNU
      XIN(J)=C2(J)
      Y(J)=C1(J)
  265 CONTINUE
      CALL POLLSQ (NDATA,XIN,Y,ND,RMS,CO)
      WRITE(6,6022)RMS
 6022 FORMAT(1H ,4HRMS=1X,E10.3/)
      WRITE(6,6023)CO(1),CO(2)
 6023 FORMAT(1H ,6HCO(1)=,1X,E10.3/1H ,6HCO(2)=,1X,E10.3/)
      GO TO 600
  500 WRITE(6,6024)DP
 6024 FORMAT(1H ,21HLIQUID PRESSURE DROP=,1X,E10.3,6HLB/FT2/)
      WRITE(6,6045)
 6045 FORMAT(1H ,64HINPUT 0 IF PROBLEM IS TO BE CONTINUED OR 1 IF PROBLE
     1M IS CHANGED/)
      READ(5,*) D
      WRITE(6,6046)
 6046 FORMAT(1H )
      IF(D)700,700,1000
  550 WRITE(6,6025)DP2
 6025 FORMAT(1H ,26HGAS PRESSURE DROP SQUARED=,1X,E10.3,7HLB2/FT4/)
      WRITE(6,6047)
 6047 FORMAT(1H ,64HINPUT 0 IF PROBLEM IS TO BE CONTINUED OR 1 IF PROBLE
     1M IS CHANGED/)
      READ(5,*) D
      WRITE(6,6048)
 6048 FORMAT(1H )
      IF(D)705,705,1000
  600 LAM=1./CO(1)
      J=NNU
      Y2=CO(1)+(CO(2)*C2(J))
      BATA=(Y2-CO(1))/C2(J)
      DO 605 J=1,NNU
      WRITE(6,6026)C2(J),C1(J)
 6026 FORMAT(1H ,7HM/VISC=,1X,E10.3/1H ,31H(G)(DP)/2(VISC)(M)(Z)(P)(T)(X
     1)=,1X,E10.3/)
  605 CONTINUE
      WRITE(6,6027)LAM,BATA
 6027 FORMAT(1H ,13HPERMEABILITY=,1X,E10.3,3HFT2/1H ,37HINERTIAL RESISTA
     1NCE RESISTANCE COEFF=,1X,E10.3,4H1/FT/)
 1000 GO TO 1
 1001 STOP
      END
```

APPENDIX E

A FORTRAN IV LISTING FOR THE DETERMINATION OF THE INTERNAL HEAT TRANSFER COEFFICIENT

```
      REAL N,MDOT,KM,KF,L,MU,I
      DIMENSION ANU(20),TF(20),TM(20)
    1 WRITE(6,6000)
 6000 FORMAT(1H ,65HONE DIMENSIONAL TRANSPIRATION COOLING MODEL WITH INT
     1ERNAL HEATING/)
      WRITE(6,6003)
 6003 FORMAT(1H ,69HINPUT:K MATRIX BTU/FT SEC R,K FLUID BTU/FT SEC R,CP
     1COOLANT BTU/LB R/)
      READ(5,*)  KM,KF,CP
      WRITE(6,6004)
 6004 FORMAT(1H )
      WRITE(6,6005)
 6005 FORMAT(1H ,60HINPUT:Q INTERNAL HEATING BTU /FT-CU SEC,COOLANT INLE
     1T TEMP R/)
      READ(5,*)  QIN,TFI
      WRITE(6,6006)
 6006 FORMAT(1H )
      WRITE(6,6007)
 6007 FORMAT(1H ,54HINPUT:GAS CONSTANT FT-LB/LB R,COMPRESSIBILITY UNITLE
     1SS/1H ,23HLIQUID DENSITY LB/FT CU/)
      READ(5,*)  R,Z,RHOL
      WRITE(6,6008)
 6008 FORMAT(1H )
      WRITE(6,6009)
 6009 FORMAT(1H ,65HINPUT:FLUID VISCOSITY LB/FT SEC,GAS REFERENCE VISCOS
     1ITY LB/FT SEC/1H ,29HGAS REFERENCE TEMP. R,VIS EXP/)
      READ(5,*)  MU,VISC,TEMP,N
      WRITE(6,6010)
 6010 FORMAT(1H )
   40 WRITE(6,6001)
 6001 FORMAT(1H ,65HINPUT:MDOT LB/FT SQ SEC,INTERNAL HEAT TRANS COEFF BT
     1U/FT CU SEC R/1H ,54H  WALL THICKNESS INCHES,MATRIX PERMEABILITY F
     2T SQ,TW R/1H ,30HINERTIAL RESISTANCE COEFF 1/FT/)
      READ(5,*)  MDOT,HPR,L,GAM,TW,BATA
      WRITE(6,6025)
 6025 FORMAT(1H )
      WRITE(6,6011)
 6011 FORMAT(1H ,45HINPUT:NO OF WALL SEGMENTS,NORMALIZED LOCATION/)
      READ(5,*)  NNU,(ANU(J),J=1,NNU)
      WRITE(6,6012)
 6012 FORMAT(1H )
C
      L=L/12.
      A=HPR/(MDOT*CP)
      B=-(HPR/KM)
   70 C=(HPR*QIN)/(MDOT*CP*KM)
      D=(KM*MDOT*CP)/HPR
      H=(-A+SQRT(A**2.-(4.*B)))/2.
      I=(-A-SQRT(A**2.-(4.*B)))/2.
      E=(D*I)+KM+KF
      F=KM-KF
      G=KF-KM-(H*D)
      ANUM=((C*F)/(B*H*G))-(((C*F)/(B*H*G))*EXP(L*H))+((QIN*L)/(MDOT*CP)
     1)-((C*L)/B)
      ADNOM=(((I*E)/(G*H))*EXP(L*H))+(EXP(L*I))-((I*E)/(G*H))-1.
      C3=ANUM/ADNOM
      C2=((C3*I*E)/(H*G))+((C*F)/(B*H*G))
      C1=TFI-C3-C2
      WRITE(6,6020)L,A,B,C,D,H,I,E,F,G,ANUM,ADNOM,C1,C2,C3
```

```
 6020 FORMAT(1H ,2HL=E10.3/1H ,2HA=E10.3/1H ,2HB=,E10.3/1H ,2HC=,E10.3/1
     1H ,2HD=,E10.3/1H ,2HH=,E10.3/1H ,2HI=,E10.3/1H ,2HE=,E10.3/1H ,2HF
     2=,E10.3/1H ,2HG=,E10.3/1H ,5HANUM=,E10.3/1H ,6HADNOM=,E10.3/1H ,3H
     3C1=,E10.3/1H ,3HC2=,E10.3/1H ,3HC3=,E10.3/)
C
      WRITE(6,6013)
 6013 FORMAT(2X ,65HX IN                TM R              TF R              DPN2
     1         DPN2S/)
C
C     CHECK FOR GAS OR FLUID
C
      IF(RHOL.GT.0.)GO TO 500
      SUM=0.0
      SUM1=0.0
      DO 200 J=1,NNU
      JJ=J
      X=L*ANU(J)
      TF(J)=(C2*EXP(X*H))+(C3*EXP(X*I))+((C*X)/B)+C1
      BB=TF(J)-TFI
      IF(BB)100,100,101
  100 TF(J)=TFI
      BDT=((C2*H*EXP(X*H)))+(C/B)
      TM(J)=(BDT/A)+TF(J)
      CC=TM(J)-TFI
      IF(CC)105,105,102
  105 TM(J)=TFI
      GO TO 102
  101 DTF=((C2*H*EXP(X*H)))+(C3*I*EXP(X*I))+(C/B)
      TM(J)=(DTF/A)+TF(J)
  102 CONS=333580.032
      CONS1=1334320.1
C
      DPN2=((R*MDOT*MU*L*Z)/(CONS*GAM))*SUM
      IF(J.EQ.1)DPN2S=0.
      IF(J.EQ.1)GO TO 20
   30 TINT=(((TF(JJ)**(N+1)+TF(JJ-1)**(N+1)))/2.)*(ANU(JJ)-ANU(JJ-1))
      SUM=SUM+TINT
      TINT1=((TF(JJ)+TF(JJ-1))/2.)*(ANU(JJ)-ANU(JJ-1))
      SUM1=SUM1+TINT1
      DPN2S1=(1./(CONS*GAM))*MDOT*R*L*Z*VISC*(TEMP**(-N))*SUM
      DPN2S2=(2./CONS1)*BATA*(MDOT**2.)*R*L*Z*SUM1
      DPN2S=DPN2S1+DPN2S2
   20 CONTINUE
      X=X*12.
      WRITE(6,6014)X,TM(J),TF(J),DPN2,DPN2S
 6014 FORMAT(5E14.5)
  200 CONTINUE
      GO TO 910
C
C     FLUID
C
  500 CONTINUE
      WRITE(6,6021)
 6021 FORMAT(1H ,27HLIQUID OPTION NOT AVAILABLE/)
      GO TO 1000
  900 DO 600 J = 1,NNU
      X=L*ANU(J)
      DENOM=E*R1*EXP(R1)+F*R2*EXP(R2)
      BRKT=(E*EXP(R1*ANU(J))+F*EXP(R2*ANU(J)))/DENOM
      TM(J)=B*C*BRKT+TF1
```

```
      RKT=(E*R1*EXP(R1*ANU(J))+F*R2*EXP(R2*ANU(J)))/DENOM
      TF(J)=C*RKT+TFI
      DPN=((AMDT*AMU*L)/(4633.056*GAM*RHOL))*ANU(J)
      X=X*12.
      WRITE(6,6015)X,TM,TF(J),DPN
 6015 FORMAT(5E15.6)
  600 CONTINUE
 1000 CONTINUE
      RR=(MDOT*CP)/L
      NN=1
      DD=.5
   50 DT=DD*(TW-TM(NN))
      IF(DT.GT.5.)GO TO 700
      DT=DD*(TM(NN)-TW)
      IF(DT.GT.5.)GO TO 800
   60 WRITE(6,6017)QIN
 6017 FORMAT(1H ,17HINTERNAL HEATING=,1X,E10.3,13HBTU/FT CU SEC/)
      GO TO 40
  700 QIN=RR*((TF(NN)-TFI)+(DT))
      GO TO 70
  800 QIN=RR*((TF(NN)-TFI)-(DT))
      GO TO 70
  910 GO TO 1
   90 STOP
      END
```

REFERENCES

1. ''Evaluation of the CONAP for Advanced ABM Nose Tips,'' Contract No. DAAG46-73-C-0053, AMNRC, Watertown, Mass. October 1972

2. Sanderson, H. C., ''SPRINT Applications Study,'' Martin Marietta Report No. OR 10,350, December 1969, Secret Report

3. Nardacci, J. L., et al, Final Technical Progress Report, ''Re-Entry Systems Environmental Protection (RESEP),'' SAMSO-TR-68-463, March 1969, Secret Report

4. ''Aerotip – An Advanced Transpiration-Cooled, Re-Entry Vehicle Nose Tip,'' Aerojet General, June 1969, Aerojet Proprietary

5. Legendre, P. J., et al, Minutes of the Nose Tip Briefing held August 22, 1969 at Aerospace, TOR-0066 (55816-36)-2

6. Kinnaird. L. D., ''Controlled Atmosphere Protected Surfaces for Advanced Interceptor Missiles,'' presented at the 2nd Aerospace Structures Design Conference, September 28 and 29, 1970

7. Kinnaird, L. D., Cawthon, D. M. and Joyner, C. B., ''Active Oxidation Protection for ABM Control Surfaces,'' AIAA Paper 71-391, April 1971

8. Marco, S. M. and Han. L. S., ''An Investigation of Convection Heat Transfer in a Porous Medium,'' ASME Paper 55-A-104, November 1955

9. Schnieder, P. J., Mauer, R. E. and Strapp, M. G., ''Two Dimensional Transpiration Cooling,'' AIAA Paper 69-96, January 1969

10. Grootenhuis, P., ''The Mechanism and Application of Effusion Cooling,'' Journal of the Royal Aeronautical Society, Vol. 63, February 1959

11. Eckert, E. R. G. and Drake, R. M., ''Heat and Mass Transfer,'' Second Edition, McGraw-Hill Book Company, Inc., New York, N.Y., 1959

12. Touloukian, Y. S., ''Thermophysical Properties of Matter Volume 7, Thermal Radiative Properties Metallic Elements and Alloys,'' Plenum Publishing Co., July 1969

13. Coxon, W. F., ''Temperature Measurement and Control,'' MacMillan Company, 1960

14. Herzberg, G., ''Electronic Spectra and Electronic Structure of Polyatomic Molecules,'' Volume III, D. Van Nostrand Co., July 1966

15. Wolfe, W. L., ''Handbook of Military Infrared Technology,'' U. S. Government Printing Office, 1965

16. Glassman, A., ''Properties of Liquid Rockets,'' Part I, Unpublished Lecture Notes 1964

17. Emerson, W. A., ''Private Communication on 30kw Dual Frequency RF Generator,'' Westinghouse Electric Corporation, Sykesville, Maryland, November 1972

18. Collins, R. E. ''Flow of Fluids Through Porous Materials,'' Reinhold Publishing Company New York, N. Y. June 1961.